이학박사 학위논문

Raman Spectroscopic Probing of the Surface Potential of Metal Nanostructures and its Application to Sensors

금속 나노 구조체 표면 전위의 라만 분광법적 감지와 센서로의 응용

2013 년 8 월

서울대학교 대학원

화학부 물리화학 전공

이 지 원

Raman Spectroscopic Probing of the Surface Potential of Metal Nanostructures and its Application to Sensors

금속 나노 구조체 표면 전위의 라만 분광법적 감지와 센서로의 응용

지도교수: 김 관

이 논문을 이학박사 학위논문으로 제출함

2013 년 6 월

서울대학교 대학원

화학부 물리화학전공

이 지 원

이지원의 이학박사 학위논문을 인준함

2013 년 6 월

위 원 장 _____ ㊞

부위원장 _____ ㊞

위 원 _____ ㊞

위 원 _____ ㊞

위 원 _____ ㊞

Ph. D. Thesis

Raman Spectroscopic Probing of the Surface Potential of Metal Nanostructures and its Application to Sensors

Supervisor: Professor Kwan Kim

Major: Physical Chemistry

By Ji Won Lee

Department of Chemistry

Graduate School of Seoul National University

2012

Abstract

Chapter 1 describes the general introduction of this thesis. Especially, a brief overview of surface-enhanced Raman scattering (SERS) is presented.

In chapter 2, a novel fabrication method of gold and silver nanoparticles films on planar and curved surfaces of glass is described. First, branched poly(ethylenimine) (PEI) was discovered to be an efficient agent for the preparation of stabilized Au nanoparticles at room temperature. The PEI-capped Au nanoparticles prepared in aqueous phase were assembled into 2D arrays, simply by the addition of benzenethiol (BT), not only at the aqueous-toluene interface but also onto the glasses including the inner walls of capillary tubes, the dielectric beads, and even the cotton fabrics. The Au-coated film thus created was highly SERS-active, showing intense peaks of BT. BT could be removed from Au while maintaining the initial SERS activity by treating with a borohydride solution. The BT desorbed Au-coated capillary was used in the study of the relative adsorption of various thiols on Au by SERS. Similary to Au, PEI-capped Ag nanoparticles were produced when a mixture of PEI and $AgNO_3$ solutions was heated. A robust 2D Ag film was formed, by the use of BT and toluene, not only on the planar glass but also on the inner surface of the glass capillary. The silver-coated glass capillary was also highly SERS active, showing intense peaks of BT. BT was removable from the Ag surface by borohydride, maintaining the initial SERS activity. Since PEI was a cationic polyelectrolyte, PEI-capped Ag nanoparticle film was usable in quantification of charged dye molecules, such as sulforhodamine B (SRB), and rhodamine-123 (R123) by the help of SERS and metal-enhanced fluorescence (MEF).

In chapter 3, the SERS of organic isocyanide or cyanide and their application in chemical sensors are presented. First, 2,6-dimethylphenylisocyanide (2,6-DMPI) was adsorbed onto a PEI-capped Au film, and its Raman spectrum was taken in various conditions. When the solution pH was varied, the NC stretching peak of 2,6-DMPI was shifted sharply around pH 8.5, close to the pKa value of the

primary amine of PEI. When a negatively charged poly(acrylic acid) (PAA) was deposited onto the PEI, the ν_{NC} peak shift occured around pH 6.5, close to the average pKa value of PEI and PAA. When additional PEI was deposited onto the PAA, the peak shift of the NC stretching band occured once again around pH 8.5, indicative of the stronger interaction of upper two polyelectrolyte layers. These observation reflected the fact that the surface potential of Au nanoparticles was alternating by the deposition of PEI and PAA. Consulting the potential-dependent SERS data, the surface potential of Au nanoparticles attained a plateau value, that is, -0.41 V versus a saturated Ag/AgCl electrode, after the deposition of five bilayers of PAA and PEI. In ambient condition, the SERS peak of 2,6-DMPI was also affected by volatile organic compounds (VOCs). The NC stretching peak of 2,6-DMPI on Au was either blue- or red-shifted upon the exposure of VOCs. This could be understood by presuming that VOCs were affecting the surface potential of metal nanoparticles. We demonstrated further that the cyanide anion is a far better adsorbate than are isocyanides for the detection of VOCs. This was because the CN stretching frequency varied by nearly twice that of isocyanide in response to an external electric field. Even hazardous metal ions could then be detected since transition metal ions were able to bind to the pendent nitrogen lone pair of electrons of CN on Au, resulting in the shift of the CN stretching band.

Student Number: 2009-30851

Contents

List of Figures

Chapter 1

Chapter 2

corresponding to d. (f) SPR peak position of the Au film measured as a function of the amount of BT added into the toluene phase.

Figure 5. (a) SERS spectrum of BT adsorbed on a PEI-capped Au film (b) SERS spectrum taken after a place-exchange reaction was allowed to occur between BT and 4-ABT for 5 h in a 1 mM ethanol solution of 4-ABT. Vibrational modes exclusively due to BT are labeled with a single asterisk (*); those overlapping with the 4-ABT peaks are marked with a double asterisk (**).

Figure 6. (a) SERS spectra taken during the flow of a 0.1 M ethanolic solution of borohydride through a capillary coated earlier with BT-adsorbed Au nanoparticles: The flow rate of borohydride was 0.19 mL/min. (b) Band area of the BT peak at 1573 cm^{-1} versus the contact time with borohydride in a. (c) SERS spectra of BT on Au measured before (dotted line) and after (solid line) treating with 0.1 M borohydride for 30 min, followed by re-adsorption of BT.

Figure 7. SERS spectra taken by allowing (a) 0.1 mM 4-ABT and (b) 1.0 μM 4-NBT in ethanol to flow through a Au capillary tube: The flow rate was 0.19 mL/min. (c) Time evolution of 4-ABT peak at 1590 cm^{-1} (a_1 band, solid squares) and 1425 cm^{-1} (b_2 band, solid circles) in (a) and (d) that of 4-NBT peak at 1330 cm^{-1} (solid triangles) in (b).

Figure 8. (a) SERS spectra taken by allowing an ethanolic mixture of 0.1 mM 4-ABT and 1.0 μM 4-NBT to flow through a Au capillary tube. The flow rate was 0.19 mL/min. (b) Time evolution of 4-ABT peak at 1590 cm^{-1} (solid squares) and 4-NBT peak at 1330 cm^{-1} (solid triangles) in a.

Figure 9. (a) SERS spectra taken by allowing 10.0 mM 4-NP in ethanol to flow through a Au capillary tube: The flow rate was 0.19 mL/min. (b) NR spectrum of 4-NP in neat solid state.

Figure 10. (a) SERS spectra taken by allowing 1.0 mM adenine in ethanol to flow through a Au capillary tube: The flow rate was 0.19 mL/min. (b) SERS intensity of the ring breathing band of adenine at 734 cm^{-1} versus the concentration of adenine flowed through Au coated capillaries to take SERS spectra. The inset shows a SERS spectrum taken at 2.0×10^{-6} M.

Figure 11. FE-SEM images (scale bars = 1 μm) of cotton fabrics taken before (a) and after coating with Au at low (b), medium (c), and high (d) levels: Specifically, the coatings in (b), (c), and (d) were conducted after adding 0.1, 0.5, and 1.0 mL of BT, respectively, into a mixture of PEI-capped Au sol (5 mL) and toluene (2 mL). The Au weight percentages in b-d were determined to be 0.2%, 1.0%, and 11%, respectively, from the thermogravimetric analysis. (e) EDX data of a cotton fabric after coating with Au in d.

Figure 12. (a) SERS spectrum of BT adsorbed on Au-coated silica beads and (b) that taken after allowing a place-exchange reaction to occur for 5 h in a 1 mM ethanol solution of 4-ABT. Vibrational modes exclusively due to BT are labeled with a single asterisk (*); those overlapping with the 4-ABT peaks are marked with a double asterisk (**). The inset shows the FE-SEM image of Au-coated silica beads (scale bar = 500 nm).

Figure 13. (Upper panel) TEM images and (lower panel) UV-vis spectra of Ag nanoparticles prepared by heating 100 mL of 10 mM aqueous $AgNO_3$ with (a) 3, (b) 1, and (c) 0.5 mL of a 2%(w/w) aqueous PEI solution for 15 min.

Figure 14. (a) UV-vis spectrum of the PEI-stabilized Ag film on a mica substrate formed by adding BT to the toluene phase. For comparison, the UV-vis spectrum of Ag nanoparticles corresponding to Figure 1 is shown in (b). The inset shows the photograph of the Ag films transferred onto a separate glass substrate or onto the inner wall of glass capillary.

Figure 15. SERS spectra of BT adsorbed on PEI-stabilized Ag film on a glass substrate measured (a) as prepared and (b) after treating with 0.1 M borohydride for 30 min, and then (c) after readsorption of BT (treating with 1 mM BT for 1 hr).

Figure 16. SERS spectra of (a) adenine and (b) riboflavin on Ag nanoparticles coated on the inner wall of glass capillaries.

Figure 17. (a) A series of SERS spectra of adenine at various concentrations ranging from 10^{-4} to 10^{-8} M flowed into the Ag-coated capillary. (b) SERS intensity of the ring breathing band of adenine at 734 cm^{-1} normalized with respect to that of a silicon wafer at 520 cm^{-1} versus the concentration of adenine.

Figure 18. (a) A series of SERS spectra of dipicolinic acid at various concentrations ranging from 10^{-3} to 10^{-7} M flowed into the Ag-coated capillary. (b) SERS intensity of dipicolinic acid at 1010 cm^{-1} normalized with respect to that of a silicon wafer at 520 cm^{-1} versus the concentration of dipicolinic acid.

Figure 19. (a) Structure of SRB. (b) UV-vis absorption spectrum of 10^{-5} M aqueous solution of SRB. NR spectra of (c) 10^{-5} M and (d) 0.1 M aqueous solution of SRB measured using 514.5- and 632.8-nm excitation sources, respectively. The inset in (d) shows the magnified spectrum in the 1800 ~ 1200 cm^{-1} region.

Figure 20. SERS spectrum of 10^{-5} M aqueous solution SRB measured using (a) a HNO_3-etched Ag foil and (b) a PEI-capped Ag nanoparticle film as the SERS substrate: a 514.5-nm excitation source was used.

Figure 21. (a) A series of SERS spectra obtained under the flow of 10^{-7} M aqueous solution of SRB at varying pH from 1 to 10 through a PEI-capped Ag capillary tube. The flow rate was 0.19 mL/min. (b) The peak intensity of the xanthenes ring mode at 1650 cm^{-1} plotted against the pH of the solution in (a). (c) Intensity of the background fluorescence at 2500 cm^{-1} in (a) plotted against the pH of the solution. For (b) and (c), the error bars indicate the average and standard deviation of 10 different measurements.

Figure 22. (a) A series of Raman spectra obtained under the flow of 10^{-5} ~ 10^{-10} M aqueous solutions of SRB at pH 4 through a glass capillary coated with PEI-capped Ag nanoparticles. All spectra were obtained using a 514.5-nm radiation as the excitation source. The inset shows the expanded spectrum obtained at 10^{-10} M of SRB. (b) The peak intensity of the xanthenes ring mode at 1650 cm^{-1} in (a) plotted against the SRB concentration. (c) The intensity of the background fluorescence at 2500 cm^{-1} in (a) plotted against the SRB concentration. For (b) and (c), the error bars indicate the average and standard deviation of 10 different measurements.

Figure 23. (a) A series of Raman spectra obtained under the flow of 10^{-5} ~ 10^{-10} M aqueous solutions of SRB at pH 7 through a glass capillary coated with PEI-capped Ag nanoparticles; all spectra obtained using a 514.5-nm radiation as the excitation source. (b) The peak intensity of the xanthenes ring mode at 1650 cm^{-1} and (c) the

intensity of the background fluorescence at 2500 cm^{-1} in (a) plotted against the SRB concentration. For (b) and (c), the error bars indicate the average and standard deviation of 10 different measurements.

Figure 24. (a) Structure of R123. (b) UV-vis absorption spectrum of 10^{-5} M aqueous solution of R123. (c) SERS spectrum of aqueous 10^{-5} M solution of R123 measured during the flow over a HNO_3-etched Ag foil.

Figure 25. The normal Raman spectra of (a) 10^{-5} M and (b) 0.1 M aqueous solution of R123 obtained using 514.5- and 632.8-nm excitation sources, respectively. The inset shows the expanded spectrum measured at 0.1 M of R123.

Figure 26. A series of Raman spectra obtained under the flow of 10^{-5} ~ 10^{-10} M aqueous solutions of R123 at pH 7 through a glass capillary coated with (a) PAA/PEI- and (c) PSS/PEI-capped Ag nanoparticles. All spectra were obtained using a 514.5-nm radiation as the excitation source. (b) The peak intensity of the xanthenes ring mode at 1650 cm^{-1} in (a) and (d) that in (c), drawn against the R123 concentration. For (b) and (d), the error bars indicate the average and standard deviation of 10 different measurements.

Figure 27. (a) The intensity of the background fluorescence at 600 cm^{-1} in Figure 26a drawn against the R123 concentration. (b) A similar plot drawn for the background fluorescence in Figure 26c. For (a) and (b), the error bars indicate the average and standard deviation of 10 different measurements.

Chapter 3

Figure 1. (a) Normal Raman spectrum of neat 2,6-DMPI. (b) SERS spectrum of 2,6-DMPI adsorbed on an ORC roughened Au wire electrode. (c) SERS spectrum of 2,6-DMPI adsorbed on PEI-capped Au nanoparticle film.

Figure 2. (a) A model fragment of PEI consisting of three primary, three secondary, and one tertiary amine groups. Schematics representing one gold atom interacting with (b) primary, (c) secondary, and (d) tertiary amine groups of PEI.

Figure 3. (a) Potential-dependent SERS spectrum of 2,6-DMPI on an ORC roughened Au wire electrode recorded at -0.6, -0.4, -0.2, 0.0 V versus an Ag/AgCl

reference electrode in a 0.1 M $NaClO_4$ aqueous solution. (b) NC stretching frequency versus the electrode potential in (a).

Figure 4. (a) Zeta (ζ)-potential of polystyrene (PS) beads measured after the deposition of PEI-capped Au nanoparticles first (Au) and then after consecutive deposition of PAA (squares) and PEI (circles) thereon. (b) Ellipsometric thickness measured as a function of (PAA/PEI) bilayer deposited on PEI-capped Au-nanoparticles film.

Figure 5. SERS spectra (upper panel) and NC stretching region (lower panel) of 2,6-DMPI on PEI-capped Au nanoparticles measured under the flow of (a) 0.1 M HNO_3 and (b) 0.1 M NaOH.

Figure 6. (a) Acid/base titration curve of PEI (0.4 mg/mL) measured by adding 0.1 N HNO_3 at 1M NaCl solution. (b) NC stretching frequency of 2,6-DMPI on PEI-capped Au nanoparticle film measured as a function of solution pH in contact with the film.

Figure 7. (a) NC stretching region of 2,6-DMPI on PAA/PEI-derivatized Au nanoparticles measured at various pHs (pH 4, 5, 7.5, and 8, respectively, from left to right) and (b) the NC stretching frequency drawn versus the solution pH.

Figure 8. (a) NC stretching region of 2,6-DMPI on PEI/PAA/PEI-derivatized Au nanoparticles measured at various pHs (pH 2, 8, 9, and 10, respectively, from left to right) and (b) the NC stretching frequency drawn versus the solution pH.

Figure 9. (a) NC stretching region measured under the flow of PAA and then PEI through a glass capillary coated previously with a 2,6-DMPI-adsorbed, PEI-capped Au nanoparticle film. (b) NC stretching frequency of 2,6-DMPI drawn as a function of the deposition of PAA (squares) and PEI (circles) layers onto the 2,6-DMPI-adsorbed, PEI-capped Au nanoparticle film.

Figure 10. (a) A series of time-dependent SERS spectra of 2,6-DMPI measured under a flow of CCl_4 at a partial pressure of 12.8 kPa: from bottom to top measured after 0, 2, 6, 10, and 14 min of flow, respectively. (b) Time variation of the NC stretching peak position under flows of CCl_4, methanol, ammonia, and butylamine, at a partial pressure of 12.8 kPa.

Figure 11. (a) Time variation of the NC stretching peak position of 2,6-DMPI measured under a flow of CCl_4 at a partial pressure of 0.64, 1.28, 2.56 or 12.8 kPa. (b) Amount of blue-shift of the NC stretching band (at plateaus) relative to that at 12.8 kPa drawn versus the concentration of CCl_4 passed over 2,6-DMPI-adsorbed PEI-capped Au nanoparticle film: the solid line is a calculated Langmuir adsorption isotherm. See text. (c) A plot of $[CCl_4]/\Delta\tilde{\nu}$ drawn versus $[CCl_4]$ in which $\Delta\tilde{\nu}$ is the NC stretching peak shift measured at the plateau level in (b) and $[CCl_4]$ is the partial pressure of CCl_4 in units of kPa.

Figure 12. (a) A series of time-dependent SERS spectra of 2,6-DMPI measured under a flow of (+)-α-pinene at a partial pressure of 15.6 kPa: from bottom to top measured after 0, 2, 6, 10, and 14 min of flow, respectively. (b) Time variation of the NC stretching peak position under flows of (+)-α-pinene, isoprene, and farnesol, at a partial pressure of 15.6 kPa.

Figure 13. (a) Time variation of the NC stretching peak position of 2,6-DMPI measured under a flow of (+)-α-pinene at a partial pressure of 0.78, 1.56, 7.8, and 15.6 kPa (from top to bottom). (b) Amount of blue-shift of the NC stretching band (at plateaus) relative to that at 15.6 kPa drawn versus the concentration of (+)-α-pinene passed over 2,6-DMPI-adsorbed PEI-capped Au nanoparticle film: the solid line is a calculated Langmuir adsorption isotherm. See text. (c) A plot of [(+)-α-pinene]/$\Delta\tilde{\nu}$ drawn versus [(+)-α-pinene] in which $\Delta\tilde{\nu}$ is the NC stretching peak shift measured at the plateau level in (b) and [(+)-α-pinene] is the partial pressure of (+)-α-pinene in units of kPa.

Figure 14. Normal Raman (NR) spectra of (a) KCN and (b) AgCN in solid state. (c) SERS spectrum of cyanide adsorbed on an ORC-roughened Au substrate.

Figure 15. (a) A series of SERS spectra of cyanide on Au measured as a function of the electrode potential in 0.1 M $NaClO_4$ aqueous solution. (b) Plot of variation of the CN stretching frequency in (a) versus the applied potential.

Figure 16. CN stretching peak of cyanide measured under a flow of (a) CCl_4 or NH_3 at a partial pressure of 12 kPa and (b) farnesol or (+)-α-pinene at a partial pressure of 15 kPa.

List of Schemes

Chapter 1

: General Introduction

1.1. Surface-Enhanced Raman Scattering (SERS)

SERS is a process in which the apparent Raman cross sections of molecules, adsorbed on roughened metal surfaces and particles, are magnificently enhanced by local electromagnetic fields.

1. Discovery of SERS

In 1974, Surface-enhanced Raman scattering (SERS) was discovered by Fleischmann, Hendra, and McQulllan who observed intense Raman scattering from pyridine adsorbed onto a roughened silver electrode surface.[1] Fleischmann's approach was to roughen the electrode to increase its surface area and, hence, the number of adsorbed molecules available for study. They did not find the scattered intensity particularly remarkable, attributing it to the many adsorption sites available on a highly roughened surface and the possibility of multilayer adsorption. Jeanmaire and Van Duyne and Albrecht and Creighton demonstrated independently that the magnitude of the Raman scattering signal can be greatly enhanced when the scatter is placed on or near a roughened silver substrate.[2,3] Jeanmaire and Van Duyne[2] proposed an electric field enhancement mechanism whereas Albrecht and Creighton[3] speculated that resonance Raman scattering from molecular electronic states, broadened by their interaction with the metal surface, might be responsible. This enhanced scattering process is known as surface-enhanced Raman scattering (SERS). In recent years, it has been reported that even single-molecule spectroscopy is possible by SERS, suggesting that the enhancement factor (EF) can reach as much as 10^{14}-10^{15}.[4,5] Since the discovery of SERS, the technique has progressed from model system studies of pyridine on a roughened silver electrode to state-of-the-art surface science and real world sensor applications.

2. Mechanism of SERS

There are two primary theories, one called an electromagnetic enhancement mechanism and the other called a chemical enhancement mechanism.[6,7] The former focus on the enhanced electromagnetic fields which can

be supported on metal surfaces with appropriate morphologies and the latter on changes in the electronic structures of molecules which occur upon adsorption and which can lead to resonance Raman scattering.

2.1. Electromagnetic (EM) enhancement

The surface plasmon is a collective excitation of the electron gas of a conductor; if the excitation is confined to the near surface region it is called surface plasmon. The surface plsmon resonance (SPR) is described this type of oscillation when at resonant conditions. There are two types of SPRs that can be generated, one called surface plasmon polaritons (SPRs)[8-10] which originates from propagating waves along a metal surface and the other called localized surface plasmon resonance (LSPR)[11-14] which is localized to a volume with dimensions smaller than the wavelength of incident light. SPRs are generated when light becomes trapped at a metal dielectric interface. The electromagnetic radiation can be coupled into the free conduction electrons at the surface of a metal.[8] Typically, thin films of Ag, Au, or Cu are used as metal substrates.[8] Light will also interact with metal particles smaller than the wavelength of incident light to generate a LSPR when the dimensions of the particle are too small to support a propagating wave. Small spherical particles have a single, sharp absorption band due to the excitation of what is called a dipole plasmon resonance, where the entire charge distribution of the particle oscillates at the frequency of the incident electric field as illustrated in Figure 1. The electromagnetic field of the light at the surface can be greatly enhanced under conditions of surface plasmon excitation; the amplification of both the incident laser field and the scattered Raman field through their interaction with the surface constitutes the electromagnetic enhancement. Electromagnetic enhancement relies on Raman active molecules being confined within these electromagnetic fields and contributes an average enhancement factor of 10^4.

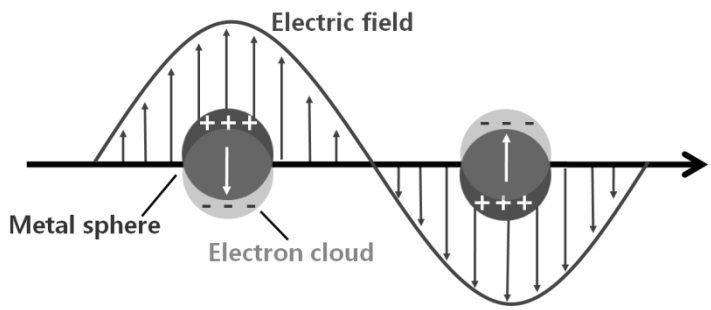

Figure 1. Illustration of excitation of the localized surface plasmon resonance of a spherical nanoparticle by incident electromagnetic radiation.

Extensive theoretical modeling has been performed to provide insight into electromagnetic enhancement by noble metal nanoparticles. The simple example of an isolated sphere, with a quasi-static description of the incident electromagnetic field, has been used to derive the proportionality

$$E^2 \propto E_0^2 \left| \frac{\varepsilon_m - \varepsilon_0}{\varepsilon_m - 2\varepsilon_0} \right|^2$$

in which E is the electric field magnitude at the surface on the sphere, E_0 is the incident field magnitude, ε_m is the wave-dependent dielectric constant of the metal composing the sphere, and ε_0 is the dielectric constant of the local environment around the sphere. This relation revels that when $\varepsilon_m = 2\varepsilon_0$, which can be achieved for Ag and Au at certain wavelength in the visible and near IR, the magnitude of the electric field at the surface of the sphere becomes very large. This field enhancement is induced by satisfying the localized surface plasmon resonance condition. Similar relations can be derived for the extinction and scattering cross sections of the nanoparticle. Maximization of these cross sections at resonant wavelengths yields the spectroscopic signature of exciting the localized surface plasmon resonance.

The electromagnetic enhancement is readily calculated for particles much smaller than the wavelength of light, for the problem reduces to an electrostatic one. The field induced in a small particle by a uniform external electric field is uniform inside the particle, parallel to the applied field and of strength

$$E_{in} = \left[1 + \left\{\left(\frac{\varepsilon_1(\omega)}{\varepsilon_2} - 1\right)A\right\}^{-1}\right]E_{out}$$

Where $\varepsilon_1(\omega)$ is the frequency dependent dielectric function of the metal, ε_2 is the dielectric constant of the surroundings, E_{in} and E_{out} refer to the fields inside and outside the particle, respectively. *A* is a depolarization factor that depends upon the particle geometry. For the particular case of the sphere, A=1/3 so that

$$E_{out} = \frac{\varepsilon_1(\omega) - \varepsilon_2}{\varepsilon_1(\omega) + 2\varepsilon_2}E_{in}$$

which is resonant for frequency where $\varepsilon_1(\omega) = -2\varepsilon_2$. Thus, excitation of this dipolar resonance creates enormous fields at the particle surface that, in effect, increase the laser power at the molecule. In addition to its effect on the incident radiation, the particle amplifies the Raman-scattered radiation. The molecular oscillation drives the sphere resonance that radiates. The extreme sensitivity if SERS to small increases in the local field is easily seen since it scales roughly as $|E_{\text{out}}|^4$.

The last statement is not quite correct, because the Raman radiation occurs at a frequency shifted from the incident radiation. Including this fact, and incorporating the distance dependence of the enhanced field that is given by the dipole decay law, the complete enhancement factor for a sphere in the electrostatic (Rayleigh) limit.

$$G = \left[\frac{\varepsilon_1(\omega_{\text{L}}) - \varepsilon_2}{\varepsilon_1(\omega_{\text{L}}) + 2\varepsilon_2}\right]^2 \left[\frac{\varepsilon_1(\omega_{\text{s}}) - \varepsilon_2}{\varepsilon_1(\omega_{\text{s}}) + 2\varepsilon_2}\right]^2 \left(\frac{r}{r+d}\right)^{12}$$

where L and S refer to the laser and Stokes fields respectively, r is the sphere radius, and d is the molecule-surface separation.

This formula based on a very simple model describes important properties of electromagnetic SERS enhancement and provides qualitative understanding of many of the experimental results. Resonance occurs when $\varepsilon_1 = -2\varepsilon_2$ at either the laser frequency or the scattered frequency. Both excitation and emission can be resonant simultaneously if the vibrational frequency shift is not too large. At resonance, the enhancement scales as the fourth power of the local field of the metallic nanostructure this relation shows why metals of high reflectivity are better enhancers. The distribution of molecular orientations and the variation of the electric field of the dipole over the surface of the sphere result in large depolarization ratios. Electromagnetic SERS enhancement does not require direct contact between molecule and metal but it strongly decreases with growing distance described by the decay of the field of a dipole over the distance $(1/d)^3$ to the fourth power, resulting in $(1/d)^{12}$.

As the particle size increases beyond the Rayleigh limit, the total enhancement decreases. The physical origins of this decrease are radiation damping and dynamic depolarization, the former term referring to loss of energy from the induced moment by emission of radiation, and the latter to the partially destructive interferences between radiations emitted at different location of the larger particles. The effect of incident electromagnetic radiation on the combined colloidal target analyte may simply be described as follow: In the first instance, electromagnetic radiation striking the colloidal surface results in Rayleigh scattering. Rayleigh scattering is a two-photon process which involves the creation of surface plasmon modes. Rayleigh scattering is an elastic process where a photon of identical frequency to that of the incident photon is expelled following the creation of a surface plasmon on the metal surface. In considering the effect of the incident radiation on the target analyte only, an inelastic Raman scattering process is observed. In the case of conventional Raman scattering no metal particles are present and the target analyte interacts directly with the incident electromagnetic

field. In this case the process is inelastic i.e. the frequency of the incident and resultant photon are not identical due to variations within the vibrational energy levels of the target analyte. Incident radiation interact with both the metal to create a surface plasmon and the target analyte where the vibrations in the vibrational levels of the molecule result in photon of unidentical frequency being returned to the metal and scattered (inelastic scattering). The combination of incident radiation and the vibrational energy of the molecule result in significantly increased scattering power observed as SERS.

2.2. Chemical (CHEM) enhancement

Several lines of evidence suggest that the electromagnetic mechanism is not the only one that contributes to the enhancement. Evidence for an additional mechanism beyond electromagnetic includes the first layer effect, quenching of SERS by the presence of submonolayer amounts of foreign atoms and the potential dependence of SERS excitation profiles. This implies that there is also a chemical enhancement mechanism which contributes considerably to the observed SERS signal. In terms of 'chemical enhancement mechanism' (the definition is still under debate, however), it has been assumed that the target molecule must in some way, adsorb onto the SERS substrate surface for the enhancement mechanisms to be applied.

The chemical enhancement is attributed to the specific interactions, i.e. electronic coupling between molecule and metal and the formation of an adsorbate-surface complex. This complex increases, on the one hand, the Raman cross section of the adsorbed molecule compared to that of a free molecule. On the other hand, the chemical mechanism involves charge transfer between the chemisorbed species and the metal surface, which is shown in Figure 2.

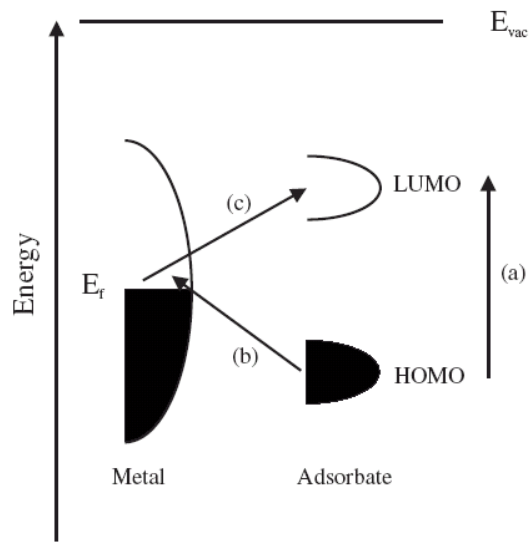

Figure 2. Typical energy level diagram for a molecule adsorbed on a metal surface.

3. Selection Rules

Fundamentally, the selection rules for SERS are the same as those for conventional Raman spectroscopy. To put it shortly, a vibration is Raman-active only if it modifies the polarizability $\boldsymbol{\alpha}$ of the molecule ($\partial\boldsymbol{\alpha}/\partial\mathbf{Q}$) $\neq 0$.[15] $\mathbf{Q}$ is the normal coordinate of the vibration. Selection rules are relaxed resulting in the appearance of normally forbidden Raman modes in the surface spectra. In addition, because the local field at the surface is highest in the direction normal to the surface, vibrational modes involving changes in the adsorbate polarizability perpendicular to the surface are preferentially enhanced.[14] This plus the fact that the electromagnetic field amplitude falls off rapidly with distance from the surface allows one to determine the adsorbate orientation with respect to the average surface normal as well as the proximity of adsorbate functional groups to the surface.

1.2. Fabrication of SERS Substrates

Noble metallic nanostructures have been widely used in SERS because of their LSPR properties.[16] As a result, there have been many studies on preparing noble metallic nanostructures as SERS substrates.[17] As an example, Ag and Au nanostructures of various shapes have been reported,[18] such as nanocubes,[19,20] nanorods,[21,22] nanocaps,[23] nanochains,[24] nanoplates,[25] and honeycomb and hexagonally structured patterns.[26] In order to achieve high SERS signal, fabrication of effective noble metallic nanostructures is crucial. In this section, several common methods, which have been used to generate noble metal nanostructures for SERS applications, will be discussed.

1. Solution-Phase Synthesis

Solution-phase synthesis is a versatile approach to forming NPs that allows control over their size, shape, composition, and structure.[27-33] This approach generally involves the reduction of metal salts in a solution containing an appropriate stabilizer to control the growth and suppress the aggregation of the nanostructures.[34,35]

Polyol process is a simple and versatile method for preparing noble metallic nanostructures with various shapes and sizes.[36,37] In a typical polyol synthesis, the salt precursor and polymeric capping agent are injected into a preheated polyol, especially ethylene glycol, which serves as both a solvent and a reducing agent.[36-39] The nucleation and growth could be controlled through varying the reaction conditions, such as temperature, reagent concentration, and types of additive ions, thus controlling the final products.

Seed-mediated growth technique is preformed using nanocrystals as seeds for further growth.[40-42] The major advantage over conventional methods is that the introduction of preformed seeds into a synthesis process allows nucleation and growth separately, thus making it easier to obtain a desired morphology by only manipulating the growth process.[40] In seed-mediated syntheses, a stable growth solution is prepared containing a metal salt, a mild reducing agent, a surfactant

molecule, and possibly other additives. The seed, the nucleating agent, is added to the solution and the metal salt is reduced directly on the surface of the seed with minimal nucleation occurring in solution.[43-46] The surfactant acts as an organic micellar template for anisotropic growth. The morphology, aspect ratios, and synthetic yields of the seeding approach are controlled by the composition and concentration of the surfactant, additives, seeds, metal salts, and reducing agent.[47,48]

Self-assembly is a typical process, in which metal nanoparticles spontaneously organize into special arrays or patterns with controllable size, and structure. To date, different assembly approaches have been employed to assemble different dimensional metal nanoarchitectures based on corresponding metal nanoparticles.[49,50] These typical assembly approaches include layer-by-layer (LBL) assembly,[51,52] solvent-induced evaporation,[53] Langmuir-Blodget assembly,[54] external field driven assembly,[55] ion or small molecule or polymer induced assembly,[56] and liquid-liquid interface assembly.[57] In addition, metal nanoparticles can be immobilized on solid substrates resulting in 2D structures through chemical attachment, electrostatic interaction, and capillary force.[58-61]

2. Top-Down Lithography

The size, shape, and interparticle spacing of surface-bound metallic nanostructures can be exquisitely controlled using scanning beam lithographies, such as electron beam lithography (EBL) and focused ion beam (FIB) lithography.[62-64] This type of control is highly important for making reproducible substrates with tunable optical properties that are relevant for conducting systematic studies of SERS.[65-67] Recent research has been focused on unconventional lithographic techniques, such as nanosphere lithography (NSL), that are capable of patterning large areas in parallel at low cost.[68]

1.3. Application of SERS

Applied work has focused on using SERS to solve problems in chemical or biological analysis. This is because SERS is a powerful technique allowing for the sensitive and selective detection of low-concentration analytes and there is no interference from water molecules. Total SERS enhancement factors can reach 14 orders of magnitudes, which brings nonresonant surface-enhanced Raman signals to a level comparably, to or even better than fluorescence. Unlike fluorescence, which produces relatively broad bands, Raman scattering yields a unique spectrum composed of several narrow spectral lines, resulting in well-distinguishable spectra even for similar molecules along with the advantage of multiplex capability, and photostability.[69]

1. Trace Chemical Detection

The detection of trace-level explosives and hazardous chemicals is in highly demand with increasing threat from harmful environment.[70] It is challenging to detect trace-level trinitrotoluene (TNT), one of the most widely used explosives due to its low vapor pressure (5 ppb). Kneipp et al. were the first to demonstrate the SERS detection of TNT with a detection limit as low as 100 nM (1 pg) level by using colloidal gold and silver.[71] Tsukruk et al. introduced nanocanal arrays decorated with metal nanoparticles as efficient SERS substrates for trace-level detection of dinitrotoluene (DNT).[72]

In addition, pesticide residues have also been detected through SERS using noble metallic nanostructures. For example, gold nanorods and silver nanocubes were used to detect three different herbicides: the organochlorine compound, the organophosphorus compound trichlorfon, and the triazinic compound ametryn, which were fabricated in solution phase.[73] Moreover, Li et al. detected in situ the parathion residues on fresh oranges using an Au-SiO_2 core-shell nanostructure.[74]

2. Biosensing

SERS has been widely used for bioanalysis, including not only the detection of biomolecules but also the detection of pathogen, and the diagnosis of cancers, which play an important role in the life science for health care or therapeutic treatment.[75-78] There have been reports focused on detecting the sequence of DNA molecule by SERS technique, which was based on the mixed DNA-functionalized silver nanoparticles or gold nanoparticle aggregates.[76] Bacteria, one of the pathogens, have been identified using SERS through internally or externally depositing Ag and Au colloids onto bacteria.[77] The antibody-boned metal colloid can be used to detect special antigens, which serve as biomarkers of cancers.[78] Van Duyne and co-workers were the first to demonstrate in vivo SERS measurements, in which they subcutaneously implanted functionalized AgFON surfaces into the live rats to quantitatively monitor the concentration of glucose levels in the interstitial fluid. Much effort to meet reliable, fast, and high specific detection requirements remains to be proceeded.[81]

3. Real World SERS Application

Although SERS was first observed in 1977, its application to other scientific field and practical problems is quiet recent. For example, SERS nanotags such as Au spheres functionalized with reporter molecules and encapsulated in a silica shell, can be used for the labeling and authentication of different objects.[82] These nanotags are usable for effectice brand protection, for example to encode jewelry or luxury goods. Nanotags can also be embedded in currency or bank notes during the printing process.[83] The development of novel uses for SERS goes hand-in-hand with developments in instrumentation. Portable Raman spectrometers are now available from several manufacturers, making it possible to measure SERS in the field for real-time chemical detection of environmental pollutants.[84]

SERS has begun to be an exciting field with application not only to laboratory research problems but also to real-life situations. Many researchers have only begun to realize the true potential of SERS.[85] Therefore, to use SERS for a

certain analytical purpose, the SERS substrates should be stable, reproducibly prepared, in expensive, and easy to make.

1.4. Reference

1. Fleischman, D. L.; Hendra, P. J.; McQuillan, A. J. *Chem. Phys. Lett*. **1974**, *26*, 123.
2. Jeanmaire, D. L.; Van Duyne, R. P. *J. Electoanal. Chem*. **1977**, *84*, 1.
3. Albrecht, M. G.; Creighton, J. A. *J. Am. Chem. Soc*. **1977**, *99*, 9215.
4. Kneipp, K.; Itzkan, I.; Dasari, R. R.; Field, M. S. *Chem. Rev*. **1999**, *99*, 2957.
5. Nie, S.; Emory, S. R. *Science* **1997**, *275*, 1102.
6. Campion, A.; Kambhampati, P. *Chem. Soc. Rev*. **1998**, *27*, 241.
7. M. Moskovits, *Rev. Mod. Phys.* **1985**, *57*, 783.
8. Raether, H. *Surface Plasmons on Smooth and Rough Surfaces and on Gratings*; Springer: New York, **1988**.
9. Maier, S. A. *Plasmonics: Fundamentals and Applications*; Springer: New York, **2007**.
10. Jones, M. R.; Osberg. K. D.; Macfarlance, R. J.; Langille, M. R.; Mirkin, C. A. *Chem. Rev*. **2011**, *111*, 3736.
11. Maier, S. A. Plasmonics: *Fundamentals and Applications*; Springer: New York, **2007**.
12. Kerker, M. *The Scattering of Light and Other Electromagnetic Radiation*; Academic Press: New York, **1969**.
13. Bohren, C. F.; Huffman, D. R. *Absorption and Scattering of Light by Small Particles*; Wiley Interscience: New York, **1983**.
14. Kreibig, U.; Vollmer, M. *Optical Properties of Metal Clusters*; Springer: Berlin, **1995**.
15. Fadini, A.; Schnepel, F. M. *Vibrational spectroscopy: methods and applications*. English ed.; E. Horwood; Halsted Press: Chichester New York, **1989**.
16. Rycenga, M.; Cobley, C. M.; Zeng, J. *Chem. Rev.* **2011**, *111*, 3669.
17. Tian, Z. Q.; Ren, B.; Wu, D. Y. *J. Phys. Chem. B* **2002**, *106*, 9463.
18. Kumar, G. V. P. *J. Nanophotonics* **20l2**, *6*, 064503.
19. Zhang, Q.; Cobley, C.; Au, L. *ACS Appl. Mater. Inter.* **2009**, *1*, 2044.
20. Zhang, Q.; Li, W.; Moran, C. *J. Am. Chem. Soc.* **2010**, *132*, 11372.

21. Santos Costa, J. C.; Ando, R. A.; Sant′ana, A. C. *Phys. Chem.Chem. Phys.* **2009**, *11*, 7491.

22. Pietrobon, B.; McEachran, M.; Kitaev, V. *ACS Nano* **2009**, *3*, 21.

23. Wang, Y. X.; Liu, S. S.; Gao, W. T.; Li, W.; Zhang, Y. J.; Yang, J. H. *Superlattice Microst.* **2012**, *52*, 750.

24. Jia, H.; Bai, X.; Li, N.; Yu, L.; Zheng, L. *CrystEngComm* **2011**, *13*, 6179.

25. Pastoriza-Santos, I.; Liz-Marz´an, L. M. *J. Mater. Chem.* **2008**, *18*, 1724.

26. Haynes, C. L.; Van Duyne, R. P. *J. Phys. Chem. B* **2001**, *105*, 5599.

27. Wiley, B.; Im, S. H.; Li, Z.-Y.; McLellan, J.; Siekkinen, A.; Xia, Y. *J. Phys. Chem. B* **2006**, *110*, 15666.

28. Hostetler, M. J.; Wingate, J. E.; Zhong, C.-J.; Harris, J. E.; Vachet, R. W.; Clark, M. R.; Londono, J. D.; Green, S. J.; Stokes, J. J.; Wignall, G. D.; Glish, G. L.; Porter, M. D.; Evans, N. D.; Murray, R. W. *Langmuir* **1998**, *14*, 17.

29. Frens, G. *Nat.: Phys. Sci.* **1973**, *241*, 20.

30. Mallin, M. P.; Murphy, C. J. *Nano Lett.* **2002**, *2*, 1235.

31. Steinbruck, A.; Csaki, A.; Festag, G.; Fritzsche, W. *Plasmonics* **2006**, *1*, 79.

32. Lu, X.; Tuan, H.-Y.; Chen, J.; Li, Z.-Y.; Korgel, B. A.; Xia, Y. *J. Am. Chem. Soc.* **2007**, *129*, 1733.

33. Selvakannan, P. R.; Sastry, M. *Chem. Commun.* **2005**, *1684*.

34. Roucoux, A.; Schulz, J.; Patin, H. *Chem. Re*V. **2002**, *102*, 3757.

35. Khomutov, G. B.; Koksharov, Y. A. *Ad*V. *Colloid Interface Sci.* **2006**, *122*, 119.

36. Wiley, B.; Sun, Y.; Mayers, B.; Xia, Y. *Chem. Eur. J.* **2005**, *11*, 454.

37. Wiley, B.; Herricks, T.; Sun, Y.; Xia, Y. *Nano Lett.* **2004**, *4*, 1733.

38. Wiley, B.; Sun, Y.; Chen, J.; Cang, H.; Li, Z.-Y.; Li, X.; Xia, Y. *MRS Bull.* **2005**, *30*, 356.

39. Sun, Y.; Mayers, B.; Xia, Y. *Nano Lett.* **2003**, *3*, 675.

40. Jana, N. R.; Gearheart, L.; Murphy, C. J. *Ad*V. *Mater.* **2001**, *13*, 1389.

41. Iqbal, M.; Chung, Y.-I.; Tae, G. *J. Mater. Chem.* **2007**, *17*, 335.

42. Brown, K. R.; Walter, D. G.; Natan, M. J. *Chem. Mater.* **2000**, *12*, 306.

43. Gole, A.; Murphy, C. J. *Chem. Mater.* **2004**, *16*, 3633.

44. Sau, T. K.; Murphy, C. J. *Langmuir* **2004**, *20*, 6414.

45. Nikoobakht, B.; El-Sayed, M. A. *Chem. Mater.* **2003**, *15*, 1957.

46. Ha, T. H.; Koo, H.-J.; Chung, B. H. *J. Phys. Chem. C* **2007**, *111*, 1123.

47. Murphy, C. J.; Sau, T. K.; Gole, A.; Orendorff, C. J. *MRS Bull.* **2005**, *30*, 349.

48. Xiong, Y.; Cai, H.; Wiley, B. J.; Wang, J.; Kim, M. J.; Xia, Y. *J. Am. Chem. Soc.* **2007**, *129*, 3665.

49. Guo, S.; Dong, S. *J. Mater. Chem.* **2011**, *21*, 16704.

50. Romo-Herrera, J. M.; Alvarez-Puebla, R. A.; Liz-Marzan, L. M. *Nanoscale* 2011, 3, 1304.

51. Zhang, X.; Chen, H.; Zhang, H. *Chem. Commun.* **2007**, 14, 1395.

52. Huang, Y.; Yang, Y.; Chen, Z.; Li, X.; Nogami, M. *J. Mater. Sci.* **2008**, *43*, 5390.

53. Peng, S.; Lee, Y.; Wang, C.; Yin, H.; Dai, S.; Sun, S. *Nano Res.* **2008**, *1*, 229.

54. Tao, A. R.; Huang, J.; Yang, A. P. *Acc. Chem. Res.* **2008**, 41, 1662.

55. H.Wu, F. Bai, Z. Sun et al. *J. Am. Chem. Soc*. **2010**, *132*, 12826.

56. Zhang, B.; Xu, P.; Xie, X. *J. Mater. Chem.* **2011**, *21*, 2495.

57. Duan, H.; Wang, D.; Kurth, D. G.; M¨ohwald, H. *Angew. Chem.* **2004**, *43*, 5639.

58. Yap, F. L.; Thoniyot, P.; Krishnan, S.; Krishnamoorthy, S. *ACS Nano*, **2012**, 6, 2056.

59. Olson, M. A.; Coskun, A.; Klajn, R. *Nano Lett.* **2009**, *9*, 3185.

60. Sardar, R.; Shumaker-Parry, J. S. *Nano Lett.* **2008**, *8*, 731.

61. Chen, G.; Wang, Y.; Tan, L. H. *J. Am. Chem. Soc.* **2009**, *131*, 4218.

62. Su, K.-H.; Wei, Q.-H.; Zhang, X.; Mock, J. J.; Smith, D. R.; Schultz, S. *Nano Lett.* **2003**, *3*, 1087.

63. Grand, J.; Adam, P.-M.; Grimault, A.-S.; Vial, A.; de la Chapelle, M. L.; Bijeon, J.-L.; Kostcheev, S.; Royer, P. *Plasmonics* **2006**, *1*, 135.

64. Ohno, T.; Bain, J. A.; Schlesinger, T. E. *J. Appl. Phys.* **2007**, *101*, 083107/1.

65. Wang, S.; Pile, D. F. P.; Sun, C.; Zhang, X. *Nano Lett.* **2007**, *7*, 1076.

66. Billot, L.; Lamy de la Chapelle, M.; Grimault, A. S.; Vial, A.; Barchiesi, D.; Bijeon, J. L.; Adam, P. M.; Royer, P. *Chem. Phys. Lett.* **2006**, *422*, 303.

67. De Jesus, M. A.; Giesfeldt, K. S.; Oran, J. M.; Abu-Hatab, N. A.; Lavrik, N. V.; Sepaniak, M. J. *Appl. Spectrosc.* **2005**, *59*, 1501.

68. Malinsky, M. D.; Kelly, K. L.; Schatz, G. C.; Van Duyne, R. P. *J. Phys. Chem. B* **2001**, *10*5, 2343.

69. Ni, J.; Lipert, R.J.; Dawson, G. B.; Porter, M. D. *Anal. Chem.* **1999**, *71*, 4903.

70. Moore, D. S. *Rev. Sci. Instrum.* **2004**, *75*, 2499.

71. Kneipp, K.; Wang, Y.; Dasari, R. R.; Feld, M. S.; Gilbert, B. D.; Janni, J.; Steinfeld, J. I. *Spectrochim. Acta A* **1995**, *51*, 2171.

72. Ko, H.; Tsukruk, V. V. *Small* **2008**, *4*, 1980.

73. Santos Costa, J. C.; Ando, R. A.; Sant′ana, A. C. *Phys. Chem. Chem. Phys.* **2009**, *11*, 7491.

74. Li, J. F.; Huang, Y. F.; Ding. Y. *Nature* **2010**, *464*, 392.

75. Pahlow, S.; M¨arz, A.; Seise. B. *Eng.Life Sci.* **2012**, *12*, 131.

76. Thuy, N. T. B.; Yokogawa, R.; Yoshimura, Y.; Fujimoto, K.; Koyano, M.; Maenosono, S. *Analyst*, **2010**, *135*, 595.

77. Efrima, S.; Zeiri, L. *J. Raman Spectrosc.* **2009**, *40*, 277.

78. Kumar, A.; Boruah, B. M.; Liang, X. *J. Nanomater.* **2011**, 2011, 1.

79. Zhai, F.; Huang, Y.; Wang, X.; Lai, K. *Chinese J. Anal. Chem.* **2012**, *40*, 718.

80. Kneipp, J.; Kneipp, H.; McLaughlin, M.; Brown, D.; Kneipp, K. *Nano Lett.* **2006**, *6*, 2225.

81. Stuart, D. A.; Yuen, J. M.; Shah, N.; Lyandres, O.; Yonzon, C. R.; Glucksberg, M. R.; Walsh, J. T.; Van Duyne, R. P. *Anal. Chem.* **2006**, *78*, 7211.

82. Freeman, G. R. U.S. patent 20050019556, **2005**.

83. Natan, M. J. U.S. patent 20070165209, **2007**.

84. Alvarez-Puebla, R. A.; Liz-Marzan, L. M. Energ. Environ. Sci. **2010**, *3*, 1011.

85. Sharma, B.; Frontiera, R. R.; Henry, A.-I.; Ringe, E.; Van Duyne, R. P. *Mater. Today* **2012**, *15*, 16.

Chapter 2

: Novel Fabrication of Metal Nanoparticle Films

1. Novel Fabrication of Au Nanoparticle Films on Planar and Curved Surfaces of Glass and Fiber Materials
2. Novel Fabrication of Ag Nanoparticle Films for SERS and MEF Based Detection of Bio- and Charged Chemicals

2.1. Novel Fabrication of PEI-capped Au Nanoparticle Films on Planar and Curved Surfaces of Glass and Fiber Materials

1. Introduction

Ultrathin films of metal nanoparticles constitute a novel class of materials with a unique combination of nominally zero and two dimensionalities.[1-6] Metal nanoparticles anchored to surfaces in the form of a film are particularly important because of their potential use in nanodevices.[7-11] Over decades, there has, therefore, been much interest not only in the synthesis of monodisperse nanoparticles but also in their self-organization into two-dimensional arrays.[12,13] Au and Ag nanoparticles capped with alkanethiols are known to form extended two-dimensional(2D) arrays by a self-assembly process.[14,15] Fatty-acid-capped Ag and Co nanoparticles are also known to form hexagonally ordered arrays.[16-19] Well-ordered arrays of Au and Pd nanoparticles can be obtained after replacing the polymer coating by alkanethiols through a phase-transfer process.[20,21] Ordered 2D lattices containing Au, Ag, and their alloy nanoparticles of two different sizes are also known.[22-24] In general, however, it is difficult to assemble well-ordered 2D films of metal nanoparticles, without voids, on solid substrates. Large-scale ordered arrays of nanoparticles may be obtained alternatively at the air-water interface using the Langmuir-Blodgett method.[25-27]

In recent years, processes for the creation of 2D arrangements of nanoparticles at the liquid-liquid interfaces have continuously been developed. For instance, Kumar et al. observed that aromatic molecules in the organic phase bind strongly with aqueous gold nanoparticles.[28] This process leads to the immobilization of gold nanoparticles in the form of a highly localized film at the interface. Reincke et al.[29] reported that the introduction of ethanol can pull hydrophilic citrate-stabilized Au nanoparticles into a water-heptane interface, leading to a closely packed monolayer. On the other hand, Han et al. showed that C_{60} can induce the self-assembly of gold nanoparticles at water-oil interfaces.[30]

Most recently, it was demonstrated that poly(ethylenimine) (PEI)-capped Au nanoparticles can be fabricated into a two-dimensional film by adding toluene into the colloidal solution.[31] The Au nanoparticle film layer crept further up the glass wall of the vial after adding benzenethiol (BT) into the toluene phase, indicating that the force driving the formation of an interfacial monolayer is very strong.

In section 2.1, it is demonstrated that robust Au nanoparticle films can be fabricated not only onto the planar and curved surfaces of glasses but also onto the inside surfaces of capillaries by the aforementioned method. First, by deposition onto planar glasses, the optical property of the Au film can be controlled simply by the amount of BT added into the toluene phase. The Au films obtained in that way are highly SERS-active. Second, it is demonstrated that BT molecules present on Au nanoparticles can be easily desorbed by flowing ethanolic borohydride solution through the capillary, maintaining the initial SERS activity. The Au-coated capillary would then be used, for instance, to investigate the relative adsorption strength of diverse organics *in situ* by SERS. Third, it is also demonstrated that Au nanoparticle films can be formed even on silica beads and flexible fabrics. The Au-coated silica beads might then be used as a core material for SERS-based biological sensors, while the Au-coated fabrics would be used as conductive mats for ready dissipation of electrical energy buildup.

2. Experimental

Chemicals. Hydrogen tetrachloroaurate ($HAuCl_4$, 99.99%), branched PEI (MW ~25 kDa), poly(allylamine) hydrochloride (PAH, MW ~70 kDa), BT (99+%), tetraethyl orthosilicate (TEOS, 99%), 4-aminobenzenethiol (4-ABT, 97%), 4-nitrobenzenethiol (4-NBT, 80%), 4-nitrophenol (4-NP, 99+%), adenine (99%) and sodium borohydride ($NaBH_4$, 99%) were purchased from Aldrich, and used as received. Other chemicals, unless specified, were reagent-grade, and highly purified water, with a resistivity greater than 18.0 MΩ cm (Millipore Milli-Q System), was used in preparing aqueous solutions. Silica particles with a mean diameter of 1 μm were prepared using the Stöber-Fink-Bohn method.[32] Bleached and sterilized fabrics made of 100% cotton, purchased from Dong-A Healthcare Company (Seoul, Korea), were used.

Preparation of PEI-capped Au Nanoparticles. To prepare PEI-capped Au nanoparticles, 25 mL of 1.4 mM aqueous $HAuCl_4$ solution was mixed with 0.4−1.0 mL of 1% (w/w) PEI and then stirred vigorously at room temperature for 16 hours. The size of the Au nanoparticles was controlled by the amount of PEI added into the reaction mixture. The reacted mixture was ultracentrifuged and filtered, and then the precipitate was washed with copious amounts of deionized water. The PEI-capped Au nanoparticles thus obtained were redispersed in water.

Preparation of PEI-capped Au Films on Planar and Curved Surfaces of Glass and Fiber Materials. To assemble a 2D film, toluene was first poured over the aqueous Au sol. A fairly homogeneous film was formed at the toluene-water interface by adding BT (0.6 ~ 1.0 mL) into the toluene phase (2 mL). The large area of 2D film was able to form on a separate glass (or a mica) substrate immersed in the mixture. To deposit Au onto the cotton fabrics (or silica beads), the samples were similarly immersed in the mixture. When Au deposited onto the inside walls of a capillary, the mixture was injected using a syringe through the capillary tube. The glass capillary was of dimensions 1.1 mm in inner diameter by 0.2 mm in thickness and 75 mm in length.

Instrumentation. The flow of solutions through a capillary tube was

controlled using a Sage Instruments model 341 syringe pump. UV-vis spectra were obtained with a SINCO S-4100 UV-vis absorption spectrometer. Transmission electron microscope (TEM) images were taken on a JEM-200CX transmission electron microscope at 200 kV. Field emission scanning electron microscope (FE-SEM) images and energy-dispersive X-ray (EDX) analysis were taken with a JSM-6700F. XPS measurements were carried out with a VG Scientific ESCALAB MK II spectrometer using Mg KR X-rays as the light source. FE-SEM operated at 5.0 and 15 kV, respectively. X-ray diffraction (XRD) patterns were obtained on a Rigaku Model D/Max-3C powder diffractometer using Cu K_α radiation. Raman spectra were obtained using a Renishaw Raman system Model 2000 spectrometer. The 632.8 nm line from a 17 mW He/Ne laser (Spectra Physics Model 127) was used as the excitation source. Raman scattering was detected over 180° with a Peltier cooled (−70°C) charge-coupled device (CCD) camera (400 × 600 pixels). The data acquisition time was usually 30 s, and the measured intensity was normalized with respect to that of a silicon wafer at 520 cm^{-1}.

3. Results and Discussion

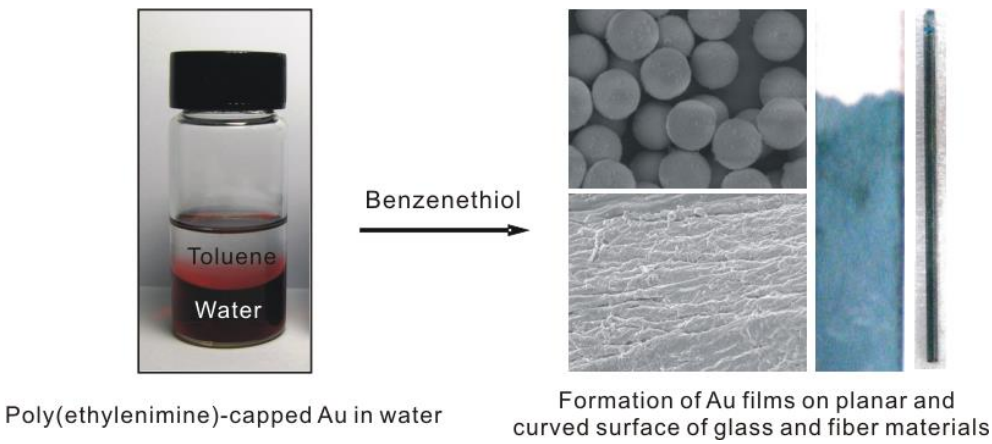

Scheme 1. Schematic representation of the novel fabrication of Au nanoparticle films on planar and curved surfaces of glass and fiber.

Characterization of PEI-capped Au Nanoparticles. Figure 1 shows the evolution of UV-vis spectra of a gold colloid from the mixture of aqueous $HAuCl_4$ and PEI solution at 25°C: in this specific case, the reaction mixture consisted of 25 mL of 1.4 mM $HAuCl_4$ and 0.7 mL of 1% (w/w) PEI. Initially, the aqueous $AuCl_4^-$ solution shows one distinct band at 292 nm caused by the ligand (π)-metal (σ^*) charge-transfer transition.[33] When PEI is added into the aqueous $HAuCl_4$ solutions, the 292 nm band disappears immediately. Much the same behavior was observed when PAH was added into the $HAuCl_4$ solution. This indicates that the π-to-σ^* LMCT is effectively quenched by cationic polyelectrolytes.[34] In the presence of PEI, however, a new band developed at 529 nm for up to 16 hours (see the inset of Figure 1) that could be attributed to the surface plasmon resonance (SPR) band of Au nanoparticles.[35] A similar SPR band is not identified at all in the presence of PAH, suggesting that the reductive capability of PEI is much higher than that of PAH; the weaker reductivity of PAH is supposed to be associated with the

characteristics of primary amines contained.

Having confirmed the formation of Au nanoparticles by PEI, UV-vis spectra were taken using mixtures of $AuCl_4^-$ and PEI in different proportions. As can be seen in Figure 2a, an absorption band appeared at ~520 nm for all mixtures, due to the SPR of Au nanoparticles. A close examination reveals that the peak maximum shifts gradually, from 511 nm to 537 nm, as the amount of PEI is decreased. The SPR peak shift observed must be attributed to the size effect of Au nanoparticles. In general, smaller size metal nanoparticles are obtained when a larger amount of reductant is used.[36] In agreement with this expectation, the size of Au nanoparticles was found to be determined by the amount of PEI used initially with respect to that of $AuCl_4^-$. Figure 2 shows the TEM images of Au nanoparticles corresponding to the UV-vis spectra labeled a, b, and c in the upper panel of Figure 2, respectively; their average sizes are 10 ± 4, 27 ± 7, and 70 ± 19 nm, respectively.

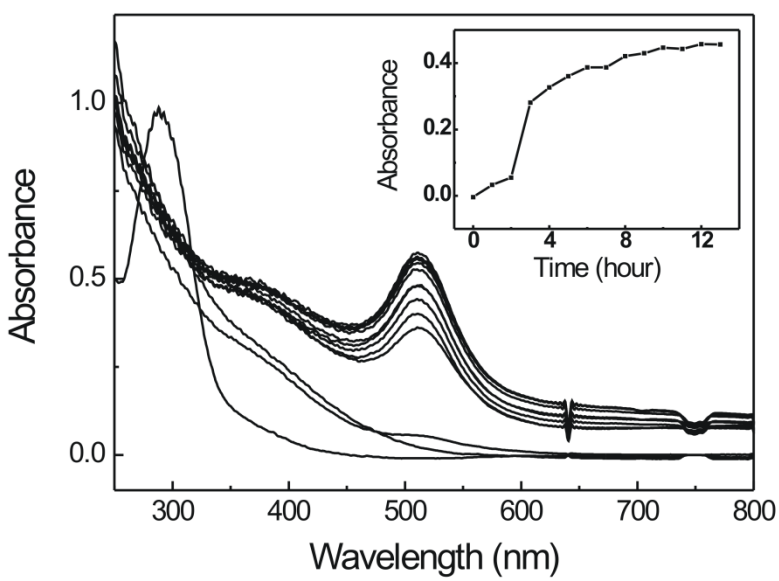

Figure 1. UV-vis spectra obtained as a function of time (time interval = 1 hour) after the addition of PEI to an aqueous $HAuCl_4$ solution at 25°C; the inset shows the absorbance at 517 nm vs the incubation time.

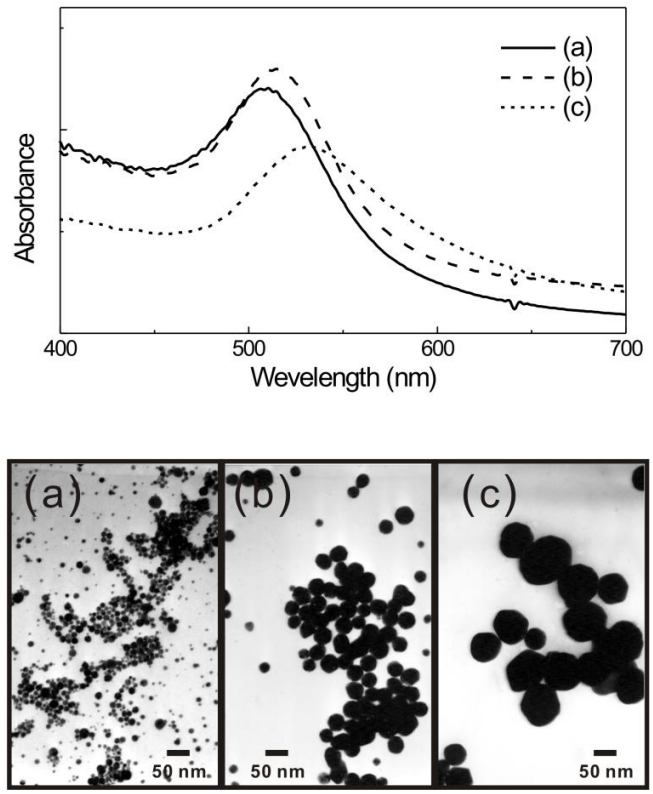

Figure 2. UV-vis spectra and corresponding TEM images taken after mixtures containing 25 mL of 1.4 mM aqueous $HAuCl_4$ solution and (a) 0.9 mL, (b) 0.7 mL, and (c) 0.5 mL of 1%(w/w) aqueous PEI solution were stirred for 16 hours at room temperature.

Clearly, when the concentration of PEI is low, larger particles are formed. This is in sharp contrast to the result of Sun et al.[37] They found that increasing the molar ratio of PEI to gold precursor leads to increasing the particle size. Their opposite result might be due to the use of concentrated $HAuCl_4$ and PEI solutions. Supposedly when the concentration of $HAuCl_4$ is high, Au particles forming by the reductive action of PEI may be positioned to be too close to form larger aggregates before they are stabilized by capping with PEI; relatively larger Au particles will then form as the molar ratio of PEI to gold precursor is increased.

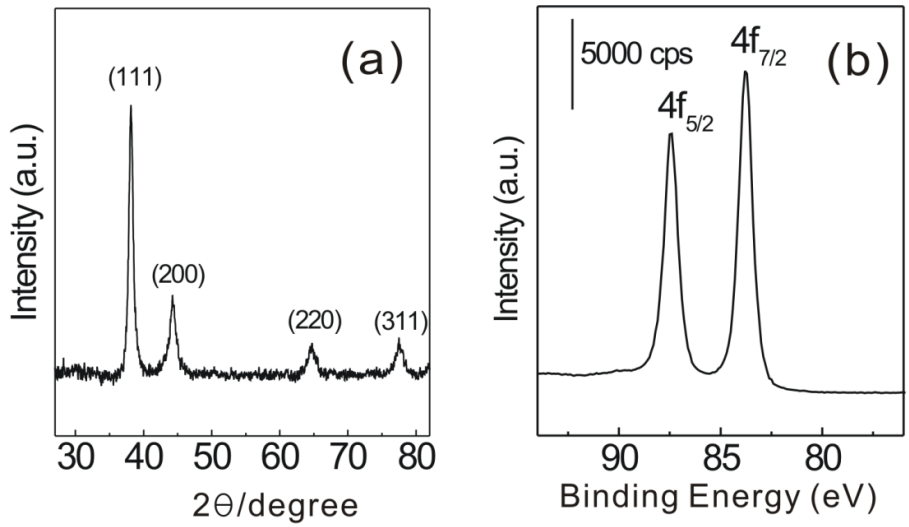

Figure 3. (a) XRD and (b) XPS spectra of PEI-capped Au nanoparticles prepared from a reaction mixture consisting of 25 mL of 1.4 mM $HAuCl_4$ and 0.7 mL of 1%(w/w) PEI.

The formation of Au nanoparticles by the action of PEI can also be confirmed by the XRD pattern (Figure 3a) and the XPS spectra (Figure 3b). The several distinct XRD peaks in Figure 3a can be assigned to the reflections from the 111, 200, 220, and 311 planes of the face centered cubic gold particles.[36] Apart from the XRD data, the XPS peaks at 83.7 and 87.4 eV in Figure 3b can be assigned, respectively, to the $4f_{7/2}$ and $4f_{5/2}$ peaks of zero-valent Au. The binding energy of the Au 4f core level is in agreement with the XPS spectra of alkylamine-capped gold nanoparticles as reported by Leff, Brandt, and Heath.[38] Any $AuCl_4^-$ is expected to give rise to XPS peaks for Au(III) in the form of a doublet at 87 eV ($4f_{7/2}$) and 92 eV ($4f_{5/2}$), but the absence of any peak around 92 eV indicates that no Au (III) species exist in the PEI-capped Au nanoparticles. This does not necessarily mean that all $AuCl_4^-$ ions are reduced completely by PEI. As can be seen in Figure 1, a shoulder band at 380 nm was present even after the 520 nm band attained a

plateau level. The shoulder band completely disappears when the reaction mixture is heated to 50°C, however. The absorbance at 520 nm is then intensified by up to 20%. This indicates that although a fair amount of un-reacted $AuCl_4^-$ is present in the reaction mixture at room temperature, their PEI complexes remain in dissolved states during the centrifugation to obtain PEI-capped Au nanoparticles.

Tetraethylenepentamine (TEP) has the same monomeric unit as PEI. It was examined whether TEP can also be used as a reductant. Although less effective than PEI, TEP was able to reduce $HAuCl_4$ to produce zero valent gold atoms. However, the gold particles that were formed were severely aggregated, since TEP could not function as a stabilizer. To obtain stabilized Au nanoparticles, a polymeric stabilizer such as poly(vinylpyrrolidone) (PVP) has to be added into the reaction medium.[39,40] This clearly supports again the dual roles of PEI, i.e. as both reductant and stabilizer. In fact, the PEI-capped Au nanoparticles prepared in this work remained stable for at least two months without any obvious colloidal aggregation.

Fabrication of PEI-capped Au Films. The assembly of nanoparticles into homogeneous 2D arrays is usually difficult to achieve due to their uncontrolled coagulation. Our group has succeeded in fabricating 2D films after adding a toluene phase into the PEI-capped Au solution. A fairly homogeneous film is formed at the toluene-water interface simply by adding BT into the toluene phase, as shown in Scheme 1. A reddish Au solution turns into a blue-colored film at the toluene-water interface, as well as on the bottle wall, upon adding BT into the toluene phase. Energetically, it must be favorable for thiol-bound Au nanoparticles to move toward the toluene phase, but the particles cannot penetrate into the phase because of the presence of the polyelectrolytes accompanying them. The fact that the filmed layer creeps up the glass walls of the vial indicates that the force driving the formation of an interfacial monolayer is very strong. The film can then be transferred onto a separate glass (or a mica) substrate immersed in the mixture. The Au film formed on a mica substrate by adding BT shows a UV-vis absorption band at ~700 nm. More specifically, its thickness is subtly dependent upon the amount of

BT added into the toluene phase. The absorbance clearly increases upon increasing the amount of BT from 0.6 to 1.0 mL in bands a-d of Figures 4, while the position of the SPR band gradually red shift from 665 to 715 nm as can be seen in Figure 4f.[41] For reference, the UV-vis spectrum of the PEI-capped Au solution is also reproduced in Figure 4(e). Supposedly because of the close-packing of Au nanoparticles, the SPR band has red-shifted by as much as ~200 nm from that in aqueous solution. The latter observation suggests that optically tuned Au films are readily fabricated by varying the amount of BT added into the toluene phase. The inset of Figure 4 shows a typical photograph of the BT-adsorbed, PEI-capped Au film transferred onto a mica substrate.

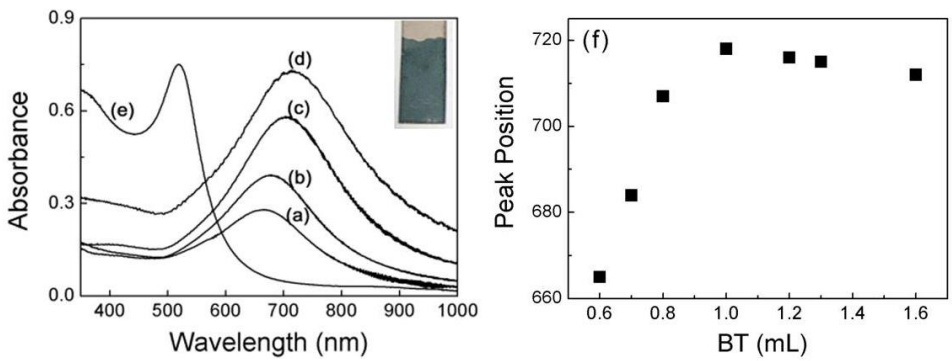

Figure 4. UV-vis spectra of BT-adsorbed, PEI-capped Au films formed at the toluene-water interface by adding increasing amounts of BT to the toluene phase. Specifically, PEI-capped Au nanoparticles were prepared from a reaction mixture consisting of 25 mL of 1.4 mM $HAuCl_4$ and 0.7 mL of 1% (w/w) PEI. After centrifugation, the reaction product was redispersed in 25 mL of water and then 2 mL of toluene was poured over the aqueous solution. Subsequently, (a) 0.6, (b) 0.7, (c) 0.8, and (d) 1.0 mL of BT were added to the toluene phase. For comparison, the UV-vis spectrum of the Au sol before forming a 2D film is reproduced in e. The inset shows the photograph of the PEI-capped Au film on a mica substrate corresponding to d. (f) SPR peak position of the Au film measured as a function of the amount of BT added into the toluene phase.

The PEI-capped Au films are highly SERS-active. Very intense SERS spectra of BT are observed by using the 632.8 nm radiation as the excitation source, as shown in Figure 5a. Both the spot-to-spot and the batch-to-batch variation of the peak intensities were within 6% and 9%, respectively, suggesting that the as-prepared Au film is microscopically smooth. When the BT-adsorbed Au film is soaked in other thiol solutions, such as ethanolic 4-ABT, a place-exchange reaction takes place between BT and 4-ABT. Figure 5b shows a Raman spectrum taken after a place-exchange reaction was allowed to occur for 5 h in a 1 mM ethanol solution of 4-ABT. The distinct peak at 1076 cm^{-1} could be assigned to the ring 7a band of 4-ABT, belonging to the a_1-type vibration. Other distinct peaks at 1138, 1387, and 1430 cm^{-1} could be attributed to the ring 9b, 3, and 19b bands of 4-ABT, respectively, all belonging to the b_2-type vibration. Vibrational modes because of the remaining BT are labeled as asterisks (*) in Figure 5. The appearance of the b_2-type bands of 4-ABT would be due to the participation of the chemical enhancement mechanism.[42]

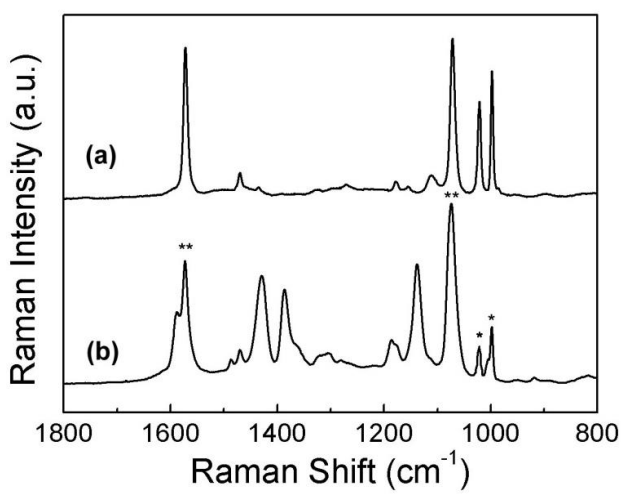

Figure 5. (a) SERS spectrum of BT adsorbed on a PEI-capped Au film (b) SERS spectrum taken after a place-exchange reaction was allowed to occur between BT and 4-ABT for 5 h in a 1 mM ethanol solution of 4-ABT. Vibrational modes exclusively due to BT are labeled with a single asterisk (*); those overlapping with the 4-ABT peaks are marked with a double asterisk (**).

Desorption of BT from PEI-capped Au Films. BT can be desorbed from the PEI-capped Au nanoparticles without disturbing the SERS activity of the Au films. This means that PEI-capped Au films can be used repeatedly to probe the adsorption of various adsorbates without the loss of SERS activity. This is possible due to the potential dependent adsorption strength of thiol molecules onto Au. In fact, when a cathodic scan is applied to a thiol-adsorbed Au electrode, thiol molecules are gradually desorbed from the electrode.[43] In this work, the thiol-adsorbed Au substrates were treated with an ethanolic solution of borohydride. Similarly, Yan et al. reported recently that self-assembled monolayers (SAMs) of thiols on gold could be removed by immersing the SAMs in $NaBH_4$ solution.[44] This method works fairly well, as demonstrated below, using a Au nanoparticle-coated glass capillary.

To deposit Au onto the inside surface of a glass capillary, a mixture comprised of BT, toluene, and PEI-stabilized Au colloid was injected using a syringe through the capillary tube. A gold-coated film was immediately formed upon the injection of the mixture. An intense SERS spectrum of BT was measured by focusing a laser light axially through the capillary wall. A series of SERS spectra was taken by flowing 0.1 M ethanolic borohydride through the capillary tube, as collectively shown in Figure 6a. As expected, the SERS peaks of BT gradually diminished with the borohydride treatment. This is seen more clearly from the band area of the BT peak at 1573 cm^{-1} drawn versus the contact time with borohydride, as shown in Figure 6b. More than 80% of BT is desorbed from the Au within 5 min. It is remarkable that the SERS activity of the PEI-capped Au is maintained even after the treatment with borohydride. When BT is re-adsorbed onto the Au substrate, the SERS spectrum is restored, as shown in Figure 6c.

Competitive Adsorption of 4-ABT and 4-NBT on PEI-capped Au Films. The capillary system could then be used to monitor *in situ* relative adsorption strength of multiple adsorbates. To confirm its practicability, a series of Raman spectra was measured by causing an ethanolic solution of 4-ABT, 4-NBT, or their mixture to flow through a BT-desorbed Au-coated capillary tube. Figure 7a

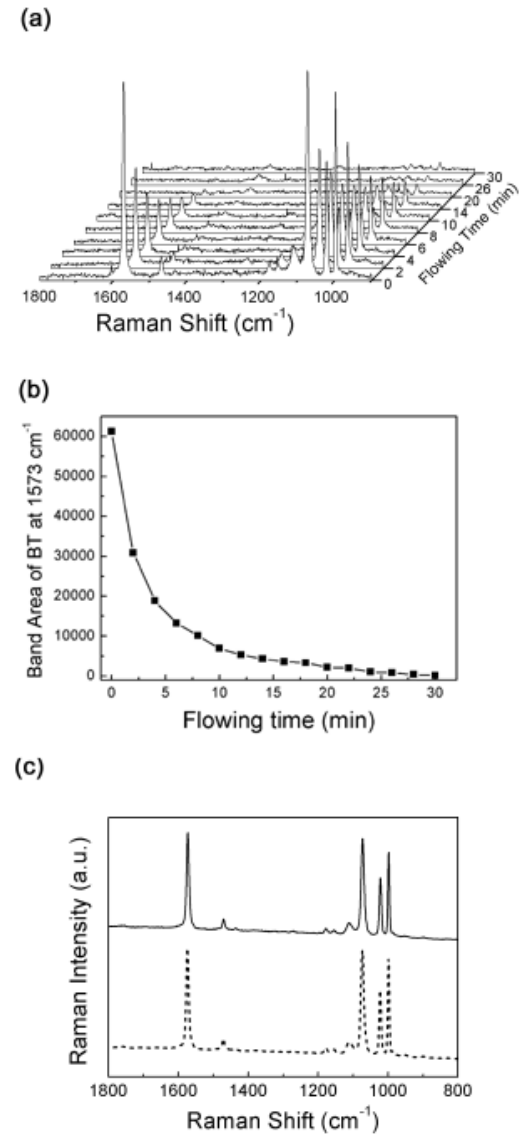

Figure 6. (a) SERS spectra taken during the flow of a 0.1 M ethanolic solution of borohydride through a capillary coated earlier with BT-adsorbed Au nanoparticles: The flow rate of borohydride was 0.19 mL/min. (b) Band area of the BT peak at 1573 cm^{-1} versus the contact time with borohydride in a. (c) SERS spectra of BT on Au measured before (dotted line) and after (solid line) treating with 0.1 M borohydride for 30 min, followed by re-adsorption of BT.

shows a series of SERS spectra taken by flowing a 0.1 mM ethanolic solution of 4-ABT through an Au-coated capillary tube, while Figure 7b shows the case of 1 μM 4-NBT. A hundred times milder solution was used for 4-NBT than for 4-ABT because 4-NBT peaks developed too rapidly in similar concentrations. This suggests that 4-NBT should adsorb onto Au more favorably than 4-ABT. The time evolution of the 4-ABT peaks at 1590 cm^{-1} (a_1 band, solid squares) and at 1425 cm^{-1} (b_2 band, solid circles) is separately drawn as a function of time in Figure 7c. A similar plot for 4-NBT peaks at 1330 cm^{-1} (solid triangles) due to the symmetric stretching vibration of the nitro group of 4-NBT is drawn in Figure 7d.[45] When drawing the latter two figures, the peak intensities were normalized with respect to those of fully covered 4-ABT or 4-NBT on Au. For the case of 4-ABT, the growth pattern of the a_1 band looks different from that of the b_2 band. At the early stage, the a_1 bands are dominant, but shortly after the b_2 bands become as important as the a_1 bands. The different growth rates of a_1 and b_2 bands are not fully understood yet, but this may be due to the fact that the orientation of 4-ABT on Au is dependent upon the surface coverage. For the case of 4-NBT, all of the peaks are observed to grow simultaneously, without showing any difference in growth rate. This may indicate that the orientation of 4-NBT is affected little by surface coverage.

The relative adsorption behavior was examined this time using a mixture of 4-ABT and 4-NBT. Figure 8a shows a series of SERS spectra taken as a function of time while flowing an ethanolic mixture of 0.1 mM 4-ABT and 1 μM 4-NBT through an Au-coated capillary. The time evolution of the 4-ABT peak at 1590 cm^{-1} (solid squares) and 4-NBT peak at 1330 cm^{-1} (solid triangles) is separately drawn in Figure 8b. The ABT peaks grow rapidly initially, reaching a maximum after 10 min and then decrease, approaching a plateau after 40 - 50 min. In contrast, the NBT peaks grow continuously, exhibiting two plateaus, one after ~20 min and the other after 40 - 50 min.

The initial growth rate of 4-NBT is far less than a half of that of 4-ABT. This may not be unexpected from the pattern seen in Figure 7d. It is conjectured that 4-ABT must be kinetically a more favorable adsorbate than 4-NBT, although

4-NBT is thermodynamically a stronger adsorbate to adsorb onto Au. Nearly a half of the 4-ABT adsorbed initially onto Au within 10 min is subject to a ligand exchange reaction with 4-NBT. As this example suggests, the Au-coated capillary could find application in various SERS-based chemical detection systems. After use, the system can be recycled by treating with borohydride.

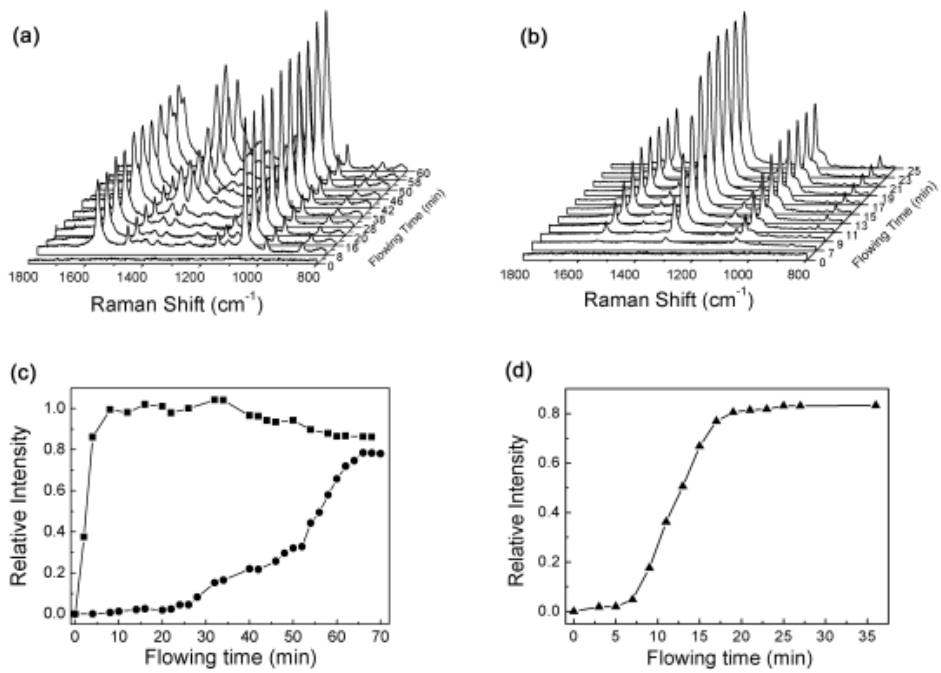

Figure 7. SERS spectra taken by allowing (a) 0.1 mM 4-ABT and (b) 1.0 μM 4-NBT in ethanol to flow through a Au capillary tube: The flow rate was 0.19 mL/min. (c) Time evolution of 4-ABT peak at 1590 cm^{-1} (a_1 band, solid squares) and 1425 cm^{-1} (b_2 band, solid circles) in (a) and (d) that of 4-NBT peak at 1330 cm^{-1} (solid triangles) in (b).

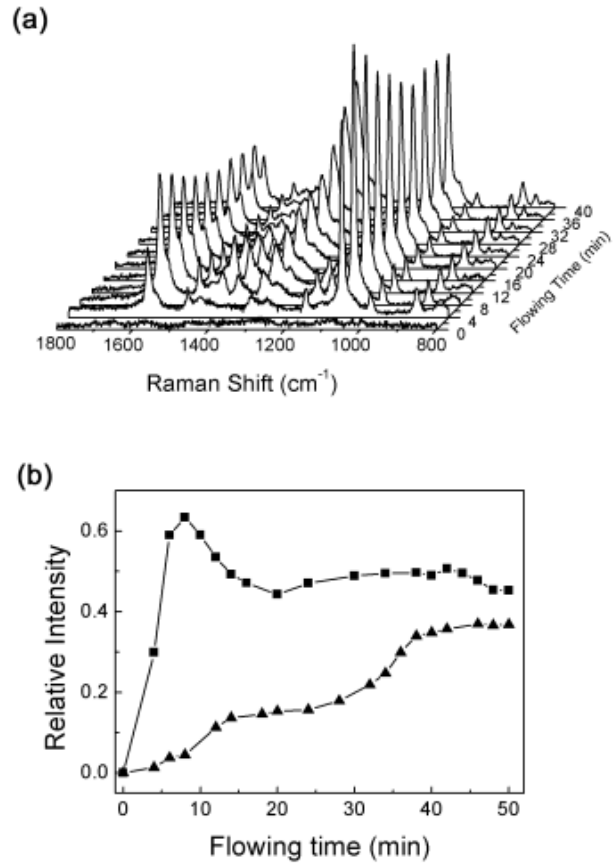

Figure 8. (a) SERS spectra taken by allowing an ethanolic mixture of 0.1 mM 4-ABT and 1.0 μM 4-NBT to flow through a Au capillary tube. The flow rate was 0.19 mL/min. (b) Time evolution of 4-ABT peak at 1590 cm^{-1} (solid squares) and 4-NBT peak at 1330 cm^{-1} (solid triangles) in a.

Chemical Analysis on PEI-capped Au Films. A more challenging task is to ensure that the Au-coated capillary is also worth in the analysis of weakly chemisorbing species by Raman spectroscopy. For that purpose, 4-nitrophenol (4-NP) and adenine were chosen as model compounds. 4-NP possesses characteristic vibrational functional groups, $–NO_2$ allowing easy identification, while adenine is a prototype biomolecule of interest. Figure 9a shows a series of Raman spectra taken

by flowing a 10 mM ethanolic solution of 4-NP through an Au-coated capillary tube. Several peaks were identified at early time and remained nearly constant afterward. The peaks in Figure 9a are quite broad, but they can be attributed to 4-NP. The characteristic NO_2 stretching peak of 4-NP appears at 1323 cm^{-1} in its normal Raman (NR) spectrum in Figure 9b.[46] The band at 1326 cm^{-1} in Figure 9a can be correlated to the 1323 cm^{-1} band in the NR spectrum. Other peaks at 857, 1150, 1258, and 1585 cm^{-1} in Figure 9a can be assigned to ring C-N-C stretch, C-H in-plane bending + O-H deformation, C-O stretch, and C-C stretch of 4-NP, respectively.[46,47] Those peaks also grow simultaneously with the 1326 cm^{-1} peak and can also be correlated to the peaks in Figure 9b. The rather broad feature of the peaks in Figure 9a would reflect that 4-NP molecules were flowing over Au surfaces encountering a heterogeneous environment.

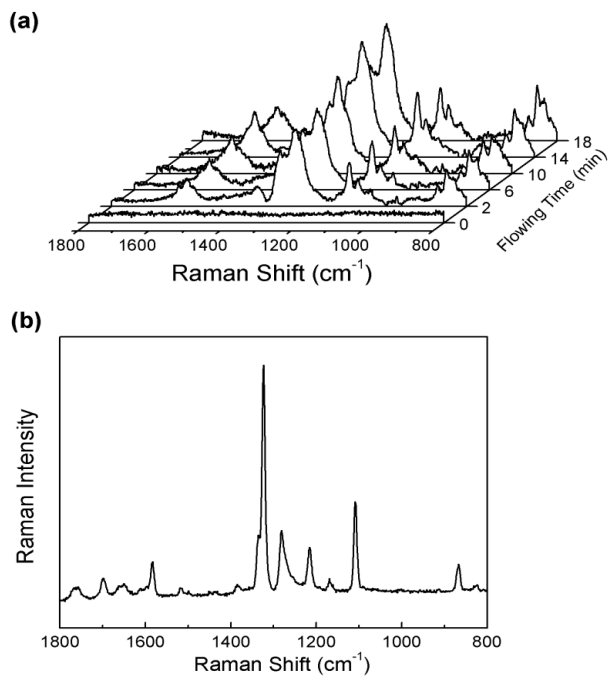

Figure 9. (a) SERS spectra taken by allowing 10.0 mM 4-NP in ethanol to flow through a Au capillary tube: The flow rate was 0.19 mL/min. (b) NR spectrum of 4-NP in neat solid state.

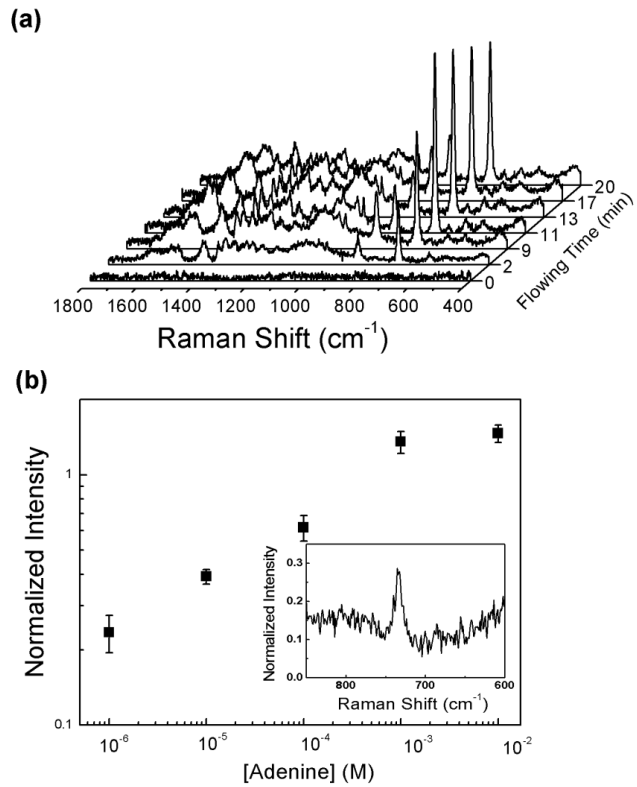

Figure 10. (a) SERS spectra taken by allowing 1.0 mM adenine in ethanol to flow through a Au capillary tube: The flow rate was 0.19 mL/min. (b) SERS intensity of the ring breathing band of adenine at 734 cm^{-1} versus the concentration of adenine flowed through Au coated capillaries to take SERS spectra. The inset shows a SERS spectrum taken at 2.0×10^{-6} M.

Figure 10a shows a series of Raman spectra taken by flowing a 1.0 mM ethanolic solution of adenine through an Au-coated capillary tube. One distinct band is observed at 734 cm^{-1}, along with a series of weak bands in the region 1200 –1500 cm^{-1}; all these bands were assigned previously to the skeletal vibration modes.[48] It is worth examining the detection limit of the present methodology for biological compounds. In this light, SERS spectra were obtained immediately after flowing adenine at various concentrations ranging from 10^{-2} to 10^{-6} M into the Au-

coated capillary. Figure 10b shows the intensity of the adenine peak at 734 cm^{-1} drawn versus the concentration of adenine solution. It is seen that the SERS signal attains a plateau value when the adenine concentration is above 2×10^{-3} M, probably due to the full coverage of adenine molecules onto gold. When the adenine concentration is below 10^{-4} M, the number of adsorbed adenine molecules decreases, resulting in weaker SERS signals. Nonetheless, adenine could be detected as low as 2.0×10^{-6} M with an S/N ratio of 5.5 ± 1.0 (see the inset of Figure 10b); the detection limit would then be 1.0×10^{-6} M based on an S/N ratio of 3. This clearly suggests that our Au-coated capillaries can be used to detect by SERS bio-analytes down to a sub-micromolar regime.

Fabrication of PEI-capped Au Films on a Cotton Fabric and Silica Beads. The dielectric beads and even flexible fabrics can also be coated with Au. As an example, Au was deposited onto a cotton fabric. Dried cotton fabric, consisting of cellulose walls, exhibits a very broad OH stretching band in the 3500 − 3000 cm^{-1} region of the attenuated total reflection infrared (ATR-IR) spectrum.[49] This indicates that the surfaces of cotton fabrics are terminated with OH groups. Thus, like on a slide glass, Au can be deposited onto a cotton fabric by soaking in a mixture of PEI-capped Au colloid and BT-dissolved toluene. As shown in the FE-SEM images in panels b-d of Figures 11, different levels of gold nanoparticles are deposited on a cotton fabric at various concentrations of BT: In this specific example, the coating was conducted after adding 0.1, 0.5, and 1.0 mL of BT, respectively, into a mixture of PEI-capped Au sol (5 mL) and toluene (2 mL). The deposition of Au nanoparticles on a cotton fabric can also be confirmed by EDX analysis shown in Figure 11e. These Au-coated fabrics could be used as conductive mats for the ready dissipation of electrical energy build up. In fact, the sheet resistance of a typical Au film was measured to be about 10^3 kΩ/sq.

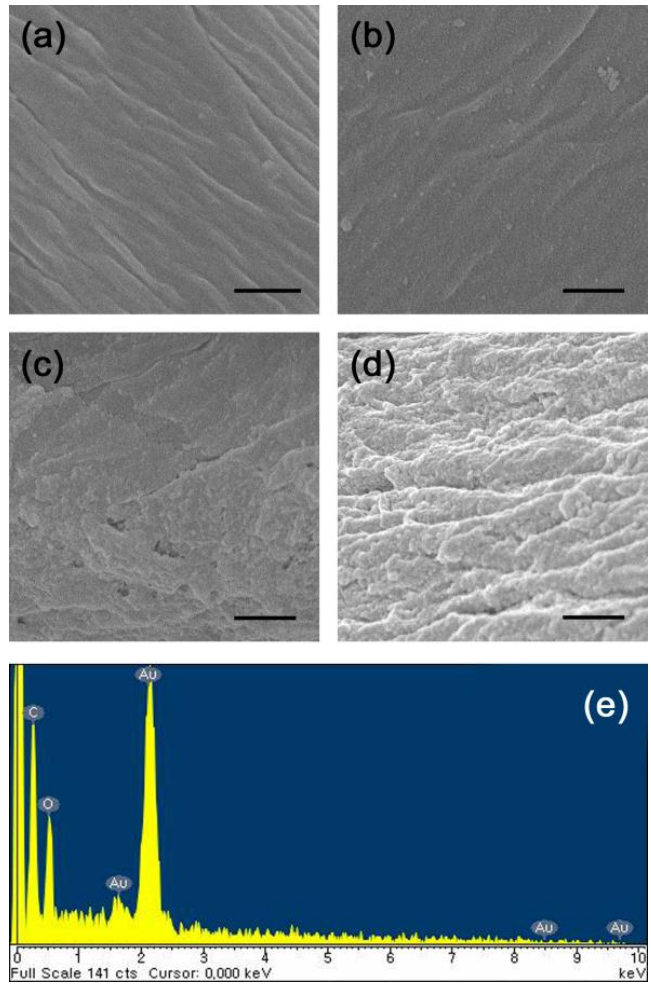

Figure 11. FE-SEM images (scale bars = 1 μm) of cotton fabrics taken before (a) and after coating with Au at low (b), medium (c), and high (d) levels: Specifically, the coatings in (b), (c), and (d) were conducted after adding 0.1, 0.5, and 1.0 mL of BT, respectively, into a mixture of PEI-capped Au sol (5 mL) and toluene (2 mL). The Au weight percentages in b-d were determined to be 0.2%, 1.0%, and 11%, respectively, from the thermogravimetric analysis. (e) EDX data of a cotton fabric after coating with Au in d.

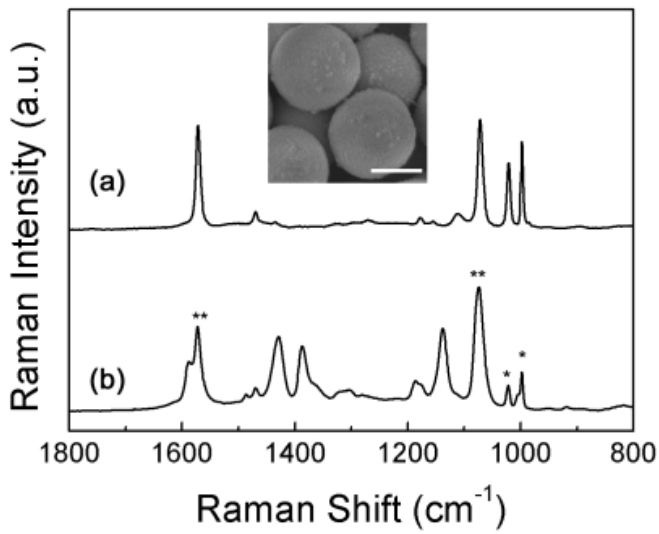

Figure 12. (a) SERS spectrum of BT adsorbed on Au-coated silica beads and (b) that taken after allowing a place-exchange reaction to occur for 5 h in a 1 mM ethanol solution of 4-ABT. Vibrational modes exclusively due to BT are labeled with a single asterisk (*); those overlapping with the 4-ABT peaks are marked with a double asterisk (**). The inset shows the FE-SEM image of Au-coated silica beads (scale bar = 500 nm).

On the other hand, silica beads are terminated with OH groups so that Au can also be deposited simply by pouring a mixture of PEI-capped Au colloid and BT-dissolved toluene over the beads. Figure 12a shows the Raman spectrum of the Au-coated silica beads. The peaks observable can be attributed to BT on Au. When these BT-adsorbed silica beads are soaked in an ethanolic solution of 4-ABT, a ligand exchange reaction takes place, exhibiting the SERS peaks of 4-ABT, as in Figure 12b. The inset of Figure 12 shows the FE-SEM image of Au-coated silica beads. The BT molecules adsorbed on Au can also be removed by soaking in a borohydride solution, once again maintaining the SERS activity. These Au-coated beads will find application as a core material for SERS-based molecular sensors.

4. Summary and Conclusion

One-pot and size-controlled preparation of amine-functionalized gold nanoparticles is possible using PEI simultaneously as a reducing and stabilizing agent. The PEI-capped Au nanoparticles thus prepared in aqueous phase can be assembled into 2D arrays not only at the aqueous/toluene interface but also at the inner surface of the sampling bottle simply by the addition of BT. A Au nanoparticle film can separately be formed, through brief contact with the mixture, on glass slides, the inner walls of capillary tubes, and even on dielectric beads and cotton fabrics. The Au-coated film thus created is confirmed to be highly SERS-active, showing intense peaks of BT. BT can be replaced, on the one hand, with other adsorbates by a place-exchange reaction. More usefully, BT can be removed from Au while maintaining the initial SERS activity by treating with a borohydride solution. The Au-coated capillary was a very efficient SERS active substrate to be usable in the microanalysis of effluent chemicals. The present electroless deposition method of Au is cost-effective and suitable for the mass production of diverse Au films, irrespective of the shapes of the underlying substrates. The method is thus expected to play a significant role in a variety of applications.

2.2. Novel Fabrication of PEI-capped Ag Nanoparticle Films for SERS and MEF Based Detection of Bio- and Charged Chemicals

1. Introduction

Interaction of drug molecules with the cell membrane surface is of an electrostatic character because many drugs are charged molecules and are weak bases or acids having counterions.[50-55] As such, attraction between unlike charges is a well-established phenomenon in biological systems.[50,51] However, it is generally difficult to spectroscopically assess how well drug molecules are bound to membrane surfaces because of the low signal levels transmitted.[56,57] In the case of fluorescent drug molecules, membrane binding may be monitored and quantified by fluorescence spectroscopy, but the usual optical and vibrational spectroscopies cannot be used to analyze the amount of drugs bound to membranes.[58-61] One of interests in our group is in the development of vibrational spectroscopic methods to highlight the interaction of charged drugs with membranes. It is worth exploring the potential of SERS in quantifying the electrostatic adsorption processes by using charged dyes as model drugs.

As described in Chapter 1, SERS is an abnormal surface optical phenomenon that produces strong, increased Raman signals for molecules adsorbed on nanostructured coinage metals.[62-65] The SERS technique offers many advantages, for examples, it is nondestructive, requires little or no sample preparation to obtain structural information, and further allows flexibility in performing measurements in air, vacuum, or solution media.[66-69] One drawback of SERS is that the enhancement properties of a SERS-active surface are highly dependent on its method of preparation and thus on its detailed nanostructure.[70-74] On the other hand, a dramatic increase in the fluorescence emission can occur with nanostructured Ag or Au surface. The phenomenon, called the surface-enhanced fluorescence (SEF) or metal-enhanced fluorescence (MEF), derives from the interaction of the dipole moment of the fluorophore and the surface plasmon field of the metal, resulting in

an increase in the radiative decay rate and stronger fluorescence emission.[75,76] In effect, within an optimal range of distances separating molecules from metal, weakly emitting materials (dyes, proteins, or DNA) with low quantum yields can be transformed into more efficient fluorophores with a shortening of fluorescence lifetimes as well. The reduction in fluorescence lifetimes due to MEF means that molecules spend less time in the excited state, thus reducing photobleaching effects.[77] These characteristics of the MEF effect therefore can be utilized in the development of efficient fluorescence-based sensors and microarrays.[77-79]

As described in the previous section, the PEI-capped Au and Ag nanoparticles prepared in an aqueous phase can be assembled into 2D arrays not only at the aqueous/toluene interface but also at the inner surface of the sampling bottle simply by the addition of BT.[31, 80-83] PEI is a cationic polyelectrolyte; hence, the properties of Au or Ag films are similar to a positively charged membrane. Nonetheless, the actual surface charge density can vary depending upon the pH of the solution in contact with the film. Another merit of the PEI-capped Au or Ag nanoparticle film is that the surface charges can be further modified with anionic and cationic polyelectrolytes by the layer-by-layer (LbL) deposition technique.[84,85] During LbL deposition, a suitable substrate is dipped back and forth between dilute solutions of positively and negatively charged polyelectrolytes which can also be modified to introduce a wide variety of functional groups. The LbL approach can therefore provide a route to tailor the surface characteristics of nanoparticles and can be used to produce SERS substrates with potential applications such as sensors for biological molecules.[86-88]

In section 2.2, it is demonstrated that PEI-capped Ag nanoparticle films can be used for the quantification of an electrostatic adsorption process of charged drug molecules. First, PEI-capped Ag nanoparticle film is confirmed to be highly homogeneous and SERS-active, showing intense peaks of BT. Second, it is demonstrated that PEI-capped Ag nanoparticle films can be used as a platform for the quantification of an electrostatic adsorption process of charged drug molecules, by using charged dye molecules such as sulforhodamine B (SRB) and rhodamine-

123 (R123) as model drugs.

2. Experimental

Chemicals. Silver nitrate ($AgNO_3$, 99.8%), sodium borohydride ($NaBH_4$, 99%), BT (>99%), adenine (99%), (−)-riboflavin (98%), dipicolinic acid (99%), sulforhodamine B (SRB, 75%), rhodamine-123 (R123, 85%), branched PEI (MW ~25 kDa), PSS (MW ~70 kDa), PAA (MW ~450 kDa), and silver foil (0.025-mm thickness, 99.9%) were purchased from Aldrich and used as received. Other chemicals unless specified were of reagent grade, and highly purified water with a resistivity >18.0 MΩ·cm (Millipore Milli-Q System) was used for preparing aqueous solutions.

Preparation of PEI-capped Ag Nanoparticles. The PEI-stabilized Ag nanoparticles were prepared by boiling a mixture of 100 mL of 10 mM $AgNO_3$ and 0.5 ~ 3 mL of 2% (w/w) PEI for 15 min. The reacted mixture was centrifuged, decanted, and the precipitate was washed with copious amounts of deionized water. As determined by transmission electron microscopy (TEM) analysis, the average size of the Ag nanoparticles was 14 ± 6 nm.

Preparation of PEI-capped Ag Films. The PEI-stabilized Ag nanoparticles were re-dispersed in water (5 mL), and toluene (2 mL) was poured over the aqueous Ag sol. A fairly homogeneous film was formed at the toluene-water interface by adding 1 mL of BT into the toluene phase. A large 2D film was also formed on a separate glass substrate immersed in the mixture, showing an intense UV-vis absorption band at ~650 nm. For depositing Ag on the inner walls of a capillary (1.1-mm inner diameter × 0.2-mm thickness × 75-mm length), the mixture was injected using a syringe through the capillary tube. BT was desorbed from the PEI-capped Ag nanoparticles without disturbing the SERS activity of the Ag film, by adding a 0.1 M borohydride solution. After the complete disappearance of the SERS peaks of BT, the PEI-capped Ag film was washed with copious amounts of ethanol and then dried with nitrogen.

Instrumentation. The rate of flow through capillary tubes was controlled using a Sage Instruments Model 341 syringe pump. UV-vis spectra were obtained with a SINCO S-4100 UV-vis absorption spectrometer. TEM images were taken on

a JEM-200CX transmission electron microscope at 200 kV. The zeta potential (ζ) was measured in water by using an electrophoretic light scattering spectrophotometer (ELSZ-1000, OTSUKA Electronics Co. Ltd., Japan): Polystyrene (PS, 0.4-μm-sized) beads were modified consecutively with PEI-capped Ag nanoparticles and PSS or PAA for this measurement. A quartz crystal microbalance (QCM) experiment was conducted using an Au-coated, AT-cut quartz crystal (fundamental resonance frequency, f_o = 10 MHz): the apparent area of the electrode was 0.20 cm^2. Raman spectra were obtained using a Renishaw Raman system Model 2000 spectrometer. The 514-nm line from a 20-mW Ar^+ laser (Melles–Griot Model 351MA520) or the 632.8-nm line from a 17-mW He/Ne laser (Spectra Physics Model 127) was used as the excitation source. Raman scattering was detected over 180° with a Peltier cooled (-70℃) charge-coupled device (CCD) camera (400 × 600 pixels). The data acquisition time was usually 30 s, and the measured intensity was normalized with respect to that of a silicon wafer at 520 cm^{-1}.

3. Results and Discussion

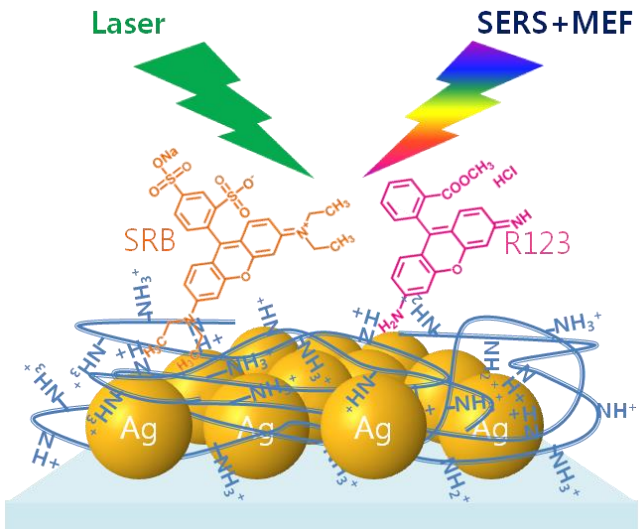

Scheme 2. Schematic representation of the novel fabrication of Ag nanoparticle films for SERS and MEF based detection of charged molecules

Characterization of PEI-capped Ag Nanoparticles. The PEI-stabilized Ag nanoparticles were produced when a mixture of PEI and $AgNO_3$ solutions was heated. The size of the Ag nanoparticles was dependent on the molar ratio of the PEI and $AgNO_3$. By increasing the molar ratio of PEI, smaller metal particles were produced, and vice versa. In this study, approximately 5−30 nm-sized Ag nanoparticles were prepared, as demonstrated in the TEM images in the upper panels of Figure 13. The particles are spherical; the average sizes are 5 ± 4 nm, 14 ± 6 nm, or 30 ± 10 nm. Clearly, when the concentration of PEI is low, larger particles are formed. In the UV-vis absorption spectra shown in the lower panel of Figure 13, the surface plasmon resonance (SPR) bands of Ag nanoparticles are observed at 390-408 nm, depending on the ratio of PEI added into the reaction mixture. Specifically, the maximum of the SPR bands appears at 390, 398, and 408 nm, respectively, for the Ag sols corresponding to the TEM images. The distinct

appearance of the SPR bands indicates that the PEI-stabilized Ag nanoparticles are present in a well-dispersed state. The gradual red-shift reflects the production of larger-sized nanoparticles at lower PEI concentrations.

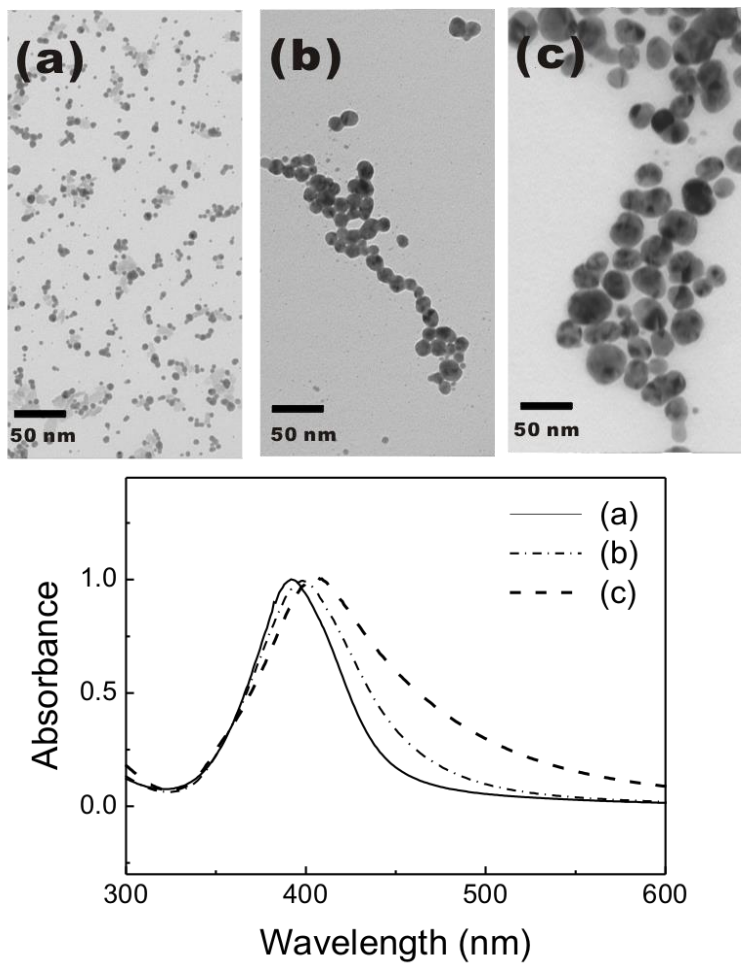

Figure 13. (Upper panel) TEM images and (lower panel) UV-vis spectra of Ag nanoparticles prepared by heating 100 mL of 10 mM aqueous $AgNO_3$ with (a) 3, (b) 1, and (c) 0.5 mL of a 2%(w/w) aqueous PEI solution for 15 min.

Fabrication of PEI-capped Ag Films. A fairly homogeneous Ag film is formed when BT is added into the toluene phase. A yellowish Ag solution turns into a purple-colored film at the toluene-water interface, as well as on the bottle wall. The fact that the filmed layer crept up the glass walls of the vial indicates that the force driving the formation of an interfacial monolayer is very strong. As for Au films, a 2-D Ag film formed at the water-toluene interface can be transferred onto a separate glass substrate immersed in the mixture or onto the inner wall of a glass capillary as shown in the inset of Figure 14. The Ag film formed on a mica substrate by adding BT showed an UV/vis absorption band at ~650 nm as shown in Figure 14a. Its absorbance also increased upon increasing the amount of BT up to 1.0 mL. The red-shift of the SPR band as much as ~250 nm from that in aqueous solution and the increase in its absorbance are indicative of the close-packing of Ag nanoparticles in the film state.[89] Much the same Ag film can be fabricated immediately onto the inside surface of a glass capillary by injecting a mixture comprised of BT, toluene, and PEI-stabilized Ag colloid through the capillary tube.

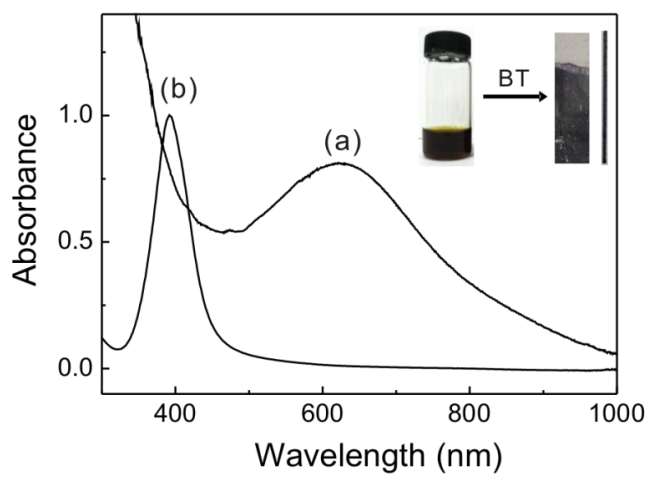

Figure 14. (a) UV-vis spectrum of the PEI-capped Ag film on a mica substrate formed by adding BT to the toluene phase. For comparison, the UV-vis spectrum of Ag nanoparticles is shown in (b). The inset shows the photograph of the Ag films transferred onto a separate glass or onto the inner wall of glass capillary.

As one expects from the intense SPR band at ~650 nm in the UV/vis spectra, strong Raman peaks of BT are observed, using a He/Ne laser at 632.8 nm, from the Ag film assembled on glasses. It must be a SERS spectrum of BT. A fairly intense SERS spectrum of BT is also measured by focusing the laser light axially through the capillary wall, as shown in Figure 15a. The most intense SERS peaks of BT are observed from an Ag-coated capillary fabricated using a mixture of 1.0 mL of BT, 2 mL of toluene, and 5 mL of Ag sol comprised of 30 nm sized Ag nanoparticles. Subsequent experiments have thus been conducted using those capillaries.

In order to use those capillaries in probing the adsorption characteristics of other adsorbates, BT should not interfere with these molecules. BT can be desorbed from the PEI-stabilized Ag nanoparticles without disturbing the SERS activity of the Ag film. Figure 15b shows SERS spectrum taken after treatment of 0.1 M ethanolic borohydride through a capillary tube. It is remarkable that the SERS activity of the PEI-stabilized Ag is maintained even after the treatment with borohydride. When BT is readsorbed onto the Ag substrate, the SERS spectrum is restored, as shown in 15c.

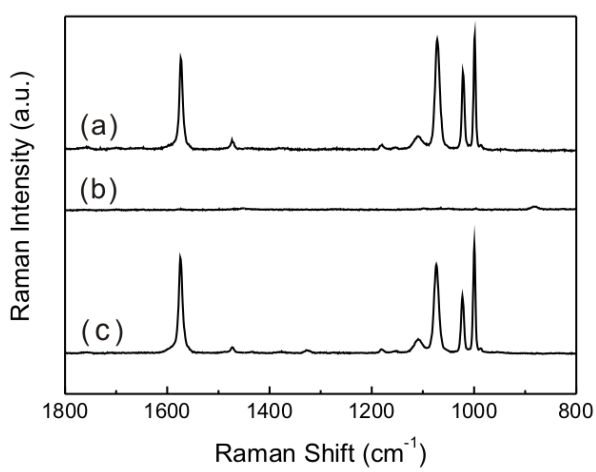

Figure 15. SERS spectra of BT adsorbed on PEI-stabilized Ag film on a glass substrate measured (a) as prepared and (b) after treating with 0.1 M borohydride for 30 min, and then (c) after readsorption of BT (treating with 1 mM BT for 1 hr).

Biochemical Identification. SERS spectra of a few compounds of biological significance, i.e., aqueous solutions of adenine (DNA base) and riboflavin (biosynthetic cofactor) are shown in Figure 16. The observed SERS spectral patterns of adenine and riboflavin are very similar to the reported data.[48,90] The ready acquisition of Raman spectra for small amounts of substances of biological importance is very promising. Therefore, it is worth examining the detection limit of the present methodology for biological compounds. In this light, a series of Raman spectra was measured by flowing an adenine solution at various concentrations ranging from 10^{-4} to 10^{-8} M through the Ag-coated capillary. In all cases, the Raman peak intensities reached a maximum value within 10 min. Figure 17a shows the SERS spectra obtained after 10 min of flow of adenine at various concentrations. In agreement with the previous reports, one distinct band is observed at 734 cm^{-1}, along with a series of weak bands in the region 1200−1500 cm^{-1}; all these bands were assigned previously to the skeletal vibration modes.[48] Figure 17b shows the intensity of the adenine peak at 734 cm^{-1} drawn versus the concentration of adenine solution. It is seen that the SERS signal attains a plateau value when the adenine concentration is above 5×10^{-6} M, probably due to the full coverage of adenine molecules onto silver. When the adenine concentration is lower than 10^{-6} M, the number of adsorbed adenine molecules decreases, resulting in weaker SERS signals. Nonetheless, it can be detected as low as 2.0×10^{-8} M of adenine with an S/N ratio of 4.5 ± 1.0; the detection limit would then be 1.0×10^{-8} M based on an S/N ratio of 3. Based on these promising results, it is attempted to detect dipicolinic acid, a signature molecule for bacterial spores.

Dipicolinic acid is an excellent marker molecule for bacterial spores, including those of *Bacillus anthracis* (anthrax).[91] The sensitivity of SERS, combined with its molecular specificity, suggests that SERS would be well suited for the detection of spores through identification of dipicolinic acid.[92] However, the affinity of dipicolinic acid for Ag or Au surfaces is known to be lower than that of even pyridine.[93] The silver-coated glass capillary can nonetheless be used to detect

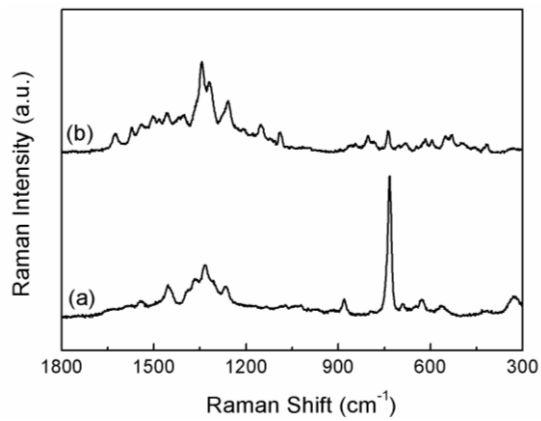

Figure 16. SERS spectra of (a) adenine and (b) riboflavin on Ag nanoparticles coated on the inner wall of glass capillaries.

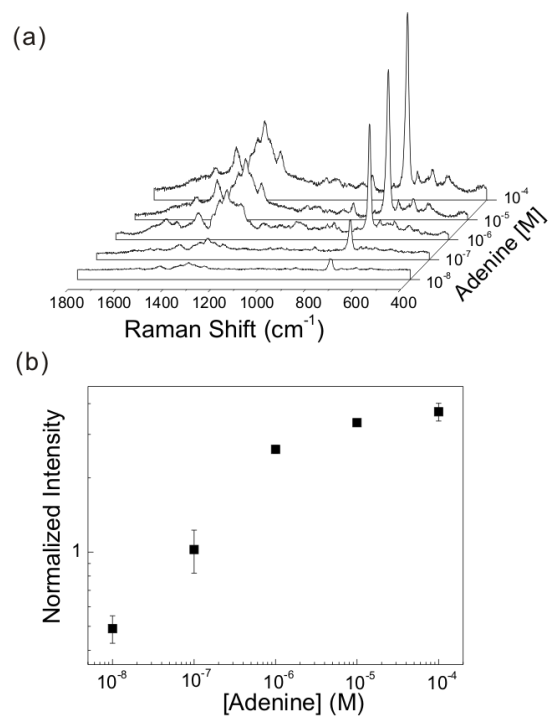

Figure 17. (a) A series of SERS spectra of adenine at various concentrations ranging from 10^{-4} to 10^{-8} M flowed into the Ag-coated capillary. (b) SERS intensity of the ring breathing band of adenine at 734 cm^{-1} normalized with respect to that of a silicon wafer at 520 cm^{-1} versus the concentration of adenine.

dipicolic acid down to a sub-micro molar regime. As similarly to adenine, a series of Raman spectra were taken by flowing a dipicolic acid solution at 10^{-3} - 10^{-7} M through an Ag-coated capillary in Figure 18a. The most distinct band was identified, immediately after the flow of the solution, at 1010 cm^{-1} that could be assigned to the ring breathing vibration of the pyridine ring, and about 10 min was required to reach a steady state. Figure 18b shows the intensity of the ring breathing band at 1010 cm^{-1} drawn versus the concentration of dipicolinic acid solution. Based on an S/N ratio of 3, the detection limit is estimated to be 1.0×10^{-7} M. This clearly suggests that our Ag-coated capillary is an invaluable device for the analysis of effluent chemicals by SERS.

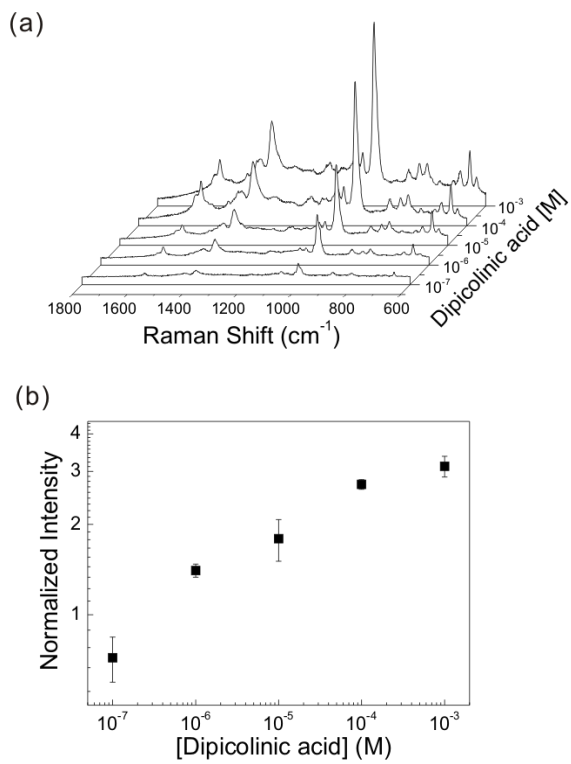

Figure 18. (a) A series of SERS spectra of dipicolinic acid at various concentrations ranging from 10^{-3} to 10^{-7} M flowed into the Ag-coated capillary. (b) SERS intensity of dipicolinic acid at 1010 cm^{-1} normalized with respect to that of a silicon wafer at 520 cm^{-1} versus the concentration of dipicolinic acid.

Identification of Anionic Dye Molecule: Sulforhodamine B (SRB). SRB (Figure 19a) is a typical negatively charged dye.[94] Figure 19b shows the UV-vis absorption spectrum of its aqueous 10^{-5} M solution; the absorbance occurred mainly between 460 and 610 nm, and the absorption maximum was observed at 563 nm. Figures 19c and d show the normal Raman (NR) spectra of aqueous 10^{-5} and 0.1 M solutions of SRB obtained using 514.5- and 632.8-nm as the excitation sources, respectively. As expected from the UV-vis absorption spectrum, only a strong fluorescence background was seen in the NR spectrum obtained using a 514.5-nm radiation (10^{-5} M of SRB): no peak was identifiable even in an expanded spectrum. In the NR spectrum recordedat 632.8-nm, however, a few bands were identifiable at least on using a concentrated solution (0.1 M of SRB). The bands at 1646, 1528, 1508, 1358, and 1282 cm^{-1} shown in Figure 19d (inset) are the characteristic features of xanthene dyes.

SERS activity of the PEI-capped Ag nanoparticle film was evaluated by comparing with a HNO_3-etched Ag foil, as shown in Scheme 2. The Ag foil that was etched with concentrated HNO_3 for 15 s exhibited a strong SERS activity. The SERS signal of BT on a PEI-capped Ag film was 5-fold more intense than that on a HNO_3-etched Ag foil (data not shown), indicating the usefulness of the PEI-capped Ag film as a SERS substrate. As shown in Figure 20a, on recording the SERS spectrum of HNO_3-etched Ag foil under the flow of 10^{-5} M solution of SRB at a 514.5-nm excitation source, it was difficult to observe the characteristic peaks of SRB. A similar spectrum of PEI-capped Ag nanoparticles (Figure 20b) coated on a glass capillary, through which a stream of 10^{-5} M SRB was passed, showed the characteristic peaks of SRB. This was as expected considering that SRB would be present mostly as an anionic species and PEI would be in a protonated state, thus forming an ion pair at pH 7, the pH of a 10^{-5} M solution of SRB. A zeta potential measurement indicates that the PEI-capped Ag nanoparticles are positively charged up to +10.2 mV. On the other hand, it was noted from the open-circuit potential measurement that the surface of the HNO_3-etched Ag foil was negatively charged; hence, it repelled SRB, resulting in a failure to generate a Raman signal.[95]

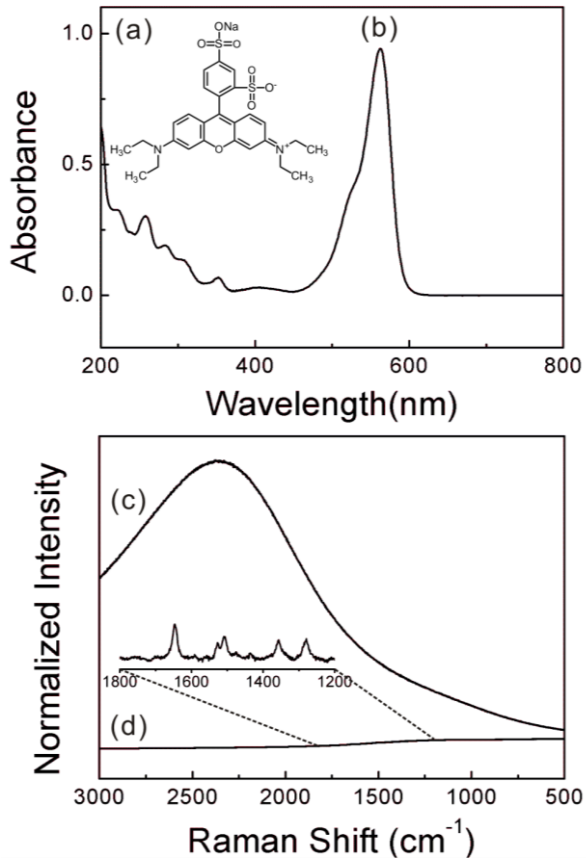

Figure 19. (a) Structure of SRB. (b) UV-vis absorption spectrum of 10^{-5} M aqueous solution of SRB. NR spectra of (c) 10^{-5} M and (d) 0.1 M aqueous solution of SRB measured using 514.5- and 632.8-nm excitation sources, respectively. The inset in (d) shows the magnified spectrum in the 1800 ~ 1200 cm^{-1} region.

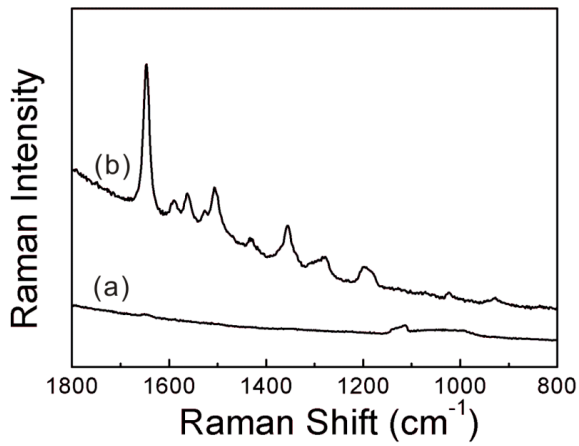

Figure 20. SERS spectrum of 10^{-5} M aqueous solution SRB measured using (a) a HNO_3-etched Ag foil and (b) a PEI-capped Ag nanoparticle film as the SERS substrate: a 514.5-nm excitation source was used.

The net cationic charge of PEI, as well as the net anionic charge of SRB depends on the pH of the solution.[84,96] On lowering the solution pH, the net cationic charge of PEI increases, whereas the net anionic charge of SRB decreases. The electrostatic attraction between PEI and SRB is thus dependent on the pH of the solution. Figure 21a shows a series of Raman spectra recorded in a stream of 10^{-7} M aqueous solution of SRB at varying pH from 1 to 10 through a glass capillary coated with PEI-capped Ag nanoparticles. All the spectra were obtained using 514.5-nm as the excitation source. In this measurement, the pH was adjusted using either HCl or NaOH. As observed from Figure 21b, the band intensity of the xanthene rings mode at ~1650 cm^{-1} is plotted against the solution pH, and the most intense Raman spectrum was seen at approximately pH 4. This finding implies that at an even lower pH, SRB would be present in a neutral form due to protonation, but at a higher pH, PEI would gradually get neutralized. The infeasible attraction at pH values lower and higher than 4 is also evident from the fluorescence backgrounds in Figure 21a. SRB is not in contact with Ag but forms an ion pair with PEI; hence, the fluorescence signal of SRB can be enhanced by increasing

interaction with the PEI-capped Ag nanoparticles. As shown in Figure 21c, a graph of the background fluorescence intensity (recorded at 2500 cm^{-1}) versus the pH of the solution shows the strongest fluorescence at pH 4; this finding is consistent with the Raman signal data.

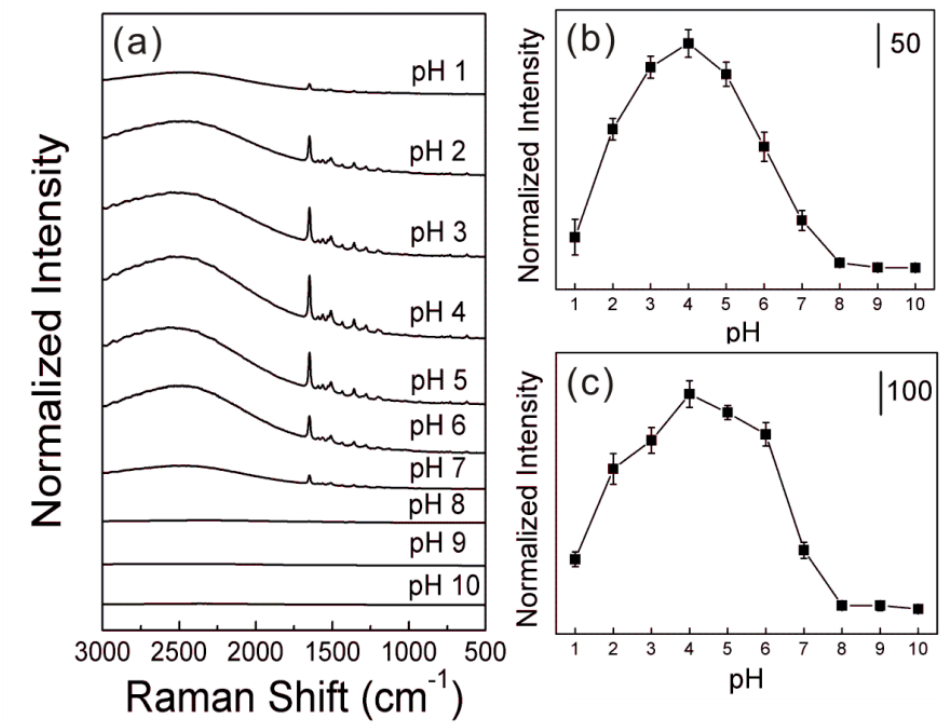

Figure 21. (a) A series of SERS spectra obtained under the flow of 10^{-7} M aqueous solution of SRB at varying pH from 1 to 10 through a PEI-capped Ag capillary tube. The flow rate was 0.19 mL/min. (b) The peak intensity of the xanthenes ring mode at 1650 cm^{-1} plotted against the pH of the solution in (a). (c) Intensity of the background fluorescence at 2500 cm^{-1} in (a) plotted against the pH of the solution. For (b) and (c), the error bars indicate the average and standard deviation of 10 different measurements.

Subsequently, the efficacy of detection of the Raman signal of SRB was measured. Figure 22a displays a series of Raman spectra measured under the flow of 10^{-10} ~ 10^{-5} M aqueous solutions of SRB through a glass capillary coated with PEI-capped Ag nanoparticles at pH 4. Again, all the spectra were obtained using a 514.5-nm radiation as the excitation source. The band intensity of the xanthenes ring mode at ~1650 cm^{-1} versus the concentration of SRB is illustrated in Figure 22b. On the other hand, Figure 22c shows the intensity of the background fluorescence from Figure 22a versus the concentration of SRB. The normalized Raman intensity, as well as the fluorescence intensity, shows a sigmoidal change with the logarithm of the SRB concentration, corresponding to Frumkin adsorption isotherm.[97,98] The Raman signal of SRB at 10^{-10} M is more than 3-fold greater than the noise level (see the expanded inset of Figure 22a), indicating a high probability of detecting sub-nanomolar concentrations of SRB by Raman spectroscopy using the PEI-capped Ag nanoparticle film as the SERS substrate.

For their normal lifespan, most cells need moderately narrow limits of pH around 7. The interaction of drugs with model membranes at neutral pH will then be worth studying. As noted above, the ion-pair formation of PEI with SRB is less likely at pH 7 than that at pH 4. This is evident from a series of Raman spectra (Figure 23a) measured under the flow of 10^{-10} ~ 10^{-5} M aqueous solutions of SRB at pH 7 through a glass capillary coated with PEI-capped Ag nanoparticles by using 514.5-nm as the excitation source. Although the peak intensities were reduced in comparison to those obtained at pH 4, as shown in Figure 22a, the Raman peaks of SRB as well as their background fluorescence were distinguishable at sub-nanomolar concentrations. The Raman intensity and the background fluorescence plotted against the logarithm of SRB concentration are shown in Figures 23b and c, respectively. Although the absolute values in the ordinates are smaller than those in Figures 22b and c, sigmoidal variations were again observed, and the detection limit of SRB at pH 7 appears comparable to that at pH 4, illustrating the usefulness of the PEI-capped Ag nanoparticle film in the detection of anionic drugs by SERS.

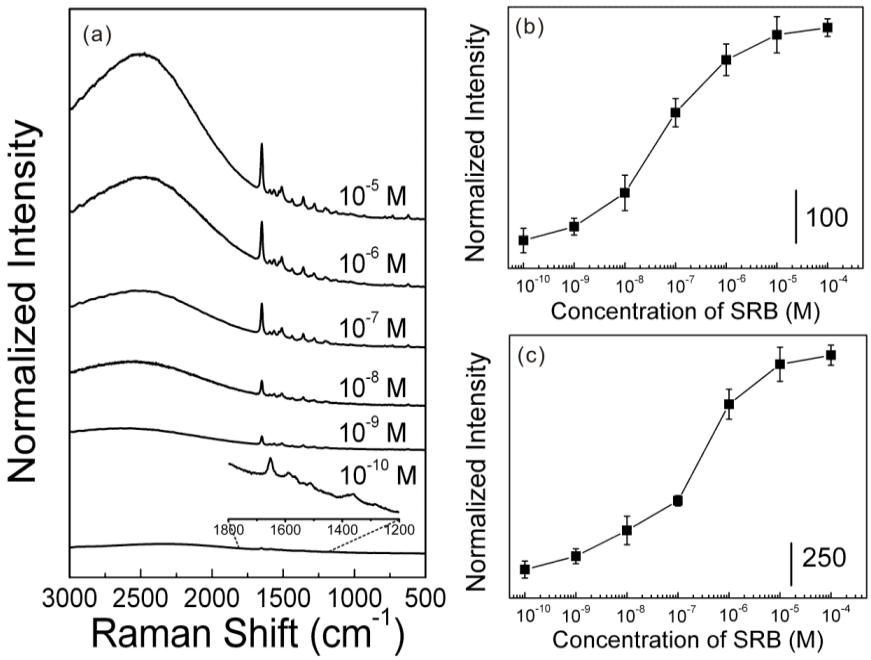

Figure 22. (a) A series of Raman spectra obtained under the flow of 10^{-5} ~ 10^{-10} M aqueous solutions of SRB at pH 4 through a glass capillary coated with PEI-capped Ag nanoparticles. All spectra were obtained using a 514.5-nm radiation as the excitation source. The inset shows the expanded spectrum obtained at 10^{-10} M of SRB. (b) The peak intensity of the xanthenes ring mode at 1650 cm^{-1} in (a) plotted against the SRB concentration. (c) The intensity of the background fluorescence at 2500 cm^{-1} in (a) plotted against the SRB concentration. For (b) and (c), the error bars indicate the average and standard deviation of 10 different measurements.

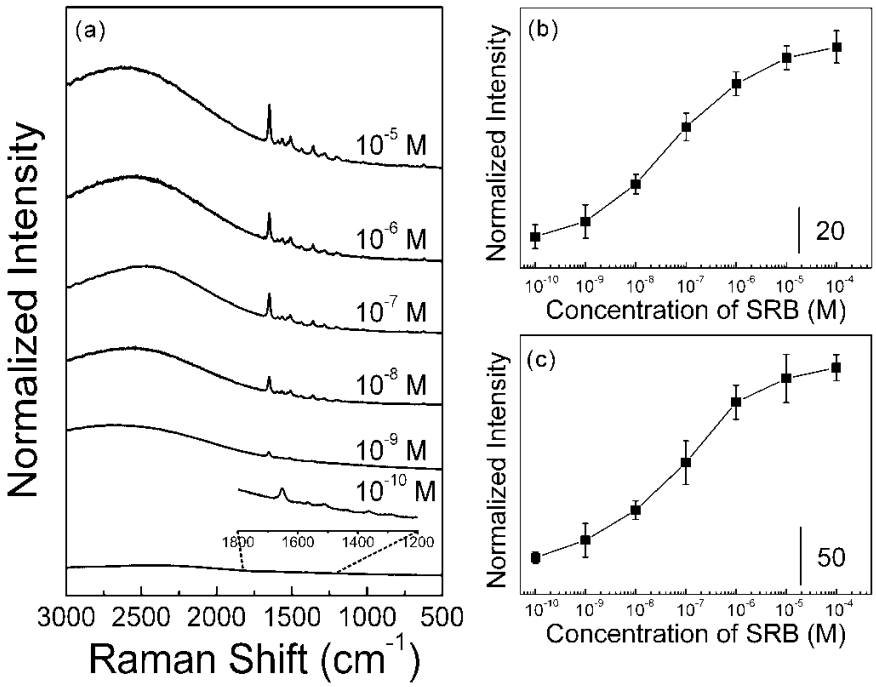

Figure 23. (a) A series of Raman spectra obtained under the flow of 10^{-5} ~ 10^{-10} M aqueous solutions of SRB at pH 7 through a glass capillary coated with PEI-capped Ag nanoparticles; all spectra obtained using a 514.5-nm radiation as the excitation source. (b) The peak intensity of the xanthenes ring mode at 1650 cm^{-1} and (c) the intensity of the background fluorescence at 2500 cm^{-1} in (a) plotted against the SRB concentration. For (b) and (c), the error bars indicate the average and standard deviation of 10 different measurements.

Identification of Cationic Dye Molecule: Rhodamin-123 (R123). It is difficult to detect the presence of cationic drugs like R123 by using PEI-capped Ag nanoparticles. The structure and UV-vis absorption spectrum of 10^{-5} M aqueous solution of R123 are shown in Figures 24a and b, respectively. The absorption occurred mainly between 420 and 550 nm, with the absorption maximum observed at 500 nm. The NR spectra of 10^{-5} and 0.1 M aqueous solutions of R123 obtained using 514.5- and 632.8-nm radiations as the excitation sources, respectively, are

shown in Figures 25a and b. As anticipated from the UV-vis absorption spectrum, only strong background fluorescence was observed in the NR spectrum by using a 514.5-nm excitation source (10^{-5} M of R123); however, several peaks were seen in the NR spectrum obtained at 632.8-nm, especially for a concentrated solution (0.1 M of R123). The peaks at 1643, 1568, 1505, 1369, and 1187 cm^{-1} in the inset of Figure 25b are characteristic of xanthene dyes,[99,100] and the HNO_3-etched Ag foil attracted R123 because of its negative charge. This finding was confirmed from the Raman spectrum (Figure 24c) obtained using a 514.5-nm source after soaking Ag foil in 10^{-5} M aqueous solution of R123. No distinguishable peak was detected, as expected, when R123 solution was passed through a glass capillary coated with PEI-capped Ag nanoparticles (data not shown).

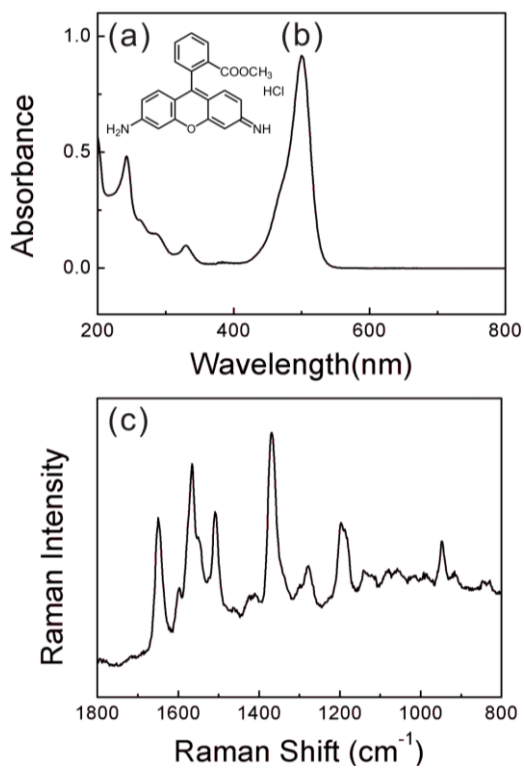

Figure 24. (a) Structure of R123. (b) UV-vis absorption spectrum of 10^{-5} M aqueous solution of R123. (c) SERS spectrum of aqueous 10^{-5} M solution of R123 measured during the flow over a HNO_3-etched Ag foil.

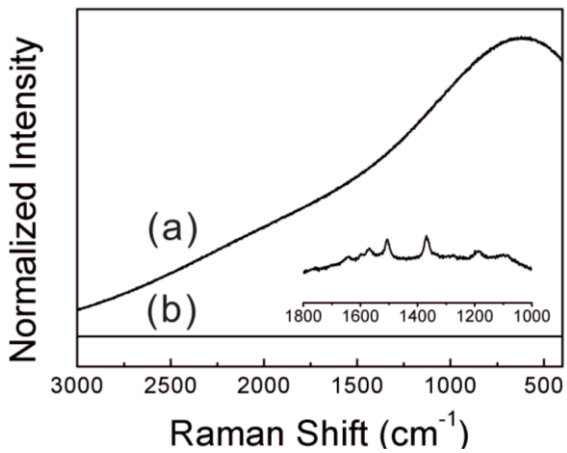

Figure 25. The normal Raman spectra of (a) 10^{-5} M and (b) 0.1 M aqueous solution of R123 obtained using 514.5- and 632.8-nm excitation sources, respectively. The inset shows the expanded spectrum measured at 0.1 M of R123.

To identify R123 by using a PEI-capped Ag nanoparticle film, it is necessary to deposit an anionic polyelectrolyte onto PEI. In case of Ag nanoparticles that are highly SERS active, the adsorption of R123 even onto the anionic polyelectrolyte would be detectible because of electromagnetic enhancement. Furthermore, the fluorescence signal of R123 was expected to increase markedly with an increase in the gap between Ag and R123 up to some distance. Two different anionic polyelectrolytes were used in this work: PAA, a weak polyelectrolyte, and PSS, a strong polyelectrolyte.[101] A 10^{-3} M aqueous solution of PAA or PSS was injected into a glass capillary previously coated with PEI-capped Ag nanoparticles, and it was allowed to stand for 30 min before blowing out the remaining solution. The glass capillary thus contained either PAA/PEI- or PSS/PEI-capped Ag nanoparticles. However, the net cationic charge of R123 as well as the net anionic charge of PAA/PEI or PSS/PEI was dependent on the pH of the solution. Considering the importance of neutral pH in living systems, the Raman spectra mainly at pH 7 were measured under a flowing solution of R123 through a glass capillary coated with PAA/PEI- or PSS/PEI-capped Ag nanoparticles: The zeta potentials of PSS/PEI- and PAA/PEI-capped Ag

nanoparticles at neutral pH were measured to be -35.4 and -17.6 mV, respectively. In order to estimate the amount of R123 dyes being adsorbed onto the anionic polyelectrolyte-coated Ag nanoparticles, a QCM experiment was conducted. A polyelectrolyte (PSS or PAA)-coated Au electrode was fixed onto a crystal holder using a conductive adhesive and the holder was fastened onto the QCM cell through the Kalez O-rings. Pure water was first added into the QCM cell and left to stabilize, after which 10^{-7} M aqueous solution of R123 was injected into the cell, monitoring the frequency change as a function of time (data not shown). The QCM frequency decreased abruptly by as much as 2 ~ 15 Hz. According to the Sauerbrey equation ($\Delta m = -0.884\ \Delta f$ ng/Hz),[55] the measured frequency change (Δf) corresponded to the adsorption of 1.32×10^{-8} and 1.77×10^{-9} g (Δm) of R123 onto the surfaces of PSS and PAA, respectively. Considering the apparent area of the QCM electrode, the number of R123 molecules bound per 1 μm^2 of PSS and PAA will then be 1.05×10^6 and 1.40×10^5, respectively. Consulting the data in Figure 26d, those numbers of R123 molecules can readily be identified by SERS.

The Raman spectra measured as a function of R123 concentration (10^{-10} ~ 10^{-5} M) by using a capillary coated with PAA/PEI-capped Ag nanoparticles is shown in Figure 26a. A 514.5-nm radiation was used as the excitation source; hence, the Raman spectra must be SERRS spectra because of which the Raman peaks could be identified even at sub-nanomolar concentrations, even though most R123 molecules may be far from the Ag nanoparticles. The normalized Raman intensity of the xanthenes mode at ~1650 cm^{-1} plotted against the R123 concentration is displayed in Figure 26b. Here as well, sigmoidal variation was obtained, indicating a Frumkin-type adsorption isotherm. A similar result could be obtained using a capillary coated with PSS/PEI-capped Ag nanoparticles (Figure 26c) for Raman spectra measured using a PSS/PEI-capped Ag nanoparticle film. The Raman signal in Figure 26c is of the order of a magnitude stronger than that in Figure 26a, which could be explained by presuming that the net anionic charge of the PSS/PEI-capped Ag film would be larger than that of the PAA/PEI-capped Ag

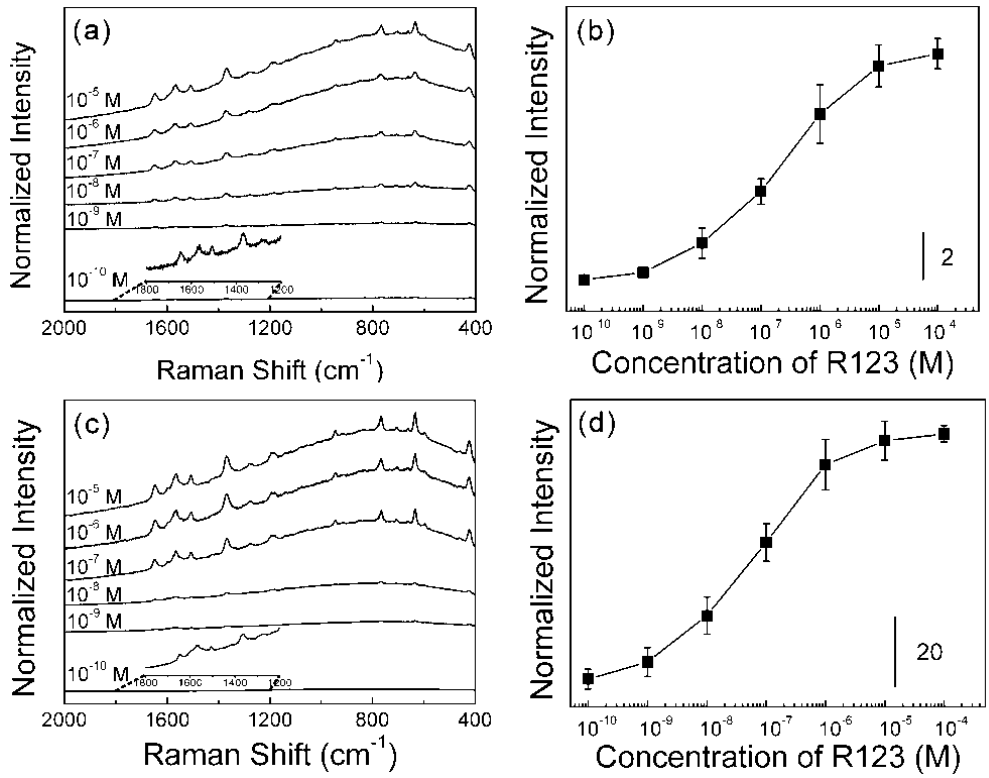

Figure 26. A series of Raman spectra obtained under the flow of 10^{-5} ~ 10^{-10} M aqueous solutions of R123 at pH 7 through a glass capillary coated with (a) PAA/PEI- and (c) PSS/PEI-capped Ag nanoparticles. All spectra were obtained using a 514.5-nm radiation as the excitation source. (b) The peak intensity of the xanthenes ring mode at 1650 cm^{-1} in (a) and (d) that in (c), drawn against the R123 concentration. For (b) and (d), the error bars indicate the average and standard deviation of 10 different measurements.

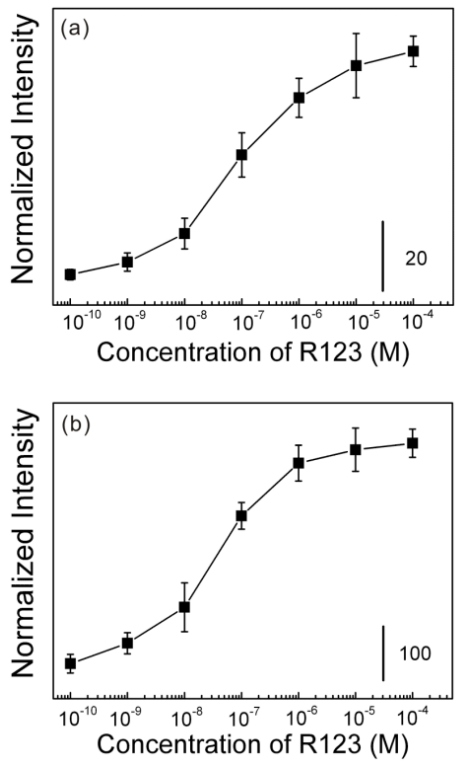

Figure 27. (a) The intensity of the background fluorescence at 600 cm^{-1} in Figure 26a drawn against the R123 concentration. (b) A similar plot drawn for the background fluorescence in Figure 26c. For (a) and (b), the error bars indicate the average and standard deviation of 10 different measurements.

film. This may be attributed to the strong polyelectrolyte nature of PSS. A more intense Raman signal is more evident from Figure 26d in which the xanthenes band intensity at ~1650 cm^{-1} is plotted against the R123 concentration. The interaction of R123 with the anionic polyelectrolytes was also confirmed from the background fluorescence as observed in Figures 27a and b in which the background fluorescence intensities from Figures 26a and c, respectively, are plotted against the concentration of R123. Thus, undoubtedly, cationic drug molecules can also be detected by Raman spectroscopy using a PEI-capped Ag nanoparticle film as the SERS substrate.

4. Summary and Conclusion

PEI can function simultaneously as a reducing and stabilizing agent to form amine-functionalized Ag nanoparticles, which can further be fabricated into a 2D film not only onto a glass slide but also onto the inner surface of a glass capillary. It is known that PEI is a cationic polyelectrolyte; therefore, it was attempted to demonstrate the usefulness of the PEI-capped Ag nanoparticle film, especially in detecting charged dye molecules by SERS and MEF phenomena. In this light, 14 nm sized, PEI-capped Ag nanoparticles were first produced in an aqueous solution and further fabricated into a PEI-capped, aggregated 2D film. The SERS activity of the PEI-capped Ag nanoparticle film, tested using a prototype organic thiol such as BT, was 5-fold greater than that of a HNO_3-etched Ag foil. In fact, anionic dye molecule, SRB, can be detected not only by SERS but also by MEF at subnanomolar concentrations. On the other hand, it was difficult to detect cationic dyes such as R123 because of the positive charges of PEI; nonetheless, it is found that even R123 could be detected at subnanomolar concentrations not only by SERS but also by MEF, by deposition of an anionic polyelectrolyte such as PSS and PAA onto the PEI-capped Ag nanoparticles. Therefore, the PEI-capped Ag nanoparticle film serves as a useful indicator to detect charged drug molecules by SERS and MEF.

2.3. References

1. Gupta, R.; Dyer, M. J.; Weimer, W. A. *J. Appl. Phys.* **2002**, *92*, 5264.
2. Agrawal, V. V.; Kulkarni, G. U.; Rao, C. N. R. *J. Phys. Chem. B* **2005,** *109*, 7300.
3. Rao, C. N. R.; Kulkarni, G. U.; Thomas, P. J.; Edwards, P. P. *Chem.-Eur. J.* **2002**, *8*, 28.
4. Kulkarni, G. U.; Thomas, P. J.; Rao, C. N. R. *Encyclopedia of Nanoscience and Nanotechnology*; Nalwa, H. S., Ed.; American Scientific Publishers: Los Angeles, 2004; Vol. 5, p 277.
5. Terenishi, T.; Miyake, M. *Encyclopedia of Nanoscience and Nanotechnology*; Nalwa, H. S., Ed.; American Scientific Publishers: Los Angeles, 2004; Vol. 5, p 421.
6. Kulkarni, G. U.; Thomas, P. J.; Rao, C. N. R. In *Recent Advances in the Chemistry of Nanomaterials*; Rao, C. N. R., Mueller, A., Cheetham, A. K., Eds.; Wiley-VCH: Weinheim, 2004; p 51.
7. Rao, C. N. R.; Kulkarni, G. U.; Thomas, Agrawal, V. V.; Saravanan, P. *J. Phys. Chem. B* **2003**, *107*, 7391.
8. Scholz, F.; Hasse, U. *Electrochem. Commun.* **2005**, *7*, 541.
9. Wu, Y.; Li, Y.; Ong, B. S. *J. Am Chem. Soc.* **2006**, *128*, 4202.
10. Kolliopoulou, S.; Dimitrakis, P.; Normand, P.; Zhang, H. L.; Cant, N.; Evans, S. D.; Paul, S.; Pearson, C.; Molloy, A.; Petty, M. C.; Tsoukalas, D. *J. Appl. Phys.* **2003**, *94*, 5234.
11. Zoy, A.; Nassiopoulos, A. A.; Nassiopoulou, A. G. *Nanotechnology* **2007**, *18*, 345608.
12. Whetten, R. L.; Khoury, J. T.; Alvarez, M. M.; Murthy, S.; Vezmar, I.; Wang, Z.; Stephens, P. W.; Clevend, Ch. L.; Luedtke, W. D.; Landman, U. *Adv. Mater.* **1996**, *8*, 428.
13. Korgel, B. A.; Fullam, S.; Connolly, S.; Fitzmaurice, D. *J. Phys. Chem. B* **1998**, *102*, 8379.
14. Lundgren, A. O.; Björefors, F.; Olofsson, L. G. M.; Elwing, H. *Nano Lett.* **2008**, *8*, 3989.

15. Harfenist, S. A.; Wang, Z. L.; Whetten, R. L.; Vezmar, I.; Alvarez, M. M. *Adv. Mater.* **1997**, *9*, 817.
16. Pileni, M. P. *New J. Chem.* **1998**, *22*, 693.
17. Abe, K.; Hanada, T.; Yoshida, Y.; Tanigaki, N.; Takiguchi, H.; Nagasawa, H.; Nakamoto, M.;Yamaguchi, T.; Yase, K. *Thin Solid Films* **1998**, *327*, 524.
18. Sun, S.; Murray, C. B. *J. Appl. Phys.* **1999**, *85*, 4325.
19. Petit, C.; Taleb, A.; Pileni, M. P. *J. Phys. Chem. B* **1999**, *103*, 1805.
20. Thomas, P. J.; Kulkarni, G. U.; Rao, C. N. R. *J. Phys. Chem. B* **2000**, *104*, 8138.
21. Schmid, G.; Baumle, M.; Beyer, N. *Angew. Chem., Int. Ed.* **2000**, *39*, 181.
22. Kiely, C. J.; Fink, J.; Zheng, J. G.; Brust, M.; Bethell, D.; Schiffrin, D. J. *Adv. Mater.* **2000**, *12*, 640.
23. Srnova, S. I.; Vlckova, B.; Bastl, Z.; Hasslett, T. L. *Langmuir* **2004**, *20*, 3407.
24. He, S. T.; Xie, S. S.; Yao, J. N.; Gao, H. J.; Pang, S. J. *Appl.Phys.Lett.* **2002**, *81*, 150.
25. Chi, L. F.; Rakers, S.; Hartig, M.; Fuchs, H.; Schmid, G. *Thin Solid Films* **1998**, *327*, 520.
26. Brown, J. J.; Porter, J. A.; Daghlian, C. P.; Gibson, U. J. *Langmuir* **2001**, *17*, 7966.
27. Sastry, M.; Gole, A.; Patil, V. *Thin Solid Films* **2001**, *384*, 125.
28. Kumar, A.; Mandal, S.; Mathew, S. P.; Selvakannan, P. R.; Mandale, A. B.; Chaudhari, R. A.; Sastry, M. *Langmuir* **2002**, *18*, 6478.
29. Reincke, F.; Hickey, S. G.; Kegel, W. K.; Vanmaekelbergh, D. *Angew.Chem., Int. Ed.* **2004**, *43*, 458.
30. Lee, K. Y.; Cheong, G. W.; Han, S. W. *Colloids Surf. A* **2006**, *275*, 79.
31. Kim, K.; Lee, H. B.; Lee, J. W.; Park, H. K.; Shin, K. S. *Langmuir* **2008**, *24*, 7178.
32. Stöber, W.; Fink, A.; Bohn, E. *J. Colloid. Interf. Sci.* **1968**, *26*, 62.
33. Torigoe, K.; Esumi, K. *Langmuir* **1992**, *8*, 59.
34. Gangopadhayay, A. K.; Chakravorty, A. *J. Chem. Phys*. **1961**, *35*, 2206.
35. Mulvaney, P. *Langmuir* **1996**, *12*, 788.

36. Sun, X.; Jiang, X.; Dong, S.; Wang, E. *Macromol. Rapid Commun*. **2003**, *24*, 1024.
37. Sun, X.; Dong, S.; Wang, E. *J. Colloid Interface Sci*. **2005**, *288*, 301.
38. Leff, D. V.; Brandt, L.; Heath, J. R. *Langmuir* **1996**, *12*, 4723.
39. Carotenuto, G.; Nicolais, L. *Composites: Part B* **2004**, *35*, 385.
40. Selva, S. T.; Ono, Y.; Nogami, M. *Mater. Lett.* **1998**, 37, 156.
41. Grabar, K. C.; Freeman, R. G.; Hommer, M. B.; Natan, M. J. *Anal. Chem.* **1995**, *67*, 735.
42. Osawa, M.; Matsuda, N.; Yoshii, K.; Uchida, I. *J. Phys. Chem.* **1994,** *98*, 12702.
43. Widrig, C. A.; Chung, C.; Porter, M. D. *J. Electroanal. Chem.* **1991,** *310*, 335.
44. Yan, M.; Zhan, S.; Zhou, X.; Liu, Y.; Feng, L.; Lin, Y.; Zhang, Z.; Hu, J. *Langmuir* **2008**, *24*, 8707.
45. Skadtchenko, B. O.; Aroca, A. *Spectrochim. Acta, Part A* **2001**, *57*, 1009.
46. Tanakaa, T.; Nakajima, A.; Watanabe, A.; Ohnoa, T.; Ozaki, Y. *Vib. Spectrosc.* **2004**, *34*, 157.
47. Erol, M.; Han, Y.; Stanley, S. K.; Stafford, C. M.; Du, H.; Sukhishvili, S. *J. Am. Chem. Soc.* **2009**, *131*, 7480.
48. Maxwell, D. J.; Emory, S. R.; Nie, S. *Chem. Mater.* **2001**, *13*, 1082.
49. Yeqiu, L.; Jinlian, H.; Yong, Z.; Zhuohong, Y. *Carbohydr. Polym.* **2005**, *61*, 276.

50. Akutsut, H.; Seelig, J. *Biochemistry* **1981**, *20*, 7366.
51. Beschiaschvili, G.; Seelig, J. *Biochemistry* **1990**, *29*, 52.
52. Barry, J.; Fritz, M.; Brender, J. R.; Smith, P. E. S.; Lee, D. -K.; Ramamoorthy, A. *J. Am. Chem. Soc.* **2009**, *131*, 4490.
53. Reuter, M.; Schwieger, C.; Meister, A.; Karlsson, G.; Blume, A. *Biophys. Chem.* **2009**, *144*, 27.
54. Sugawara, M.; Takekuma, Y.; Yamada, H.; Kobayashi, M.; Iseki, K.; Miyazaki, K. *J. Pharm. Sci.* **1998**, *87*, 960.
55. Krämer, S. D.; Braun, A.; Jakits-Deiser, C.; Wunderli-Allenspach, H. *Pharm. Res.* **1998**, *15*, 739.

56. Nabiev, I. R.; Morjani, H.; Manfait, M. *Eur. Biophys. J.* **1991**, *19*, 311.

57. Quinn, J. G.; O'Neill, S.; Doyle, A.; McAtamney, C.; Diamond, D.; MacCraith, B. D.; O'Kennedy R. *Anal. Biochem.* **2000**, *281*, 135.

58. Surewicz, W. K.; Leyko, W. *Biochim. Biophys. Acta*, **1981**, *643*, 387.

59. Bagalkot, V.; Zhang, L.; Levy-Nissenbaum, E.; Jon, S.; Kantoff, P. W.; Langer, R.; Farokhzad , O. C. *Nano Lett.* **2007**, *7*, 3065.

60. Sanganahalli, B. G.; Joshi, P. G.; Joshi, N. B. *Life Sci.* **2000**, *68*, 81.

61. Bacia, K.; Kim, S. A.; Schwille, P. *Nat. Method* **2006**, *3*, 83.

62. Moskovits, M. *Rev.Mod. Phys.***1985**, *57*, 783.

63. Chang, R. K.; Furtak, T. E. 1982. Surface Enhanced Raman Scattering. Plenum Press, New York.

64. Kneipp, K.; Wang, Y.; Kneipp, H.; Perelman, L. T.; Itzkan, I.; Dasari, R. R.; Feld, M. S. *Phys. Rev. Lett*. **1997**, *78*, 1667.

65. Nie, S.; Emory, S. R. *Science* **1997**, *275*, 1102.

66. Yang, Y.; Li, Z.-Y.; Yamaguchi, K.; Tanemura, M.; Huang, Z.; Jiang, D.; Chen, Y.; Zhou, F.; Nogami, M. *Nanoscale* **2012**, *4*, 2663.

67. Shanmukh, S.; Jones, L.; Driskell, J.; Zhao, Y.; Dluhy, R.; Tripp, R. A. *Nano Lett.* **2006**, *6*, 2630.

68. Betz, J. F.; Cheng, Y.; Rubloff, G. W. *Analyst* **2012**, *137*, 826.

69. Kao, P.; Malvadkar, N. A.; Cetinkaya, M.; Wang, H.; Allara, D. L.; Demirel, M. C. *Adv. Mater.* **2008**, *20*, 3562.

70. Halvorson, R. A.; Vikesland, P. J. *Environ. Sci. Technol*. **2010**, *44*, 7749.

71. Camden, J. P.; Dieringer, J. A.; Zhao, J.; Van Duyne, R. P. *Acc. Chem. Res.* **2008**, *41*, 1653.

72. Kerker, M. *Acc. Chem. Res.* **1984**, *17*, 271.

73. Stranahan, S. M.; Titus, E. J.; Willets, K. A. *ACS Nano* **2012**, *6*, 1806.

74. Lee, S. Y.; Hung, L.; Lang, G. S.; Cornett, J. E.; Mayergoyz, I. D.; Rabin, O. *ACS Nano* **2010**, *4*, 5763.

75. Campion, A.; Gallo, A. R.; Harris, C. B.; Robota, H. J.; Whitmore, P. M. *Chem. Phys. Lett.* **1980**, *73*, 447.

76. Kümmerlen, J.; Leitner, A.; Brunner, H.; Aussenegg, F. R.; Wokaun, A. *Mol. Phys.* **1993**, *80*, 1031.

77. Lakowicz, J. R. *Anal. Biochem.* **2001**, *298*, 1.

78. Smith, D. S.; Kostov, Y.; Rao, G. *Sens. Actuators, B: Chem.* **2007**, *127*, 432.

79. Sabanayagam, C. R.; Lakowicz, J. R. *Nucleic Acids Res.* **2007**, *35*, e13.

80. Kim, K.; Lee, H. B.; Lee, J. W.; Shin, K. S. *J. Colloid Interf. Sci.* **2010**, *345*, 103.

81. Kim, K.; Lee, J. W.; Lee, H. B.; Shin, K. S. *Langmuir* **2009**, *25*, 9697.

82. Lee, J. W.; Lee, H. B.; Kim, K.; Shin, K. S. *Anal. Bioanal. Chem.* **2010**, *397*, 557.

83. Lee, J. W.; Kim, K.; Shin, K. S. *Vib. Spectrosc.* **2010**, *53*, 121.

84. Kim, K.; Lee, J. W.; Choi, J. -Y.; Shin, K. S. *Langmuir* **2010,** *26*, 19163.

85. Kim, K.; Lee, J. W.; Shin, D.; Kim, K. Y.; Shin, K. S. *J. Phys. Chem. C* **2010**, *114*, 9917.

86. Ariga, K.; Ji, Q.; Hill, J. P.; Bando, Y.; Aono, M. *NPG Asia Mater.* **2012**, *4*, e17.

87. Costa, E.; Lloyd, M. M.; Chopko, C.; Aguiar-Ricardo, A.; Hammond, P. T. *Langmuir* **2012**, *28*, 10082.

88. Yeo, S. J.; Kang, H.; Kim, Y. H.; Han, S.; Yoo, P. J. *ACS Appl. Mater. Inter.* **2012**, *4*, 2107.

89. Grabar, K. C.; Freeman, R. G.; Hommer, M. B.; Natan, M. J. *Anal. Chem*. **1995**, *67*, 735.

90. Nirode, W. F.; Devault, G. L.; Sepaniak, M. J. *Anal. Chem.* **2000**, *72*, 1866.

91. Murrell, W. G. 1969. The bacteria spore. Academic Press, London, ch. 7

92. Bell, S. E. J.; Mackle, J. N.; Sirimuthu, N. M. S. *Analyst* **2005**, *130*,545.

93. Zhang, X; Young, M. A.; Lyandre, O.; Van Duyne, R. P. *J. Am. Chem. Soc*. **2005**, *127*, 4484.

94. Gole, A.; Sainkar, S. R.; Sastry, M. *Chem. Mater*. **2000**, *12*, 1234.

95. Oubre, C.; Nordlander, P. *J. Phys. Chem. B* **2004**, *108*, 17740.

96. Liu, S.; Zhao, X.; Li, Y.; Zhao, X.; Chen, M. *J. Chem. Phys*. **2009**, *130*, 234509.

97. Sun, M.; Xu, H. *ChemPhysChem* **2009**, *10*, 392.

98. Lombardi, J. R.; Birke, R. L. *J. Phys. Chem. C* **2008**, *112*, 5605.

99. Kim, K.; Lee, H. B.; Choi, J-Y; Kim, K. L.; Shin, K. S. *J. Phys. Chem. C* **2011**, *115*, 13223.

100. Kim, K.; Kim, K. L.; Lee, H. B.; Shin, K. S. *J. Phys. Chem. C* **2010**, *114*, 18679.

101. Ikeda, K.; Sato, J.; Fujimoto, N.; Hayazawa, N.; Kawata, S.; Uosaki, K. *J. Phys. Chem. C* **2009**, *113*, 11816.

Chapter 3

: Cyanide and Isocyanide SERS: A Tool to Detect Volatile Organic Compounds and Variation of Surface Potential of Metal Nanostructures

1. pH and Polyelectrolytes Effect on the SERS of 2,6-Dimethylphenylisocyanide (2,6-DMPI) on PEI-Capped Au Substrate
2. 2,6-DMPI-Adsorbed Gold Nanostructure: A SERS Sensory Device to Detect Volatile Organic Compounds (VOCs)
3. Cyanide SERS: A Useful Platform to Detect Both VOCs and Hazardous Metal Ions

3.1. pH and Polyelectrolytes Effect on the SERS of 2,6-Dimethylphenylisocyanide (2,6-DMPI) on PEI-Capped Au Substrate

1. Introduction

Noble metal nanoparticles have been intensely investigated in the last decade in conjunction with their potential use in microelectronics, chemical sensors, and a host of other applications.[1-4] This is particularly because noble metal nanoparticles have unique optical and electronic properties that are not found in either isolated atoms or bulk solids.[5] Thin films of organic molecules and polyelectrolytes can be placed on these nanoparticles and nanostructures. Self-assembled monolayers on nanoparticles, on the one hand, stabilize the reactive surface of the particle and, on the other hand, present organic functional groups at the particle-solvent interface.[6,7] These organic functional groups are useful for applications, such as immunoassays, that are dependent on chemical composition of the surface.[8,9] However, due to the high surface-to-volume ratio, metal nanoparticles must be more affected by environment compared to bulk metals so that although the coating of organics or polyelectrolytes can be an advantage in some case, it can also be a disadvantage where surface potential, for instance, is one of the key factors in the application of metal nanoparticles.

The layer-by-layer (LbL) deposition technique can be used to modify the surface of nanoparticles.[10-12] Over decades, polyelectrolytes have been utilized in the formation of new types of materials known as polyelectrolyte multilayers.[13] These thin films can easily be constructed using the LbL deposition technique first demonstrated by Decher et al.[14-19] During LbL deposition, a suitable substrate is dipped back and forth between dilute solutions of positively and negatively charged polyelectrolytes.[20] A small amount of polyelectrolyte is adsorbed during each dip, thereby reversing the surface charge for the gradual and controlled build-up of consecutive polycation-polyanion layers. The LbL approach can therefore provide a route to tailor the surface characteristics of nanoparticles. Since nanoparticles are

then endowed with a well-defined surface charge, either positive or negative, their stable dispersions in aqueous solutions are secured. There is one difficulty that the high surface curvature may restrict polymer adsorption.[21,22] Poor polymer coverage can thereby decrease the stability of colloidal suspensions, especially with the smallest sized particles.

It is certainly expected that the physicochemical properties of nanoparticles will change, although to a small degree, upon the deposition of polyelectrolytes.[23] UV/vis spectrometry can provide a partial assurance of the changes in surface characteristics of nanoparticles. For instance, the peak plasmon absorption wavelength of the gold nanoparticles has been observed to red-shift after each adsorption step of polyelectrolytes. Such red-shift is usually attributed to a change in the local dielectric constant around the gold nanoparticles.[24-26] It is unclear how much the surface potential of gold nanoparticles itself is subject to change by the deposition of polyelectrolytes, however. Unfortunately, no device is yet available to measure the surface potential of nanoparticles directly.

Very recently, it has been reported that a large Raman peak shift is observed for the NC stretching band of 1,4-phenylenediisocyanide (1,4-PDI) situated at the hot spot which is the gap between gold nanoparticles and the gold wire electrode when gold nanoparticles are exposed to polar organic vapor, such as acetone and ammonia.[27] The peak shift amounted to as much as 22 cm^{-1}, corresponding to the variation of surface potential of Au nanoparticles from +0.7 V to -0.6 V vs a saturated Ag/AgCl electrode. These observations clearly suggested that the peak position of the NC stretching band can be used as an indicator of the surface potential of Au nanoparticles.

In section 2, it is demonstrated that PEI-capped Au nanoparticles can be fabricated into a two-dimensional film not only on planar glasses but also on the inside surfaces of capillaries. The Au films were found to be highly SERS-active. In this section, first, PEI-capped Au nanoparticles film is fabricated on the inside surface of a glass capillary, and 2,6-dimethylphenylisocyanide (2,6-DMPI) as a model molecule of organic isocyanide, is adsorbed onto the Au nanoparticles. Then,

it is examined how the surface charge (surface potential) of Au nanoparticles that had been capped with PEI is varied by the pH of the external solution. In fact, branched PEI is a basic polyelectrolyte comprised of primary, secondary, and tertiary amines in a 1:0.75:1 molar ratio, so that PEI molecules exhibit considerable buffer capacity over almost the entire pH range.[28-30] This is because the pH at which protonation takes place is believed to be a function of the pK_a values of three different amines.[30,31] Since the local environment for the three amino groups is different from each other, their pK_a values are different such that the pH is around 9 for primary, 8 for secondary, and 6 ~ 7 for tertiary amino groups.[32] As a result, the protonation profile of PEI increases rapidly, especially in the acidic region, making the molecule a virtual "proton sponge."[33] The electron donation capability of PEI alone to Au nanoparticles would then depend subtly on the pH of the medium. On the other hand, the interaction between oppositely charged (acidic and basic) polyelectrolytes is affected by the pH of the medium, as well as the concentration of the background electrolytes, since the effective charge of polyelectrolytes depends on the ionization of its polar groups, and this in turn rests on both the pH and the ionic strength of the medium.[34-37] Bearing this in mind, first, the SERS of 2,6-DMPI is measured by varying the solution pH after capping consecutively with PEI and PAA. Second, it is demonstrated that the surface potential of Au nanoparticles is varied by the LbL deposition of polyelectrolytes onto them.

2. Experimental

Chemicals. Hydrogen tetrachloroaurate ($HAuCl_4$, 99.99%), branched PEI (MW ~25 kDa), poly(acrylic acid) (PAA, MW ~450 kDa), benzenethiol (BT, 99+%), 2,6-dimethylphenylisocyanide (2,6-DMPI, 96%), sodium borohydride ($NaBH_4$, 99%), and 0.4-μm-sized carboxyl-terminated polystyrene (PS) beads were purchased from Aldrich and used as received. Nitric acid (HNO_3, 60%) and sodium hydroxide (NaOH, 97%) were purchased from Samchun and Daejung Chemical Co, respectively. Other chemicals unless specified were reagent grade, and aqueous solutions were prepared using highly purified water whose resistivity was greater than 18.0 MΩ·cm.

Preparation of PEI-Capped Au Nanoparticle Film. Details were described in the Experimental section of Chapter 2. Btriefly, 25 mL of 1.4 mM aqueous $HAuCl_4$ solution was first mixed with 0.7 mL of 1% (w/w) PEI, and then stirred vigorously at 80 ℃ for 2 h. The reacted mixture was ultracentrifuged and filtered, and then the precipitate was washed with copious amounts of deionized water. The PEI-capped Au nanoparticles obtained were re-dispersed in water (5 mL). Toluene (2 mL) was poured over the aqueous Au solution, and then BT (1.0 mL) was added into the toluene phase. A fairly homogeneous Au film formed at the toluene-water interface, and it was possible to transfer the film onto a silicon wafer immersed in the mixture. To deposit Au onto the inside of the capillary wall, the mixture was injected using a syringe through the capillary tube. The glass capillary had a 1.1 mm in inner diameter and was 0.2 mm thick and 75 mm long. BT was subsequently removed from Au for the adsorption of 2,6-DMPI.

Adsorption of 2,6-DMPI on PEI-Capped Au Nanoparticle Film. As described in Chapter 2, BT was desorbed from the PEI-capped Au nanoparticles, without disturbing the SERS activity of the Au film, by treatment with a 0.1 M borohydride solution.[38] Specifically, 0.1 M ethanolic borohydride solution was flowed through a BT-adsorbed capillary tube at a flow rate of 0.19 mL/min; more than 80% of BT was desorbed from the Au within 5 min. After the complete disappearance of the SERS peaks of BT, a 1.0 mM ethanolic solution of 2,6-DMPI

was flowed through the capillary, and the SERS peaks were saturated within 1 min.

LbL Deposition of Polyelectrolytes. For the LbL deposition of polyelectrolytes onto the PEI-capped Au film on a silicon wafer, the substrate was immersed in an aqueous solution of PAA (0.1 mg/mL) for 10 min at room temperature, and then washed with water. After drying using a nitrogen blow, the substrate was immersed in an aqueous solution of PEI (0.1 mg/mL) for 10 min, washed with water, and dried with nitrogen; the pH of the PEI solution was 7.5, while that of the PAA solution was 5. These processes were repeated to obtain a multilayered film on the gold-nanoparticles. Polyelectrolyte layers were also deposited onto Au-deposited PS beads. The beads were dipped sequentially into PAA and PEI solutions (0.1 mg/mL) for 10 min, and in the interim to change the polyelectrolyte solution, PS beads were intensively rinsed with water.

Instrumentation. The thickness of the PAA/PEI multilayers on a silicon wafer was estimated using a Rudolph Auto EL II optical ellipsometer. The measurement was performed with a 632.8 nm beam of He/Ne laser incident upon the sample at 70°. The ellipsometric parameters, Δ and ψ, were determined for both the bare clean substrates and the multilayered films. As usual, the refractive index of the polyelectrolyte film was assumed to be 1.45,[39] and at least three different sampling points were considered to get the averaged thickness value. The zeta (ζ) potential of polyelectrolyte-deposited PS beads was measured in water by using electrophoretic light scattering spectrophotometer (ELS-8000, OTSUKA Electronics Co. Ltd., Japan). The flow of solutions through a glass capillary tube was controlled using a Sage Instruments Model 341 syringe pump. UV/vis spectra were obtained with a SINCO S-4100 UV/vis absorption spectrometer. Transmission electron microscope (TEM) images were taken using a JEM-200CX transmission electron microscope at 200 kV. Raman spectra were obtained using a Renishaw Raman system Model 2000 spectrometer equipped with an integral microscope (Olympus BH2-UMA). The 632.8 nm radiation from a 17 mW He/Ne laser (Spectra Physics Model 127) was used as the excitation source and the power at the sampling position was ~0.17 mW. The Raman band of a silicon wafer at 520

cm-1 was used to calibrate the spectrometer. The spectral peak intensity was also normalized with respect to that of the silicon wafer at 520 cm^{-1}. For potential-dependent SERS measurements, Au wire was made SERS-active by repeated oxidation-reduction cycles (ORCs) in a 0.1 M KCl solution by cycling between -0.8 V and +1.0 V and then being immersed in a 1 mM ethanolic solution of 2,6-DMPI for 1 h. The modified Au wire and a pure Pt wire were used as working and counter electrodes, respectively, in a 0.1 M $NaClO_4$ solution.[40] The potential of the electrochemical cell used for Raman spectral measurements was controlled using a CH Instruments model 660A potentiostat, which employed CHI 660A electrochemical analyzer software (version 2.03) running on an IBM-compatible PC. All potentials are reported with respect to the saturated Ag/AgCl electrode.

Theoretical Calculations. In order to better interpret the interaction of PEI to Au theoretically, simple density functional theory (DFT) calculation have been separately performed. The binding energy of the primary, or secondary, or tertiary amine group of PEI with a single Au atom and the associated change in the net charge of Au atom were computed using a Gaussian 03W suite at the B3LYP level theory. The LanL2DZ basis sets were used for the Au atom while the STO-3G basis sets were used for the fragment of PEI.

3. Results & Discussion

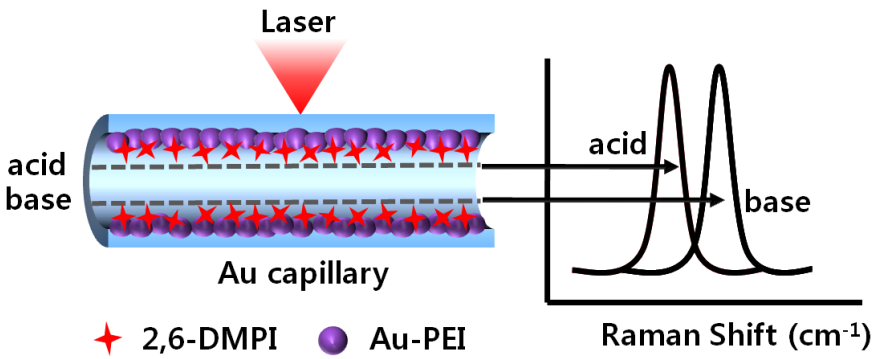

Scheme 1. The pH effect on the surface potential of polyelectrolytes-capped gold nanoparticles probed by SERS.

Normal Raman and SERS Spectra of 2,6-DMPI. Figure 1a shows the normal Raman (NR) spectrum of 2,6-DMPI in a neat solid state. Figure 1b shows the SERS spectrum of 2,6-DMPI adsorbed on an ORC-roughened Au wire. The general characteristics of the NR and SERS spectra of 2,6-DMPI were reported in the literature in the literature. In the NR spectrum, two intense peaks appear at 2123 and 640 cm^{-1}, which can be assigned to the NC stretching and the C−NC stretching vibration, respectively. Ring associated bands are comparatively less intense than the NC associated bands, as can be seen from the peaks at 3046, 1593, and 995 cm^{-1} in Figure 1a, which can be assigned to the CH stretching, the ring CC stretching (ν_{8a}), and the in-plane ring breathing (ν_{12}) modes of 2,6-DMPI, respectively. Substantial spectral differences exist between the NR and SERS spectra in Figures 1a and b. The most noticeable differences are associated with the NC stretching bond. The C−NC stretching band is weakened considerably and shifted by as much as 18 cm^{-1} upon adsorbing on Au. In addition, the NC stretching

peak is shifted from 2123 to 2174 cm^{-1}. The NC stretching peak has thus blue-shifted by as much as 51 cm^{-1} upon adsorbing on Au. The NC stretching band also broadened considerably, from 9 to 23 cm^{-1}, by the surface adsorption, whereas the ring-associated bands including ν_{8a} broadened only by 2 cm^{-1}. The substantial blue-shift of the NC stretching mode can be understood by invoking the fact that the carbon lone-pair electrons in the isocyanide group have antibonding character. The donation of these electrons to gold should increase the strength of the NC bond. The substantial band broadening is associated with the vibrational energy relaxation channel provided by the direct contact of the NC group with the metal substrate.[41-43]

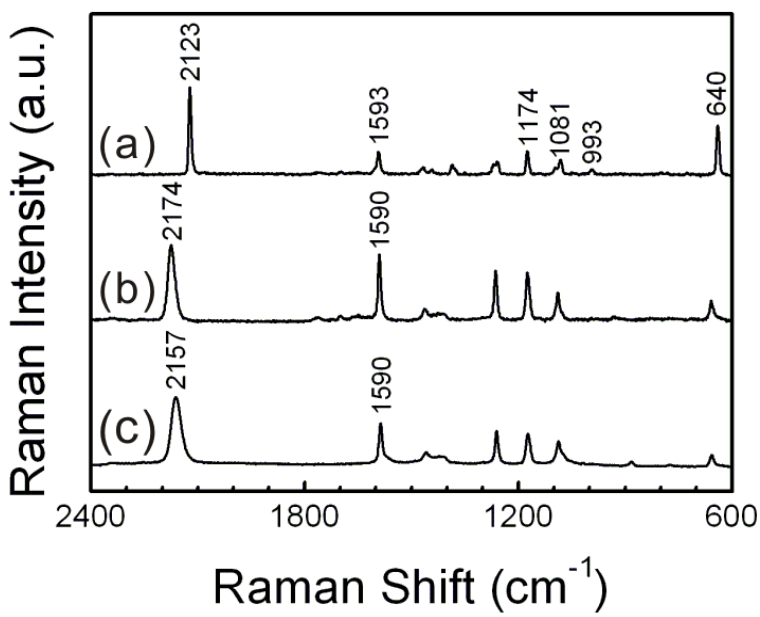

Figure 1. (a) Normal Raman spectrum of neat 2,6-DMPI. (b) SERS spectrum of 2,6-DMPI adsorbed on an ORC roughened Au wire electrode. (c) SERS spectrum of 2,6-DMPI adsorbed on PEI-capped Au nanoparticle film.

Figure 1c shows the SERS spectrum of 2,6-DMPI adsorbed on PEI-capped Au nanoparticles on glass. Its spectral pattern is barely different from that

in Figure 1b except that the NC stretching band appears at 2157 cm^{-1} in Figure 1c instead of at 2174 cm^{-1}, as observed in Figure 1b. The difference in the NC stretching frequency must be due to the presence of PEI. To see the effect of PEI theoretically, a quantum mechanical calculation has been carried out based on DFT.[44] One gold atom was bound to a small fragment of branched PEI, consisting of three primary, three secondary, and one tertiary amine groups, as shown in Figure 2a. When a gold atom was located near the primary amine groups (see Figure 2b), the binding energy (after the geometry optimization) was computed to be 215 kJ/mol. Furthermore, when a gold atom was located near the secondary and tertiary amine groups (see Figure 2c and 2d, respectively), the binding energies were calculated to be as large as 321 kJ/mol and 294 kJ/mol, respectively. For reference, when a gold atom was allowed to interact with an ammonia molecule, a similar calculation resulted in the binding energy of 205 kJ/mol. Although the present calculations are somewhat primitive, it clearly indicates that the interaction between PEI and gold is quite strong. The theoretical calculation suggested that the gold atom became negatively charged upon interacting with PEI. The net charge of the gold atom was computed to be -0.48e, -0.81e, and -0.72e when interacting with the primary, secondary, and tertiary amine groups of PEI, respectively, while it was -0.42e when interacting with an ammonia molecule. The lower NC stretching frequency of 2,6-DMPI by 17 cm^{-1} in Figure 1c versus Figure 1b would then be associated with the electron donation of PEI to gold. An increase in the net electronic charge of gold atoms can be thought to correspond to the lowering of the potential of gold in clusters. The NC stretching band of 2,6-DMPI on Au must shift in either direction in accordance with the surface potential of gold, which is subject to change by an external source or by the donation or withdrawal of PEI electrons to or from gold substrates.

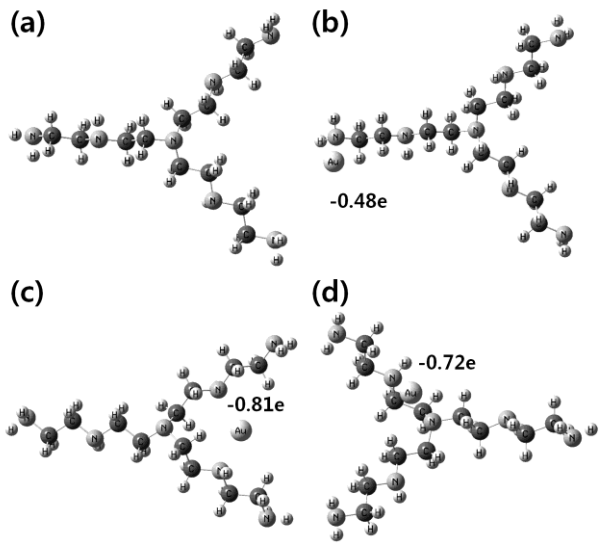

Figure 2. (a) A model fragment of PEI consisting of three primary, three secondary, and one tertiary amine groups. Schematics representing one gold atom interacting with (b) primary, (c) secondary, and (d) tertiary amine groups of PEI.

To see the effect of external potential on Au, a series of potential-dependent SERS spectra of 2,6-DMPI were taken using the same ORC-roughened Au wire electrode in Figure 1b.[45] As shown in Figure 3a, SERS spectra were reproducibly obtained in the potential region between +0.0 V and -0.6 V as compared to a saturated Ag/AgCl reference electrode in a 0.1 M $NaClO_4$ aqueous solution. The peak positions, as well as the bandwidths of the ring modes, were not subjected to change following the potential variation. In contrast with the ring modes, a noticeable peak shift is observed for the NC stretching band. The NC stretching peak is gradually blue-shifted following the increase in the surface potential. This can be understood by referring to the bonding scheme of 2,6-DMPI to Au. As the potential is made more positive, there is increased σ donation from the C atom to the metal, resulting in a greater shift of electron density from the N atom into the NC bond, and as a consequence, both the bond order and the vibrational frequency are increased. The opposite effect takes place when the potential is made more negative. In addition, the backdonation from metal to NC

π* orbitals can occur at negative potentials, decreasing the bond order and vibrational frequency. As a result of these effects, the NC stretching peaks are observed at 2176, 2168, 2162, and 2154 cm^{-1} at 0.0, -0.2, -0.4, and -0.6 V, respectively. As can be seen in Figure 4b, these values vary linearly with a slope of ~36 cm^{-1}/V. The NC stretching frequencies observed herein are all much higher than that of free isocyanide, as shown in Figure 1a. This suggests that even at negative potentials, back-bonding makes only a minor contribution to the spectral feature of 2,6-DMPI adsorbed on a Au electrode. According to the potential-dependent SERS in Figure 3a, the NC stretching frequencies of 2174 cm^{-1} and 2157 cm^{-1} in Figures 1b and 1c correspond, respectively, to the surface potential of Au at -0.04 V and -0.52 V versus a saturated Ag/AgCl reference electrode: the PEI has donated enough electrons to Au such that even in ambient conditions the Au nanoparticles should assume -0.52 V. The PEI has thus markedly decreased the surface potential of Au nanoparticles by as much as > 0.4 V upon contact.

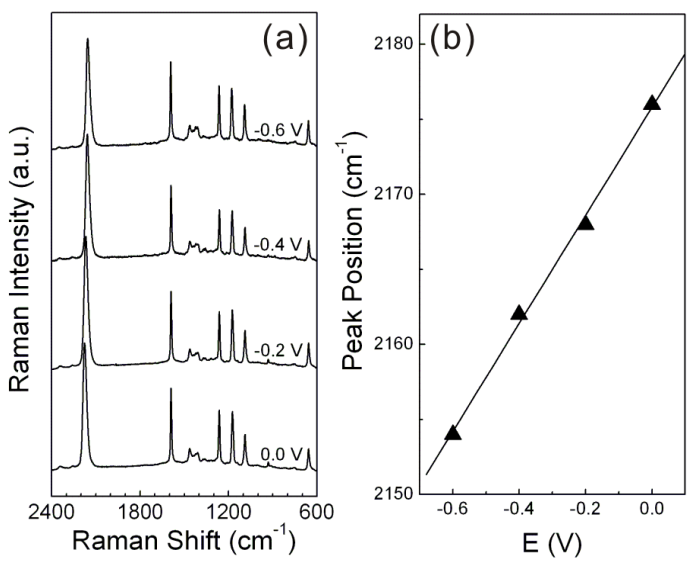

Figure 3. (a) Potential-dependent SERS spectrum of 2,6-DMPI on an ORC roughened Au wire electrode recorded at -0.6, -0.4, -0.2, 0.0 V versus an Ag/AgCl reference electrode in a 0.1 M $NaClO_4$ aqueous solution. (b) NC stretching frequency versus the electrode potential in (a).

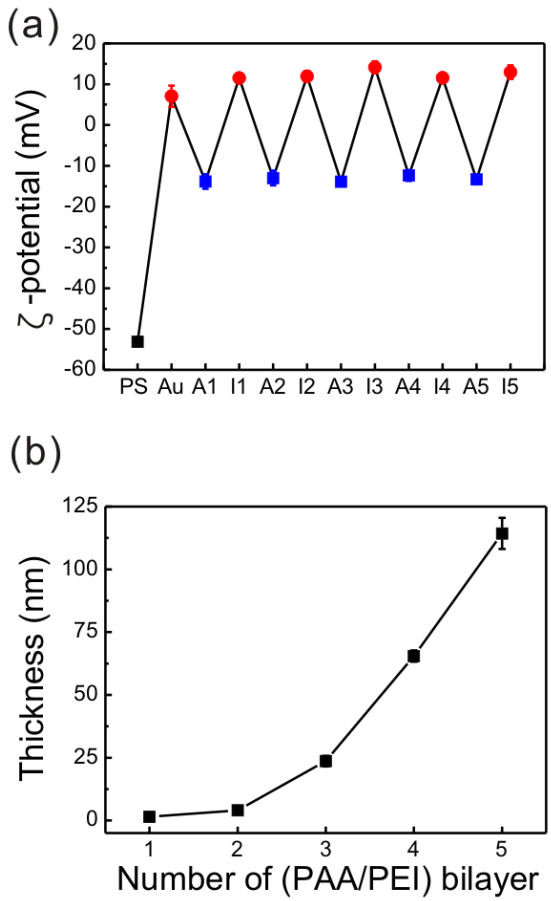

Figure 4. (a) Zeta (ζ)-potential of polystyrene (PS) beads measured after the deposition of PEI-capped Au nanoparticles first (Au) and then after consecutive deposition of PAA (squares) and PEI (circles) thereon. (b) Ellipsometric thickness measured as a function of (PAA/PEI) bilayer deposited on PEI-capped Au-nanoparticles film.

Zeta Potential and Ellipsometry Measurements. Prior to examining the effect of polyelectrolytes onto the surface potential of Au nanoparticles, two control experiments (zeta potential and ellipsometry measurements) were perforemed to make sure that PAA and PEI can be deposited consecutively onto the PEI-capped Au nanoparticles film. At first, the zeta potential of unmodified PS

beads was measured to be negatively charged, i.e. -53.1 ± 0.9 mV, probably due to the deprotonation of the surface carboxyl groups. When the beads are coated with PEI-capped Au nanoparticles, the zeta potential becomes positive up to about +7.06 ± 2.6 mV. The zeta potential then alternates between negative (up to -13 mV) and positive (up to +13 mV) values, corresponding to the alternate adsorption of PAA (squares in Figure 4a) and PEI (circles in Figure 4a), respectively. As can be seen in Figure 4a, the alternation is more pronounced as the number of (PAA/PEI) bilayers increases. On the other hand, Figure 4b shows the ellipsometric thickness measured as a function of the (PAA/PEI) bilayer assembled on a PEI-capped Au-nanoparticles film on a silicon wafer; a bilayer refers to the deposition of a pair of negative and positive polyelectrolyte layers. The amount of (PAA/PEI) deposited initially onto the Au-nanoparticles film is not significant, but after two deposition cycles the ellipsometric thickness increases linearly with a growth rate of ~46 nm per bilayer. Accordingly, when five bilayers of (PAA/PEI) are deposited onto the film, the outermost PEI is located approximately 113 nm from the inner Au nanoparticles. Both the zeta potential and ellipsometry thickness measurements clearly demonstrate that PAA and PEI are successfully deposited onto the PEI-capped Au-nanoparticles film.

Effect of pH on SERS of 2,6-DMPI on PEI-Capped Au. SERS spectra of 2,6-DMPI adsorbed on PEI-capped Au nanoparticles were measured under the flow of acidic or basic solutions. Scheme 1 shows the schematic of the in-situ capillary Raman spectral measurement system. Specifically, Figures 5a and b show the SERS spectra measured under the flow of 0.1 M HNO_3 and 0.1 M NaOH solutions, respectively. The two SERS spectra are barely different from each other except that the NC stretching band appears at 2168 cm^{-1} in Figure 5a and at 2158 cm^{-1} in Figure 5b. The difference in the NC stretching frequency must be associated with the different pH values in the two solutions, i.e., pH 1 for 0.1 M HNO_3 and pH 13 for 0.1 M NaOH. The pH effect is not direct, but is mediated through PEI. This is evident because the SERS spectral pattern of 2,6-DMPI, including its NC stretching band, is not influenced by pH variation when pure gold

is used as the SERS substrate (data not shown). Consulting the potential-dependent SERS spectral data in Figure 4, the PEI-capped Au nanoparticles in Figures 5a and b can be regarded to assume -0.21 V and -0.49 V, respectively, versus a saturated Ag/AgCl reference electrode. It is presumed that the extent of protonation/deprotonation of PEI was determined by the pH, which in turn affected the surface potential of the Au nanoparticles that were in contact with PEI, leading to the different NC stretching frequencies observed in Figures 5a and b.

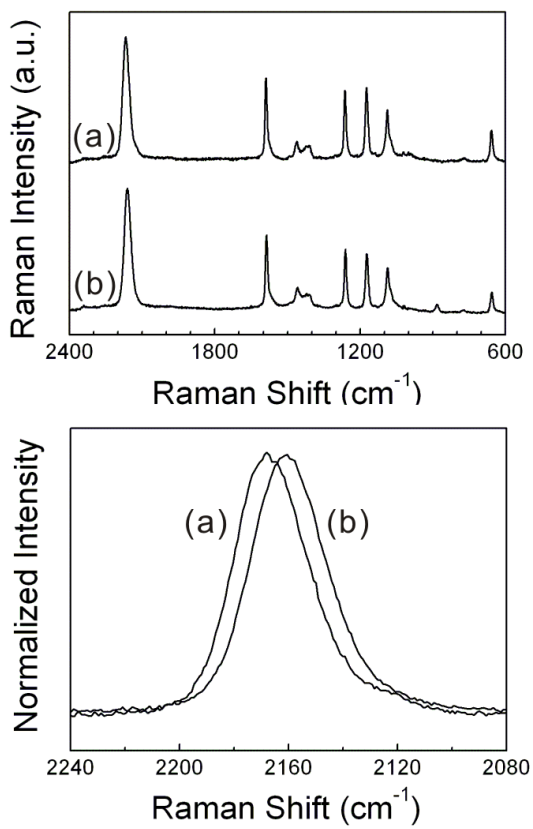

Figure 5. SERS spectra (upper panel) and NC stretching region (lower panel) of 2,6-DMPI on PEI-capped Au nanoparticles measured under the flow of (a) 0.1 M HNO_3 and (b) 0.1 M NaOH.

The protonation/deprotonation characteristics of PEI is determined by its pKa value. Accordingly, it was attempted, on one hand, to record the titration curve and, on the other hand, to measure the NC stretching frequency of 2,6-DMPI on PEI-capped Au nanoparticles as a function of solution pH. Figure 6a shows a typical acid/base titration curve of PEI, measured, after dissolving 1.2 mg of PEI in 30 mL of H_2O to give a final concentration of 0.4 mg/mL, by titrating with 0.1 N HNO_3 at 1M NaCl solution. It is well known that the titration of aqueous PEI with an aqueous acid solution, such as nitric acid, gives titration curves with no break suitable for determination of the end point.[46,47] This is due to the buffer capacity of PEI associated with the different pK_a values of primary (around 9), secondary (around 8), and tertiary amines (around 6-7) on the PEI backbone. In any case, Figure 6b shows the NC stretching frequencies of 2,6-DMPI on PEI-capped Au measured as a function of pH. The NC stretching frequency increases slightly from 2158 cm^{-1} to 2162 cm^{-1} as the solution pH decreases from 12 to 9, and then increases very abruptly from 2162 cm^{-1} to 2168 cm^{-1} as the solution pH decreases from 9 to 8. Thereafter, the NC stretching frequency increases very slightly from 2168 cm^{-1} to 2169 cm^{-1} as the solution pH decreases from 8 to 4. The pH region in which a dramatic frequency change takes place is around 8.5, which is close to the pK_a of the primary amine of PEI. This indicates that protonation and deprotonation occurs very dramatically around the pH value near the pK_a of the primary amine: among all forms of amine groups in PEI, approximately 50% of amine groups are presumably protonated at pH 8.5. The dramatic variation of the NC stretching frequency at pHs around the pK_a of the primary amine would then be associated with the strong buffer capacity of PEI.[28-30]

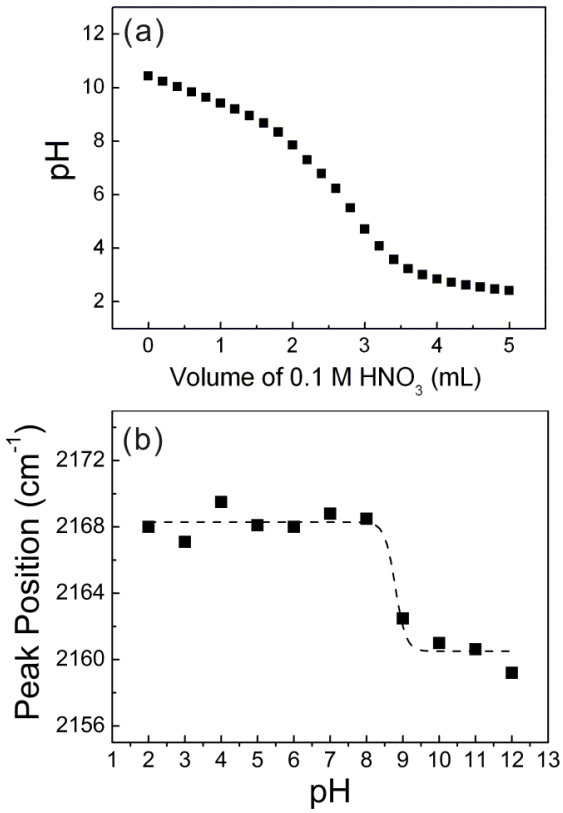

Figure 6. (a) Acid/base titration curve of PEI (0.4 mg/mL) measured by adding 0.1 N HNO_3 at 1M NaCl solution. (b) NC stretching frequency of 2,6-DMPI on PEI-capped Au nanoparticle film measured as a function of solution pH in contact with the film.

Subsequently, it was examined how the NC stretching band of 2,6-DMPI changes by varying the pH when an anionic polyelectrolyte such as PAA is deposited onto the PEI on Au. When PAA was deposited over the PEI-capped Au nanoparticles on a silicon wafer, the NC stretching band of 2,6-DMPI blue-shifted from 2157 to 2164 cm^{-1} in ambient conditions.[26] Consulting the potential-dependent SERS data in Figure 4b, this corresponds to a potential change from -0.52 V to -0.32 V versus a saturated Ag/AgCl reference electrode. Using the in-situ capillary Raman measurement system (Scheme 1), a series of SERS spectra of 2,6-DMPI

were then taken as a function of pH after the deposition of PAA onto PEI as shown in Figure 7a. Spectral variation is relatively small compared to that observed before the deposition of PAA. This is more evident from Figure 7b in which the NC stretching frequency versus the solution pH observed in Figure 7a is plotted. On one hand, the abrupt frequency change takes place around pH 6.5 instead of pH 8.5 and, on the other hand, the amount of frequency change is about three fourth of that observed in Figure 6b, i.e., 7.5 cm^{-1} in Figure 7b as compared to 10 cm^{-1}, as shown in Figure 6b. The pK_a value of PAA is known to be approximately 4.3.[48] The pH 6.5 at which the abrupt change of the NC stretching frequency occurs is close to the average pK_a value of the primary amine PEI (~9) and the PAA (~4.3). This can be explained by invoking the electrostatic neutralization of PEI by PAA, thus decreasing the electron donation capability of PEI to Au nanoparticles. Hence, the surface potential of Au nanoparticles is affected by PAA, indirectly via the mediation of PEI.

In order to gain further insight into the influence of the upper polyelectrolyte, SERS spectra of 2,6-DMPI were taken after the deposition of new PEI onto the PAA layer. As a new PEI is deposited onto PAA, the electron donating capability of the bottom PEI to Au increases such that the NC stretching peak of 2,6-DMPI red-shifts from 2164 to 2159 cm^{-1} in ambient conditions.[26] A series of SERS spectra of 2,6-DMPI were also taken at various pHs, even after the deposition of PEI onto PAA layer, as shown in Figure 8a. Spectral variation in Figure 8a is comparatively smaller than that in Figure 7a. This is more evident from Figure 8b in which the NC stretching frequency versus the solution pH observed in Figure 8a is plotted. The abrupt frequency change takes place around pH 8.5 in Figure 8b instead of pH 6.5, as shown in Figure 7b. The amount of frequency change in Figure 8b is about one half of that in Figure 7b, i.e., 4 cm^{-1} in Figure 8b vs. 7.5 cm^{-1} in Figure 7b. It appears that the surface potential of Au nanoparticles is affected more by the bottom PEI (in contact with Au) than the upper PAA and PEI. This is probably due to stronger interaction of the upper two polyelectrolyte layers.

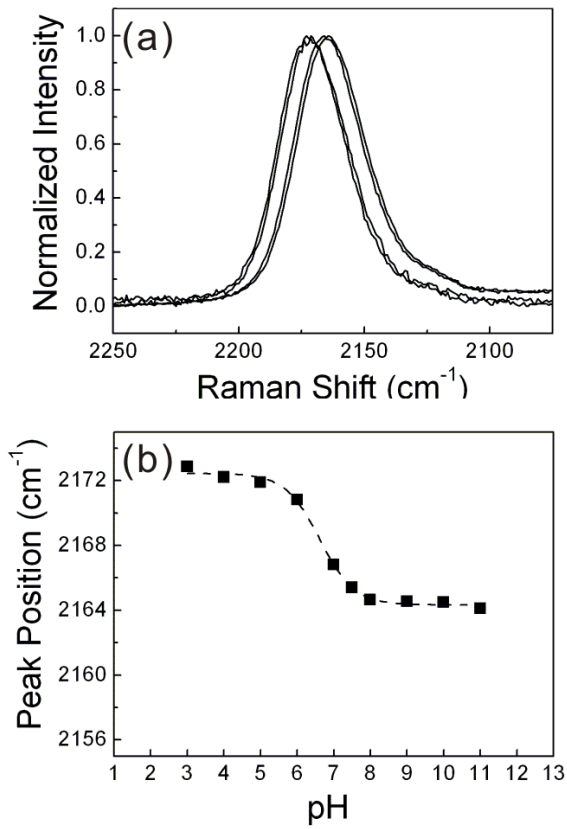

Figure 7. (a) NC stretching region of 2,6-DMPI on PAA/PEI-derivatized Au nanoparticles measured at various pHs (pH 4, 5, 7.5, and 8, respectively, from left to right) and (b) the NC stretching frequency drawn versus the solution pH.

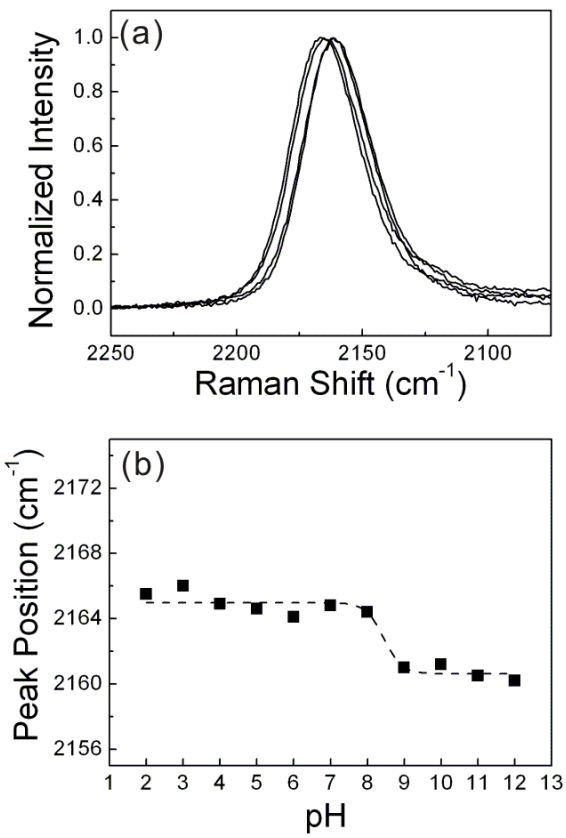

Figure 8. (a) NC stretching region of 2,6-DMPI on PEI/PAA/PEI-derivatized Au nanoparticles measured at various pHs (pH 2, 8, 9, and 10, respectively, from left to right) and (b) the NC stretching frequency drawn versus the solution pH.

Effect of in situ LbL Deposition of Polyelectrolytes on SERS of 2,6-DMPI on PEI-capped Au. Subsequently, it was attempted to take SERS spectra under the flow of PAA solution through a glass capillary coated previously with a 2,6-DMPI-adsorbed, PEI-capped Au nanoparticles film. It turns out that any spectral change occurred immediately and became stabilized shortly after the contact with PAA solution. This implies that the electrostatic interaction of PAA with PEI is very strong. The ring modes of 2,6-DMPI were invariant, but the NC

stretching band was subjected to change in response to the flow of PAA solution. That is, the NC stretching band of 2,6-DMPI has shifted from 2157 to 2164 cm^{-1} by the interaction of PEI with PAA. Subsequently an aqueous PEI solution was allowed to flow through the glass capillary, and found that the NC stretching band shifts immediately from 2164 to 2158 cm^{-1} without altering the ring modes. For reference, the NC stretching region is shown in Figure 9a for the two spectra taken under the flow of PAA and then PEI. Figure 9b shows the variation of the NC stretching frequency of 2,6-DMPI drawn as a function of deposition of PAA (squares) and PEI (circles) layers onto the capillary film. The NC stretching frequency alternates with the deposition of anionic and cationic polyelectrolytes, but the amount of peak shift gradually diminishes along with the increase in the deposition cycles. More specifically, the effect of the outermost polyelectrolytes onto the core Au nanoparticles is weakened gradually as the deposition cycle is increased. Obviously, this is in contrast with the zeta potentials shown in Figure 4a. The zeta potential is governed directly by the outermost polyelectrolytes irrespective of the number of bilayers deposited, but the outermost layer is revealed to hardly affect the core Au nanoparticles when the layer is distant about >160 nm from the core.

As described above, when PAA was passed over the PEI-capped Au nanoparticles film, the NC stretching band of 2,6-DMPI was blue-shifted from 2157 to 2164 cm^{-1}. Consulting the potential-dependent SERS data in Figure 3b, this corresponds to a potential change from -0.52 V to -0.32 V vs a saturated Ag/AgCl reference electrode. One may argue that the NC stretching band should have red-shifted, instead of showing a blue-shift, when negatively charged PAA were in contact with the film. This can be reconciled with the notion that the bottom PEI has donated enough electrons to Au such that even in ambient conditions the Au nanoparticles should assume -0.52 V vs a saturated Ag/AgCl reference electrode. As PAA is deposited onto PEI, the electron donating capability of PEI to Au must decrease, resulting in the increase in the surface potential of Au nanoparticles. As a new PEI is deposited onto PAA, the electron donating capability of the bottom PEI

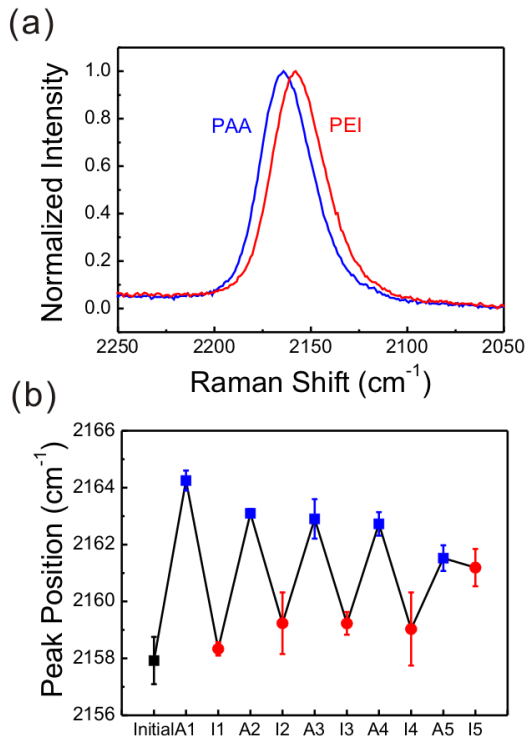

Figure 9. (a) NC stretching region measured under the flow of PAA and then PEI through a glass capillary coated previously with a 2,6-DMPI-adsorbed, PEI-capped Au nanoparticle film. (b) NC stretching frequency of 2,6-DMPI drawn as a function of the deposition of PAA (squares) and PEI (circles) layers onto the 2,6-DMPI-adsorbed, PEI-capped Au nanoparticle film.

to Au will now increase, resulting in the decrease in the surface potential of Au nanoparticles, as observed by means of NC stretching peaks. The bottom PEI is gradually less affected by the LbL deposition of polyelectrolytes, and in this specific example, the surface potential of Au nanoparticles is finally stabilized around -0.41 V since the NC stretching frequency has attained a plateau value around 2161 cm^{-1}, as can be seen in Figure 9b. Although not shown here, the relative peak intensities of the ring modes were invariant. This would suggest that the orientation of 2,6-DMPI on PEI-capped Au nanoparticles film is also not subjected to change by the LbL deposition of PAA and PEI.

4. Summary and Conclusions

Nanoparticles are commonly stabilized through the adsorption of acidic/basic polyelectrolytes around the surface of the particle. One example of these nanoparticles is PEI-capped Au nanoparticles. In this work, it was examined how much the surface potential of Au nanoparticles is affected by the solution pH through the mediation of the protonation and deprotonation of PEI in contact with Au nanoparticles using SERS of 2,6-DMPI. In fact, the surface-potential-dependent NC stretching peak of 2,6-DMPI has shifted sharply around pH 8.5, close to the pKa value of the primary amine of PEI. When a negatively charged PAA was deposited onto the PEI, the peak shift of the NC stretching band took place around pH 6.5, close to the average pKa value of PEI and PAA. When additional PEI was deposited on PAA, the peak shift of the NC stretching band occurred once again around pH 8.5, indicative of the stronger interaction of upper two polyelectrolyte layers. The surface potential of Au nanoparticles alternated upon the further LbL deposition of PEI and PAA, but the extent of variation gradually diminished. The surface potential of Au nanoparticles finally attained a plateau value, that is, -0.41 V, after the deposition of five bilayers as thick as 113 nm. In contrast to the surface potential of Au nanoparticles, the zeta potential was confirmed to vary alternately irrespective of the number of LbL depositions, indicating that it must be determined solely by the outermost polyelectrolyte layer. This work is unique in that SERS is proven to be useful in assessing even a minute surface potential change of noble metal nanoparticles brought about by polyelectrolytes.

3.2. 2,6-DMPI-Adsorbed Gold Nanostructure: A SERS Sensory Device to Detect Volatile Organic Compounds (VOCs)

1. Introduction

Volatile organic compounds (VOCs) are numerous, varied, and ubiquitous. A major source of manmade VOCs is solvents, especially paints and protective coatings.[49,50] Allergic, respiratory, or immune effects in infants or children are largely associated with these man-made VOCs. The ability of VOCs to affect health varies greatly from those that are highly toxic, to those with no known health effect.[51,52] At present, not much is known about what health effects occur from the levels of organics usually found in homes, although many VOCs are known to cause cancer in animals.[53] As with other pollutants, the extent and nature of the health effect will depend on many factors including level of exposure and length of time exposed. In nature, most VOCs arise from plants, as exemplified by the strong odor emitted by many plants.[54,55] The biogenic VOCs include the isoprenoids (or terpenoids) such as isoprene and monoterpenes, as well as alkanes, alkenes, carbonyls, alcohols, esters, and acids.[56] Recently, isoprene (C_5H_8), monoterpenes ($C_{10}H_{16}$), and sesquiterpenes ($C_{15}H_{24}$) have received a great attention since these VOCs can produce tropospheric ozone (O_3) in the presence of nitrogen oxide.[57-60]

The early detection of VOCs is a challenging task. In principle, VOCs in the environment or certain atmospheres can be detected based on the specific interactions between the organic compounds and the sensor components.[61] There are a lot of VOC sensing materials, including metal oxide, conducting polymers, carbon nanotubes, carbon-polymer composites and functionalized gold nanoparticles to detect a wide range of VOCs.[62-67] In fact, metal oxide materials such as SnO_2 and ZnO and conducting polymers have been used in commercial sensors to detect even ppm concentrations despite the nonselectivity. However, so

far, the VOC sensing devices using vibrational spectroscopy such as Raman scattering have been rarely developed. Very recently, Fan and coworkers reported a direct detection of 2,4-dinitrotoluene vapor using photo-chemically synthesized Au nanoparticles as the SERS substrate.[73] It was possible due to the high affinity of 2,4-dinitrotoluene vapor towards Au nanoparticles. However, to detect other VOCs similarly via SERS, but whose adsorption strength to Au or Ag might be very weak, it would be mandatory to cool down the SERS substrate.[74]

As described in section 3.1, the peak position of the NC stretching band of 2,6-DMPI on Au is very sensitive to the electrode potential. We demonstrate in this section that the NC stretching band is susceptible even to the exposure of VOCs. Specifically, The SERS of 2,6-DMPI on PEI-capped Au nanoparticles are affected greatly not only by usual VOCs such as CCl_4, methanol, ammonia, and butylamine but also by biogenic VOCs such as isoprene, farnesol, and (+)-α-pinene. To our knowledge, this is the first report, informing the applicability of SERS, though indirect, in the detection of biogenic VOCs.

2. Experimental

Chemicals. Hydrogen tetrachloroaurate ($HAuCl_4$, 99.99%), branched poly(ethylenimine) (PEI, MW~25 kDa), benzenethiol (BT, 99+%), 2,6-DMPI (96%), sodium borohydride ($NaBH_4$, 99%), butylamine (BA, 99.5%), isoprene (99.5+%), farnesol (95%), and (+)-α-pinene (98.5+%) were purchased from Aldrich and used as received. Ammonia solution (NH_3, 28.0~30%) and methyl alcohol (MeOH, 99.5%) were purchased from Samchun Chemical Co. Carbon tetrachloride (CCl_4, 99%) was purchased from Janssen Chimica Co. Other chemicals, unless specified, were reagent grade, and aqueous solutions were prepared using highly purified water whose resistivity was greater than 18.0 M· cm.

VOCs. For a concentration dependency study, 1 L volumetric flask was first flushed with N_2, maintaining an atmospheric pressure, and then capped with a rubber septum. Using a syringe, a measured quantity of VOCs was introduced through the rubber septum into the volumetric flask and allowed them to fully evaporate. About 50 mL of the mixed organic gas was suck out using a syringe, which was subsequently set to flow through a glass capillary coated with Au.

Instrumentation. The flow of VOCs through a glass capillary tube was controlled using a Sage Instruments Model 341 syringe pump. The 632.8 nm radiation from a 17 mW He/Ne laser (Spectra Physics Model 127) was used as the excitation source for Raman spectrial measurement. For potential-dependent SERS measurements, an Au wire was made SERS-active by repeated oxidation-reduction cycles (ORCs) in a 0.1 M KCl solution by cycling between -0.8 and +1.0 V, and then it was immersed in a 1 mM ethanolic solution of 2,6-DMPI for 3 h.[40] The Au wire modified in this way and a pure Pt wire were used as working and counter electrodes, respectively, in a 0.1 M $NaClO_4$ solution. The potential of the electrochemical cell was controlled using a CH Instruments model 660A potentiostat, which employed CHI 660A electrochemical analyzer software (version 2.03). All potentials are reported with respect to the saturated Ag/AgCl electrode. A quartz crystal microbalance (QCM) experiment was conducted using an Au-coated, AT-cut quartz crystal (fundamental resonance frequency, f_o = 10

MHz): VOCs of a known concentration were passed through the cell, monitoring the frequency change as a function of time.[75]

3. Results & Discussion

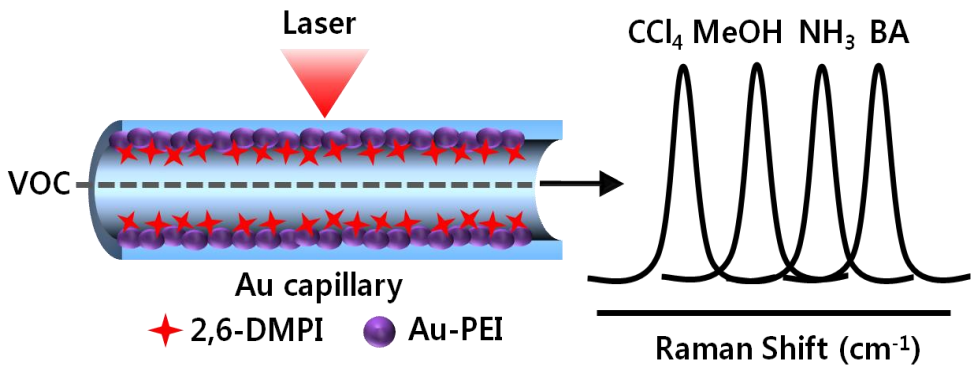

Scheme 2. Schematic representation of 2,6-DMPI-adsorbed gold nanostructure: a SERS sensory device for detection of volatile organic compounds.

Effect of VOCs on SERS of 2,6-DMPI on PEI-capped Au. As mentioned in the Experimental Section, VOCs of different concentration were prepared by allowing a measured liquid aliquot to evaporate in a 1 L vessel filled with atmospheric N_2, and their flow rate through a glass capillary containing PEI-capped Au nanoparticles was controlled using a syringe pump: hereafter, the concentration of VOCs will be denoted simply by their partial pressure since the carrier gas is mostly atmospheric nitrogen. Scheme 2 shows the schematic of 2,6-DMPI-adsorbed gold nanostructure to detect VOCs.

First, it was confirmed that the SERS spectral pattern of 2,6-DMPI was affected by the concentration of VOCs, but not by the flow rate of VOCs at least in the range of 0.3 – 13 mL/min. The flow rate of VOCs was thus set to be 8 mL/min in all subsequent experiments. Figure 10a shows a series of time dependent SERS spectra of 2,6-DMPI measured under a flow of CCl_4 vapor at a partial pressure of 12.8 kPa. The ring associated bands were neither shifted nor broadened by

exposure to CCl_4. In contrast, the NC stretching band was noticeably blue-shifted upon contact with CCl_4. This is evident from Figure 10b which shows the variation of the NC stretching peak position, drawn versus time, in Figure 10a. The NC stretching band blue-shifted from 2157 to 2177 cm^{-1} within 30 s, and it remained there without further variation. Consulting the potential-dependent SERS data in Figure 3b in section 3.1, this corresponds to a potential change from -0.52 to 0.037 V.

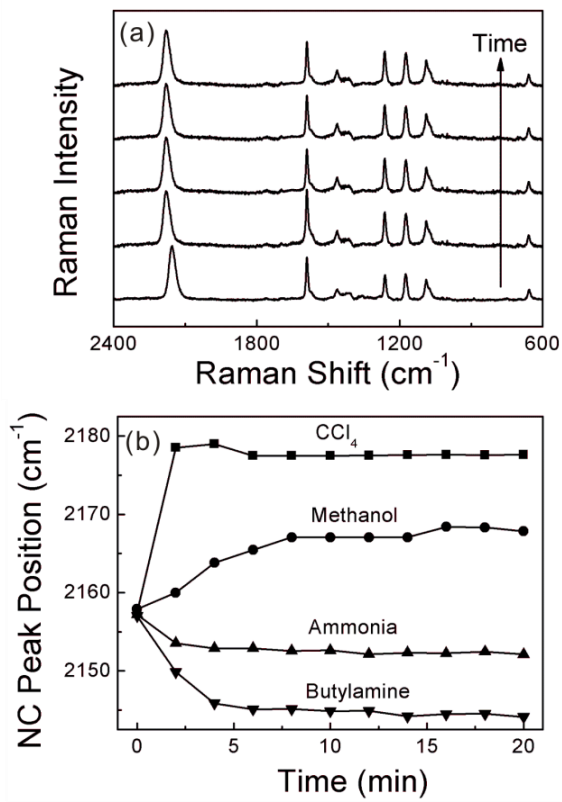

Figure 10. (a) A series of time-dependent SERS spectra of 2,6-DMPI measured under a flow of CCl_4 at a partial pressure of 12.8 kPa: from bottom to top measured after 0, 2, 6, 10, and 14 min of flow, respectively. (b) Time variation of the NC stretching peak position under flows of CCl_4, methanol, ammonia, and butylamine, at a partial pressure of 12.8 kPa.

The ring associated bands of 2,6-DMPI were invariant also when other VOCs like ammonia, methanol, and butylamine were passed over the 2,6-DMPI-adsorbed PEI-capped Au nanoparticle film. The NC stretching band had, however, red-shifted under the flow of ammonia and butylamine, while it blue-shifted under the flow of methanol. The time-variation of the peak position measured under the flow of these VOCs at 12.8 kPa is also shown in Figure 10b. The NC stretching band was up- or downshifted, and then reached a plateau level within 30 s. The amounts of red-shift under the flow of ammonia and butylamine were 7 and 12 cm^{-1}, respectively, while the amount of blue-shift under the flow of methanol was 10 cm^{-1}. As for CCl_4, the blue-shift by methanol is indicative of the charge transfer from gold to methanol. On the other hand, the red-shift by ammonia and butylamine indicates the donation of lone-pair electrons of the nitrogen atoms in ammonia and butylamine to Au. A subtle difference in the interaction of VOCs with Au must be responsible for the measured difference in the peak shift of the NC stretching band.

Concentration Dependency of Usual VOCs. When VOCs at lower partial pressures were passed over the 2,6-DMPI adsorbed PEI-capped Au nanoparticle film, it took as much as 4 min for the peak position of the NC stretching band to reach a plateau level. The amount of peak shift at the plateau level was also dependent on the concentration of VOCs. Among different VOCs, the concentration dependencies were different, but their behaviors were qualitatively similar to one another. We therefore made a focus specifically on the concentration dependencies of carbon tetrachloride and butylamine. Figure 11a shows the time-variation of the NC stretching peak position measured under the flow of CCl_4 vapors at partial pressures of 12.8, 2.56, 1.28, and 0.64 kPa. It is evident that at least 3 - 5 min is required for a steady state to be established at partial pressures lower than 12.8 kPa. The amount of NC peak shift at 0.64 - 2.56 kPa is, however, at best 2 - 3 cm^{-1} lower than that at 12.8 kPa. This may indicate that the PEI-capped Au nanoparticles were covered with CCl_4 to near saturation at a partial pressure above 0.64 kPa (vide infra). The amounts of blue-shift (at

plateaus) relative to that measured at 12.8 kPa are plotted in Figure 11b as a function of the concentration of CCl_4. The smaller peak shift at lower partial pressures must be associated with the lower surface coverage of CCl_4 in that condition. It is remarkable that even a blue-shift of 1 cm^{-1} was reproducibly measured at a partial pressure of 125 mPa. The partial pressure of 125 mPa corresponds to 6.5 ppm.

A QCM study was conducted to see how much CCl_4 could adsorb on an Au surface. CCl_4 vapor was allowed to flow over a 10 MHz Au electrode; according to the Sauerbrey equation,[76] the measured frequency change (Δf) can be associated with the mass of CCl_4 adsorbed on Au (Δm) as follows: $\Delta m = -0.884\Delta f$ ng/Hz. Surprisingly, no meaningful frequency change was measurable at a partial pressure of CCl_4 as low as 12.8 kPa. This suggests that the observation of the NC stretching peak shift is far more sensitive to the gravimetric method, QCM. In any case, at 23 kPa the frequency decrease was measured to be 8.6 Hz, which corresponds to the adsorption of 7.59 ng of CCl_4 on Au. Since the active area of Au in the QCM apparatus was 0.20 cm^2, each CCl_4 molecule would then be presumed to occupy an area of 0.68 nm^2. The present QCM experiment dictates that smaller amounts of CCl_4 should adsorb on Au at 0.64 kPa than at 12.8 kPa and of course than at 23 kPa. How then can we rationalize the observation that the amount of blue-shift of the NC stretching band at 0.64 kPa is as much as 85% of that measured at 12.8 kPa? It is tentatively assumed that the amount of electronic charge transferable from Au to CCl_4 was quite limited so that were not substantially more electrons able to transfer, even though more CCl_4 might have been adsorbed on Au at 12.8 kPa than at 0.64 kPa (vide supra). However, when the partial pressure of CCl_4 was lower than 0.64 kPa, a smaller number of electrons were actually transferred from Au to CCl_4, thereby the amount of blue-shift was decreased.

In order to gain further insight into the interaction of CCl_4 with Au, it was attempted to fit the data in Figure 11b to the Langmuir adsorption isotherm.[77] Letting $\Delta\tilde{\nu}$ be the NC stretching peak shift measured at the plateau level,

$\Delta\tilde{\nu}_{max}$be its maximum value measured at 12.8 kPa, K_{ads} be the adsorption constant of CCl_4 onto Au, and [CCl_4] be the concentration of CCl_4 in kPa, the following equation may hold:

$$\frac{\Delta\tilde{\nu}}{\Delta\tilde{\nu}_{max}} = \frac{K_{ads}[CCl_4]}{1 + K_{ads}[CCl_4]}$$

$$\frac{[CCl_4]}{\Delta\tilde{\nu}} = \frac{[CCl_4]}{\Delta\tilde{\nu}_{max}} + \frac{1}{K_{ads}\Delta\tilde{\nu}_{max}}$$

Figure 11c shows a plot drawn for $[CCl_4]/\Delta\tilde{\nu}$ versus [CCl_4]. The plot exhibits a linear relationship between the two values, implying that the Langmuir adsorption isotherm is applicable to the present system. From the slope and intercept, K_{ads} is calculated to be 13.6 kPa^{-1}. By using this K_{ads}, a theoretical Langmuir isotherm is drawn in Figure 11b. As expected, the theoretical Langmuir isotherm fits very well with the experimental results. It should be pointed out that the present K_{ads} is determined on the basis of the peak shift associated with the charge transfer between CCl_4 and Au. The value may not necessarily be the same as that determined based on the gravimetric method. As described above, QCM is not so sensitive to detect the sub-monolayer coverage of VOCs on Au.

As described earlier, the effect of butylamine was opposite to that of carbon tetrachloride. The NC stretching peak of 2,6-DMPI was red-shifted by as much as 12 cm^{-1}. A concentration dependency study was conducted in a similar way to CCl_4, and the amounts of red-shift (at plateaus) were determined at partial pressures ranging from 5 Pa to 26 kPa. Although not shown here, the plot of the amounts of red-shift, determined relative to that measured at 26 kPa, drawn versus the concentration of BA exhibited a linear relationship, implying that the Langmuir adsorption isotherm is applicable to the adsorption of BA onto Au. From the slope and intercept, the value of K_{ads} was calculated to be 1.73 kPa^{-1}. By using this K_{ads}, a theoretical Langmuir isotherm could be predicted which fitted well with the experimental results. The K_{ads} value for butylamine was about one fourth of that determined for carbon tetrachloride, however. This might indicate that the electron acceptor ability of carbon tetrachloride is more effective than the electron donor ability of butylamine when interacting with Au.

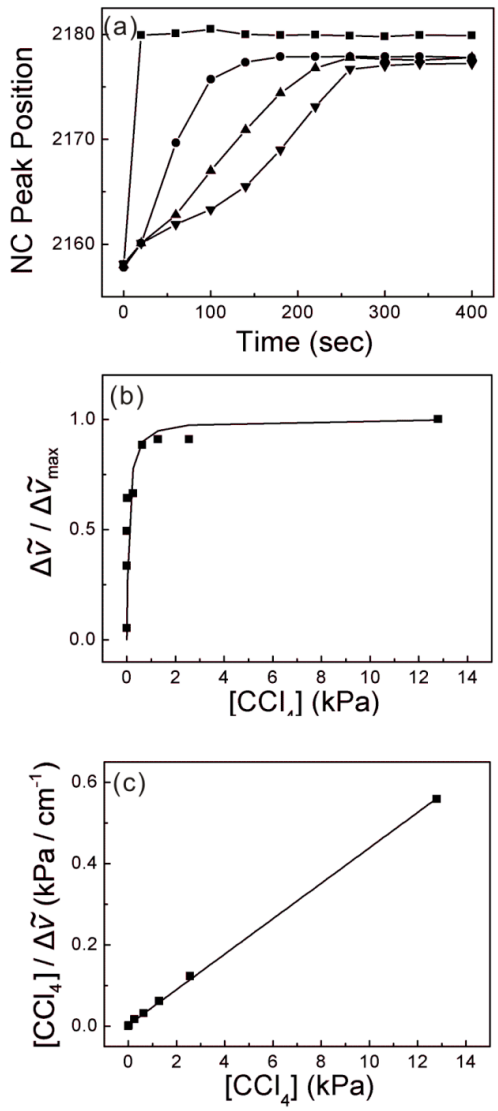

Figure 11. (a) Time variation of the NC stretching peak position of 2,6-DMPI measured under a flow of CCl_4 at a partial pressure of 0.64, 1.28, 2.56 or 12.8 kPa. (b) Amount of blue-shift of the NC stretching band (at plateaus) relative to that at 12.8 kPa drawn versus the concentration of CCl_4 passed over 2,6-DMPI-adsorbed PEI-capped Au nanoparticle film: the solid line is a calculated Langmuir adsorption isotherm. (c) A plot of $[CCl_4]/\Delta\tilde{\nu}$ drawn versus $[CCl_4]$ in which $\Delta\tilde{\nu}$ is the NC stretching peak shift measured at the plateau level in (b) and $[CCl_4]$ is the partial pressure of CCl_4 in units of kPa.

Effect of Biogenic VOCs on SERS of 2,6-DMPI on PEI-capped Au. SERS spectra of 2,6-DMPI were also taken under the flow of biogenic VOCs, *i.e.* isoprene, (+)-α-pinene (monoterpenes), and farnesol (sesquiterpenes). Figure 12a shows a series of time-dependent SERS spectra of 2,6-DMPI measured under the flow of (+)-α-pinene at a partial pressure of 15.6 kPa. The spectral pattern of 2,6-DMPI is invariant except for the NC stretching band. The NC stretching band was noticeably red-shifted by exposure to (+)-α-pinene. As collectively shown in Figure 12b, the NC stretching band has red-shifted from 2157 to 2150 cm^{-1} within 5 min. Consulting the potential-dependent SERS data in Figure 3b of section 3.1., this corresponds to a potential change from -0.52 to -0.72 V.

When the 2,6-DMPI-adsorbed Au film was exposed to isoprene, the NC stretching band was red-shifted, similarly to the case of (+)-α-pinene, but the band was blue-shifted upon contact with farnesol. Although the measured spectra are not shown, the ring associated bands of 2,6-DMPI are barely affected by these biogenic VOCs either. The time-variation of the NC peak position is also shown in Figure 12b: these data were also obtained at 15.6 kPa as the case of (+)-α-pinene. Once again, the NC stretching band was shifted rapidly within 5 min for both cases of farnesol and isoprene. The amount of blue-shift by farnesol was as much as 10 cm^{-1}, while the amount of red-shift by isoprene was 4 cm^{-1}. Consulting the potential-dependent SERS data in Figure 3b of section 3.1., these correspond to a potential change from -0.52 to -0.24 V by farnesol and from -0.52 to -0.62 V by isoprene. These data clearly indicate that the electronic charge transfer takes place from Au to farnesol, which thus acts as an electron acceptor, while isoprene and (+)-α-pinene act as electron donors to Au**.**

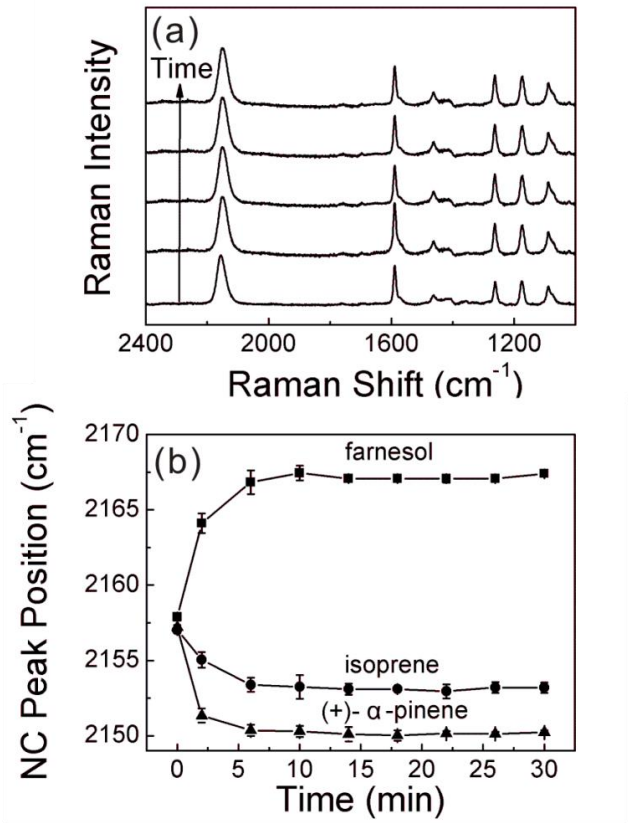

Figure 12. (a) A series of time-dependent SERS spectra of 2,6-DMPI measured under a flow of (+)-α-pinene at a partial pressure of 15.6 kPa: from bottom to top measured after 0, 2, 6, 10, and 14 min of flow, respectively. (b) Time variation of the NC stretching peak position under flows of (+)-α-pinene, isoprene, and farnesol, at a partial pressure of 15.6 kPa.

Concentration Dependency of Biogenic VOCs. Figure 13a shows the time-variation of the NC stretching peak position of 2,6-DMPI measured under the flow of (+)-α-pinene at 0.78~15.6 kPa. At lower concentrations, more time was required for the NC band to reach a plateau level. The amount of red-shift at the plateau level was dependent on the concentration of VOCs. For instance, the NC stretching band was red-shifted by up to 5 cm^{-1} at 0.78 kPa, while it was red-shifted

by up to 7 cm^{-1} at 15.6 kPa. The lower peak shift is associated with the lower surface coverage of VOCs. In this sense, it is noteworthy that even at a partial pressure of 1.56 Pa, the peak shift of 1 cm^{-1} could be reproducibly measured. Since 1.56 Pa corresponds to 68 ppm, the observation of NC peak shift by SERS is an effective tool even for the identification of biogenic VOCs.

In order to gain information on the adsorption behavior of biogenic VOCs on Au, the data have been further analyzed in Figure 13a. No further NC peak shift occured when the partial pressure of VOCs was greater than 15.6 kPa. On this ground, Figure 13b shows the relative peak shift (measured against the NC peak position at 15.6 kPa) drawn against the partial pressure of (+)-α-pinene. As assumed above, the lower peak shift can be attributed to the lower surface coverage of (+)-α-pinene. It was thus attempted to fit the data in Figure 13b to the Langmuir adsorption isotherm.[77] The isotherm equation is given by

$$\frac{\Delta\tilde{\nu}}{\Delta\tilde{\nu}_{max}} = \frac{K_{ads}\,[(+)\text{-}\alpha\text{-pinene}]}{1+K_{ads}\,[(+)\text{-}\alpha\text{-pinene}]}$$

$$\frac{[(+)\text{-}\alpha\text{-pinene}]}{\Delta\tilde{\nu}} = \frac{[(+)\text{-}\alpha\text{-pinene}]}{\Delta\tilde{\nu}_{max}} + \frac{1}{K_{ads}\Delta\tilde{\nu}_{max}}$$

where $\Delta\tilde{\nu}$ is the NC stretching peak shift at the plateau level, $\Delta\tilde{\nu}_{max}$ is its maximum value measured at 15.6 kPa, K_{ads} is the adsorption constant of (+)-α-pinene onto PEI-capped Au nanoparticles, and [(+)-α-pinene] is the concentration of (+)-α-pinene in kPa. The plot, i.e. [(+)-α-pinene]/$\Delta\tilde{\nu}$ against [(+)-α-pinene] in Figure 13c is almost linear, suggesting the appropriateness of the Langmuir adsorption model. From the ratio of the intercept and slope, K_{ads} is calculated to be 3.27 kPa^{-1}. By using this value, a theoretical Langmuir adsorption model is drawn as a solid line in Figure 13b. The theoretical values match very well with the experimental results. Although not shown here, the interaction of isoprene and farnesol with Au can also be described in terms of the Langmuir adsorption isotherm.

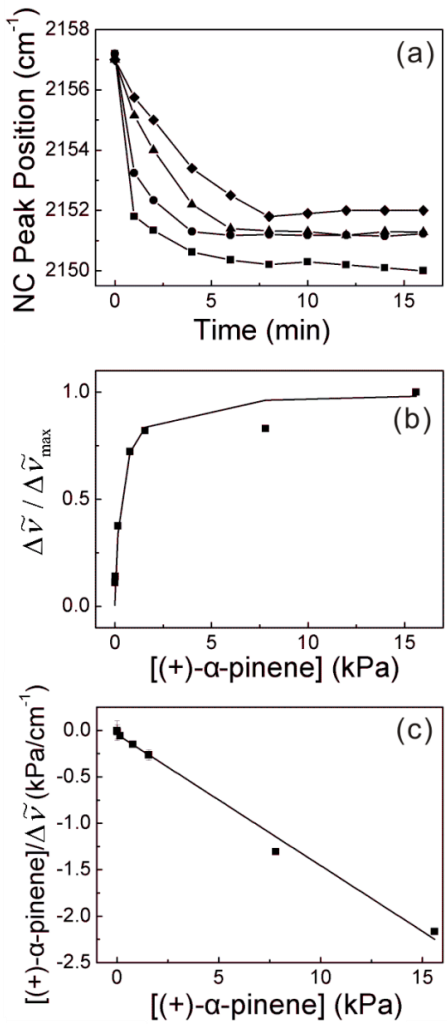

Figure 13. (a) Time variation of the NC stretching peak position of 2,6-DMPI measured under a flow of (+)-α-pinene at a partial pressure of 0.78, 1.56, 7.8, and 15.6 kPa (from top to bottom). (b) Amount of blue-shift of the NC stretching band (at plateaus) relative to that at 15.6 kPa drawn versus the concentration of (+)-α-pinene passed over 2,6-DMPI-adsorbed PEI-capped Au nanoparticle film: the solid line is a calculated Langmuir adsorption isotherm. (c) A plot of [(+)-α-pinene]/$\Delta\tilde{\nu}$ drawn versus [(+)-α-pinene] in which $\Delta\tilde{\nu}$ is the NC stretching peak shift measured at the plateau level in (b) and [(+)-α-pinene] is the partial pressure of (+)-α-pinene in units of kPa.

4. Summary and Conclusions

Organic isocyanide (such as 2,6-DMPI) adsorbed on a noble metal nanostructure can be used as a platform for VOC sensor operating via SERS. This is possible since the NC stretching band is very susceptible to the surface potential of Au onto which 2,6-DMPI is assembled. The surface potential of Au nanoparticles is even subject to change by VOCs, which can be easily monitored by the SERS of 2,6-DMPI. The variation of the NC stretching band of 2,6-DMPI on Au not only by usual VOCs such as CCl_4, methanol, ammonia, and butylamine but also by biogenic VOCs such as isoprene, farnesol, and (+)-α-pinene was clearly demonstrated. The amount of peak shift was dependent on the concentration of VOCs. The NC stretching peak shift versus the partial pressure of VOCs could be fitted to the Langmuir adsorption isotherm. The detection limit in this work is far superior to the results obtained via other techniques, especially those operating based on gold nanoparticles and aggregates.

3.3. Cyanide SERS : A Useful Platform to Detect Both VOCs and Hazardous Metal Ions

1. Introduction

The detection of VOCs by monitoring the SERS of 2,6-DMPI was possible since firstly, organoisocyanides were readily adsorbed on SERS-active metals such as Ag and Au by the formation of an M–C bond, secondly, the intrinsic stretching frequency of isocyanide group observable at 2100 ~ 2300 cm^{-1} was very different from the usual group frequencies of organic compounds, with the added benefit that the associated scattering intensity was very high, and thirdly, once bound to metals, the NC stretching frequency varied by as much as 36 cm^{-1} per 1 V variation of the metal electrode.[45,78-79] Isocyanides, R–N≡C, are geometric isomers of nitriles R–C≡N. Both consist of a carbon atom triple-bonded to a nitrogen atom, bound to an organic moiety "R" via either the nitrogen or carbon lone pair of electrons.[80] Considering the two separate lone pair electrons on the C and N atoms, the cyanide anion CN^- itself should then undoubtedly be a potent ligand especially for transition metals.[81-83] The very high affinity of the cyanide anion to metals can be attributed to its negative charge, compactness, and ability to engage in π-bonding.[84-87] Normally, metal atoms bind to the carbon atom rather than to the nitrogen, definitively owing to the formation of stronger bonds with C than with N.[88-92] Well-known transition metal complexes include hexacyanides, tetracyanides, and even dicyanides.[81,93]

In this section, the cyanide anion is demonstrated to be a far better adsorbate than are isocyanides for the detection of VOCs by means of SERS. Adsorption of the cyanide anion on a metal electrode is accompanied by the variation in the CN stretching frequency by nearly twice that of isocyanide in response to an external electric field. A greater peak shift can therefore be expected when CN (instead of 2,6-DMPI) on Au is exposed to VOCs. Another advantage

associated with the nitrogen lone-pair electrons of the cyanide anion is that, whereas metal ions present in solution cannot be identified directly by vibrational spectroscopy, metal ions (especially transition metal ions) are able to bind to the pendant nitrogen lone pair of electrons of CN on Au, resulting in the shift of the C≡N stretching band. The presence of those metal ions can then be detected by monitoring the shift of the CN stretching band using SERS. As such, this section clearly demonstrates the usefulness of the cyanide SERS not only for the detection of VOCs but also for the detection of hazardous metal ions as well.

2. Experimental

Chemicals. Potassium cyanide (KCN, 98+%), potassium chloride (KCl, 99%), sodium chloride (NaCl, 99%), sodium perchlorate ($NaClO_4$, 99%), ferrous nitrate ($Fe(NO_3)_2$, 98%), and ferric nitrate ($Fe(NO_3)_3$, 98%) were purchased from Samchun Chemical Co. Sodium nitrate ($NaNO_3$, 99%), sodium sulfate (Na_2SO_4, 99%), sodium hydrogen sulfate ($NaHSO_4$, 95%), and sodium carbonate (Na_2CO_3, 99%) were purchased from Duksan Chemical Co. Sodium hydrogen carbonate ($NaHCO_3$, 99.9%), sodium phosphate (Na_3PO_4, 96%), sodium hydrogen phosphate (Na_2HPO_4, 99%), sodium dihydrogen phosphate (NaH_2PO_4, 91%), chromium nitrate ($Cr(NO_3)_3$, 99%), manganese nitrate ($Mn(NO_3)_2$, 97%), cobalt nitrate ($Co(NO_3)_2$, 98%), nickel nitrate ($Ni(NO_3)_2$, 98.5%), farnesol (95%), (+)-α-pinene (98.5%), and Au foil (0.05 mm thick) were purchased from Sigma-Aldrich Co. Carbon tetrachloride (CCl_4, 99%) was purchased from Janssen Chimica Co. Triply distilled water of resistivity greater than 18.0MΩ·cm was used throughout, and unless specified, all the other chemicals used were of reagent grade.

Preparation of CN-adsorbed Au substrate. A SERS-active Au substrate was prepared via oxidation-reduction cycling (ORC) of an Au foil in 0.1 M KCl solution by sweeping consecutively at 1 V/s between -0.8 and +1.0 V versus a saturated Ag/AgCl electrode.[40] Cyanide was assembled onto the Au surface by soaking the Au substrate in 0.1 mM aqueous solution of KCN for 3 h. As described in section 3.2, the VOC sample was prepared by first flushing a volumetric flask (1 L) with N_2 after which it was capped with a rubber septum at atmospheric pressure. Using a syringe, a measured quantity of organics, i.e. CCl_4 or NH_3 or farnesol or (+)-α-pinene, was introduced into the volumetric flask through the rubber septum and allowed to vaporize completely. About 50 mL of the mixed gas was extracted using a syringe, and was subsequently set to flow through a glass capillary containing a CN-adsorbed Au electrode.

Instrumentation. The flow of VOCs through the glass capillary tube was controlled using a syringe pump (Model 341, SAGE Instruments, Inc.). The 632.8 nm radiation from a 17 mW He/Ne laser (Spectra Physics Model 127) was used as

the excitation source for Raman spectral measurement, and the power at the sampling position was ~0.17 mW. The spectral peak intensity was normalized with respect to that of the silicon wafer at 520 cm^{-1}. The potential of the electrochemical cell was controlled using a potentiostat (Model 660A, CH Instruments), employing CHI 660A electrochemical analyzer software (version 2.03) running on an IBM-compatible PC. All potentials are reported with respect to the saturated Ag/AgCl electrode.

3. Results & Discussion

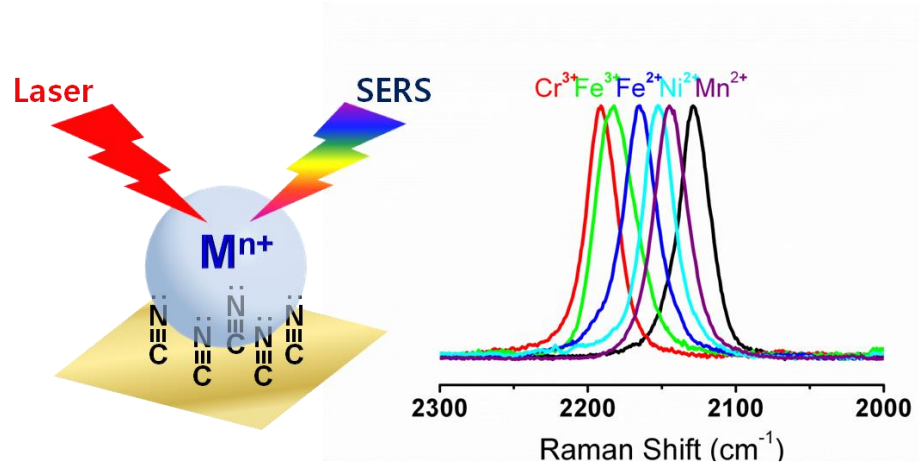

Scheme 3. Schematic representations of cyanide SERS as a platform for detection of volatile organic compounds and hazardous transition metal ions.

Normal Raman and SERS Spectrum of Cyanide on Au. Figures 14a and b show the normal Raman (NR) spectra of KCN and AgCN, respectively, in the solid state. The CN stretching band is observed at 2074 cm^{-1} in Figures 14a, but at 2164 cm^{-1} in Figures 14b. This remarkable difference (as much as 90 cm^{-1}) in the CN stretching frequency is most probably associated with the bonding mode of the cyanide ion with potassium and silver ions. The interaction of cyanide with K^+ is ionic, whereas the interaction with the silver ion is primarily covalent.[94,95] It is recognized that both the carbon and nitrogen lone-pair electrons of the cyanide anion have anti-bonding character.[81] The donation of the lone pair electrons to silver during the formation of the covalent bond necessarily results in a significant blue-shift of the CN stretching band. Owing to the ionic nature of the bond, the cyanide ion in KCN can be regarded as a free anion given that the lone pair electrons are not shared with potassium. This is evident from the NR spectrum of KCN dissolved in water (not shown) where the CN stretching band in the solution

spectrum is largely similar to that in the solid state spectrum. Figures 14c shows the SERS spectrum of cyanide adsorbed on an ORC-roughened Au substrate. The CN stretching band is observed at 2126 cm^{-1} in the SERS spectrum, indicative of a blue-shift of ca. 52 cm^{-1} upon adsorption on the Au surface.[90] The extent of the blue-shift is about one-half of that observed in the NR spectrum of AgCN. This may be reflective of the lower covalency of the Au–CN bond relative to the Ag–CN bond. However, it should be recognized that both the carbon and nitrogen lone pair electrons were donated from the anion (to the cation) in AgCN, whereas only the carbon lone pair electrons were donated in the surface adsorption of cyanide on Au. It is also noteworthy that the CN stretching band in Figures 14c is four times broader than that in Figures 14a or b, specifically, the CN stretching band was broadened from 8 to 30 cm^{-1} upon adsorption on Au. This broadening is postulated to be associated with the efficient vibrational energy relaxation channel provided by the metallic substrate, Au.

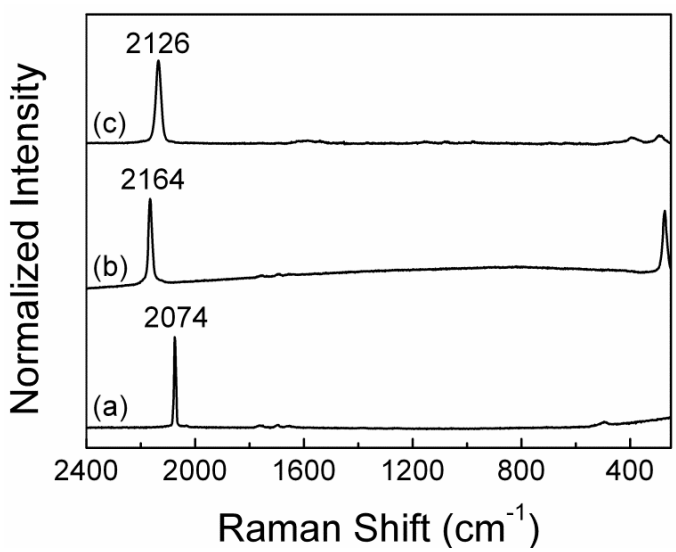

Figure 14. Normal Raman (NR) spectra of (a) KCN and (b) AgCN in solid state. (c) SERS spectrum of cyanide adsorbed on an ORC-roughened Au substrate.

Potential-Dependent SERS Spectra of Cyanide on Au. Figures 15a shows a series of SERS spectra of cyanide on Au, measured as a function of the electrode potential in 0.1 M $NaClO_4$ aqueous solution; the working electrode was the same Au electrode used to measure the SERS spectrum shown in Figures 14c. It should be mentioned that spectra similar to those in Figures 15a were obtained in 0.01 M and 0.5 M $NaClO_4$ solutions, indicating that the position of the CN stretching peak was determined solely by the applied electrode potential. Figures 15b shows the variation of the CN stretching frequency as a function of the applied potential. The plot is linear with a slope of 56 cm^{-1}/V. The positive slope can be understood by referring to the mode of bonding of cyanide to Au.[87] As the potential becomes more positive, there is an increased σ donation from the C atom to Au, resulting in an increase in the bond order of the CN bond. The converse is true when the potential is lowered. Notably, the CN stretching frequency observed at negative potentials, for instance, 2100 cm^{-1} at -0.6 V, is higher than that corresponding to free cyanide in Figures 14a. This indicates that the back-donation from Au to the CN π^* orbitals makes only a minor contribution to the spectral profile of cyanide adsorbed on Au. As mentioned in the Introduction, the NC stretching band of 2,6-DMPI varies by ~36 cm^{-1} per 1 V variation of the electrode potential, which is about two-thirds of the variation observed for cyanide adsorbed on Au. This greater potential dependence for the cyanide on Au is plausibly associated with the presence of the lone-pair of electrons not only in the carbon atom but also in the nitrogen atom in cyanide. VOCs may then be more easily detected using cyanide on Au than 2,6-DMPI on Au.

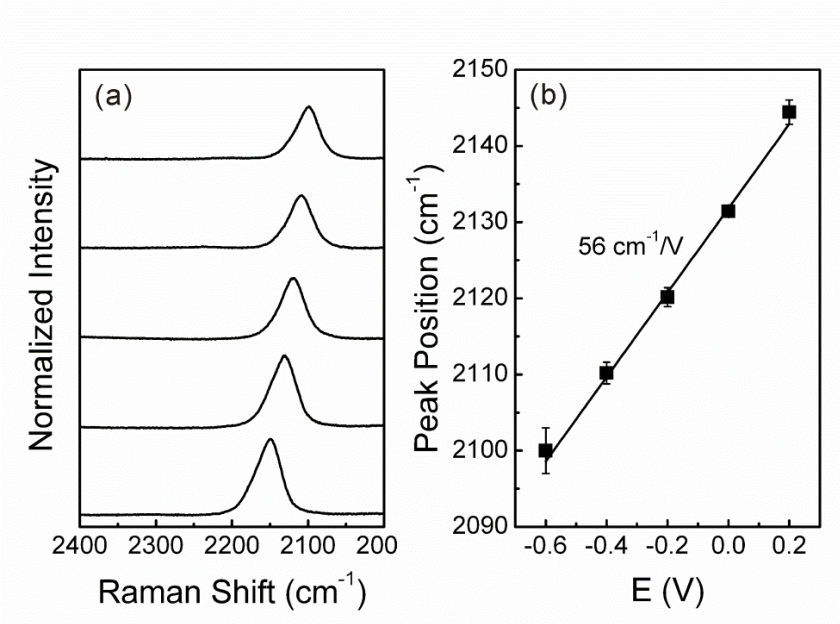

Figure 15. (a) A series of SERS spectra of cyanide on Au measured as a function of the electrode potential in 0.1 M $NaClO_4$ aqueous solution. (b) Plot of variation of the CN stretching frequency in (a) versus the applied potential.

Effect of VOCs on SERS of Cyanide on Au. The SERS spectra of cyanide on Au (placed inside a glass capillary) were acquired under a flow of various VOCs. The SERS spectral pattern of cyanide was independent of the flow rate of the VOCs in the range of 0.3 ~ 13 mL/min; the flow rate of the VOCs was thus set to 8 mL/min. The position of the CN stretching band maximum was sensitive to the type of VOCs. Figures 16a shows the CN stretching peak of cyanide recorded under a flow of CCl_4 at a partial pressure of 12 kPa. No peak due to CCl_4 was detectable, but the CN stretching band of cyanide was blue-shifted from 2126 to 2146 cm^{-1} within 30 s. Based on the potential-dependent SERS data presented in Figures 15b, this shift corresponds to a potential change from -0.1 to +0.26 V. As also shown in Figures 16a, passing 12 kPa of NH_3 over cyanide on Au effected a red-shift of the CN stretching band by as much as 21 cm^{-1}; again, no

peak due to NH_3 was detectable. This shift corresponds to a potential change from -0.1 to -0.47 V. The red-shift of the CN stretching band induced by NH_3 indicates the donation of lone-pair electrons from ammonia to Au, whereas the blue-shift induced by CCl_4 is indicative of charge transfer from gold to CCl_4. As expected from the potential-dependent data in Figures 15b, the extent of the red- or blue-shift measured using CN on Au in this work is 1.5 times greater than that measured using 2,6-DMPI on Au. This implies that the effect of VOCs on Au is the same regardless of the kind of adsorbate (CN^- or 2,6-DMPI). However, owing to the greater potential dependence, the system comprising CN on Au is more sensitive for the detection of VOCs than 2,6-DMPI on Au.

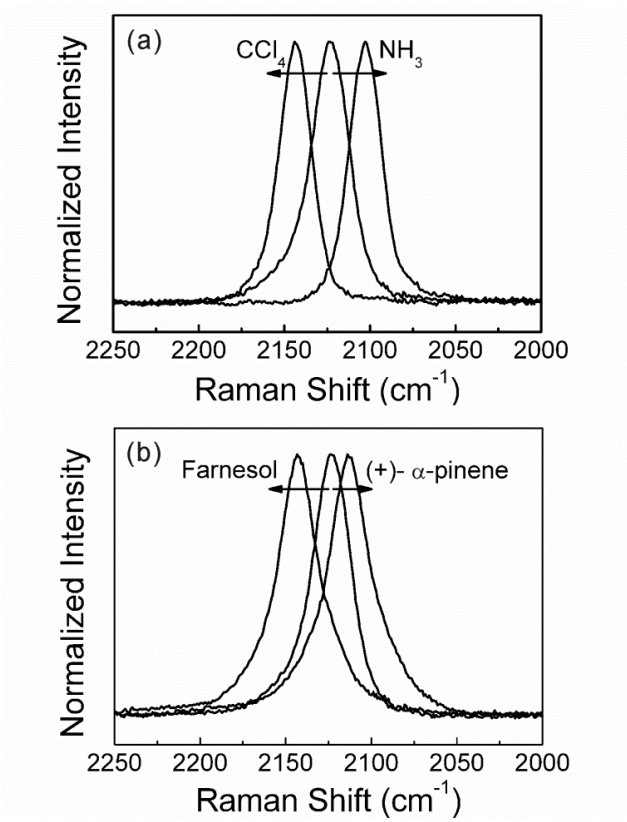

Figure 16. CN stretching peak of cyanide measured under a flow of (a) CCl_4 or NH_3 at a partial pressure of 12 kPa and (b) farnesol or (+)-α-pinene at a partial pressure of 15 kPa.

The early detection of biogenic VOCs remains a challenging task especially because of the ubiquitous and reactive nature of VOCs.[97,98] As referred in section 3.2, no device has yet been developed for their detection via vibrational spectroscopy owing to their low detectability. In this light, it was examined the extent of the effect of biogenic VOCs on the stretching band of CN on Au. Figures 16b shows the SERS spectra of cyanide measured under a flow of either farnesol or (+)-α-pinene at a partial pressure of 15 kPa. Under the flow of farnesol, the CN stretching band was blue-shifted by 20 cm^{-1} within 30 s, whereas under the flow of (+)-α-pinene, the band was red-shifted by 10 cm^{-1}. As similarly in section 3.2, these data clearly indicate that electronic charge transfer takes place from Au to farnesol, whereby farnesol acts as an electron acceptor, whereas (+)-α-pinene acts as an electron donor to Au. The present observation suggests that the cyanide on Au system can be used as a platform for a biogenic VOC sensor operating via SERS. It was thus performed more in-depth examination of the temporal variation of the CN stretching peak position of cyanide under the flow of farnesol at 0.5 ~ 10 kPa. Figures 17a demonstrates that at lower concentrations, more time was required for the CN band to reach a plateau level, we saw in section 3.2. The extent of the blue-shift at the plateau level was also dependent on the concentration of the VOCs. For instance, the CN stretching band was blue-shifted by 16 cm^{-1} at 0.5 kPa, whereas this band was blue-shifted by up to 20 cm^{-1} at 10 kPa. It is nonetheless noteworthy that even at a partial pressure of 1 Pa, a peak shift of 2 cm^{-1} can be reproducibly measured. Given that 1 Pa corresponds to 76 ppm, the observation of the shift of the CN peak due to SERS is an effective tool for the identification of biogenic VOCs (more than 2,6-DMPI on Au). A plot of [farnesol]/$\Delta\tilde{\nu}$ against [farnesol] is given in Figure 17b in which $\Delta\tilde{\nu}$ is the CN stretching peak shift measured at the plateau level in Figure 17a and [farnesol] is the partial pressure of farnesol in units of kPa. As in section 3.2, the plot is linear, suggesting that the interaction of farnesol with Au can be described by the Langmuir adsorption isotherm.[77]

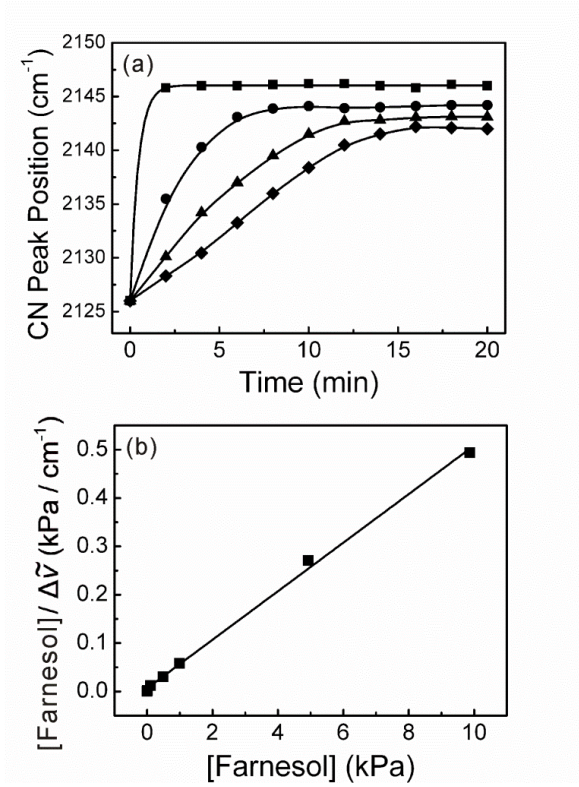

Figure 17. (a) Temporal variation of the CN stretching peak position of cyanide under a flow of farnesol at 0.5 ~ 10 kPa. (b) Plot of [farnesol]/$\Delta\tilde{\nu}$ versus [farnesol].

Effect of Metal Ions in Solution on SERS of Cyanide on Au. As a control experiment, it was first examined whether and how anions affect the CN stretching peak of cyanide adsorbed on Au. For this purpose, a 5 μL aliquot of 1 mM aqueous solution of a sodium salt such as NaCl, $NaNO_3$, Na_2SO_4, $NaHSO_4$, Na_2CO_3, $NaHCO_3$, Na_3PO_4, Na_2HPO_4, NaH_2PO_4, and $NaClO_4$ was dropped onto a film of cyanide on an ORC-roughened Au electrode, after which the Au electrode was subjected to Raman spectral measurement. The CN stretching peak was invariant with respect to the type of anion, consistently appearing at 2126 cm^{-1}. Notably, this frequency is the same as that in Figure 14c, which suggests that the anions exert a negligible effect on the surface potential of Au nanostructures. The

sodium cation is also apparently ineffective for producing a change in the CN stretching frequency, implying that its interaction with the nitrogen lone pair electrons is negligibly weak. The CN stretching band of cyanide on Au was, however, markedly affected by contact with transition metal cations. For instance, the CN stretching band underwent an immediate blue-shift by as much as 37 cm^{-1} upon contact with 1 mM aqueous solutions of $CoCl_2$, $Co(CH_3CO_2)_2$, $CoCO_3$, or $Co(NO_3)_2$. Given that the degree of the blue-shift was the same irrespective of the anion species, the peak shift is ascribed to the interaction of Co^{2+} ions with the lone pair of electrons on the nitrogen of the cyanide anions on the Au substrate. The immediate and notable blue-shift suggests that the stability constant of the cobalt(II) isocyanide complex must be very high.

The existence of concentration dependence was evaluated in the detection of the shift of the CN stretching band due to the Co^{2+} ion. For that purpose, 5 μL of 1 fM ~ 1 μM $Co(NO_3)_2$ solution was dropped onto a film of cyanide on Au. An immediate shift of the CN stretching band was apparent even upon application of 1 fM $Co(NO_3)_2$, suggesting that formation of the cobalt(II)-isocyanide complex is a kinetically favorable process. Figure 18a shows the Raman spectra of the CN stretching region measured after addition of 1, 10, or 100 fM $Co(NO_3)_2$ solution. At >100 fM $Co(NO_3)_2$, the CN stretching band occurs as a single peak with a maximum at 2163 cm^{-1}. At <100 fM $Co(NO_3)_2$, however, the CN stretching band is asymmetric. Specifically, at 10 fM $Co(NO_3)_2$, the CN stretching band is inclined toward higher frequency, with a shoulder peak at 2126 cm^{-1}. The latter peak is ascribed to CN that does not undergo coordination with the Co^{2+} ion (see the reference spectrum in Figure 18a). On the other hand, the CN band acquired with 1 fM $Co(NO_3)_2$ is asymmetrically skewed toward lower frequency. The band can be decomposed into two clear components, one centered at 2126 cm^{-1} and the other centered at 2163 cm^{-1}. The normalized intensities of the decomposed peaks are plotted in Figure 18b as a function of the concentration of $Co(NO_3)_2$ solution. The present data clearly illustrate that the cobalt ion can be reproducibly detected at a concentration as low as 1 fM by exploiting the SERS of CN-adsorbed on Au.

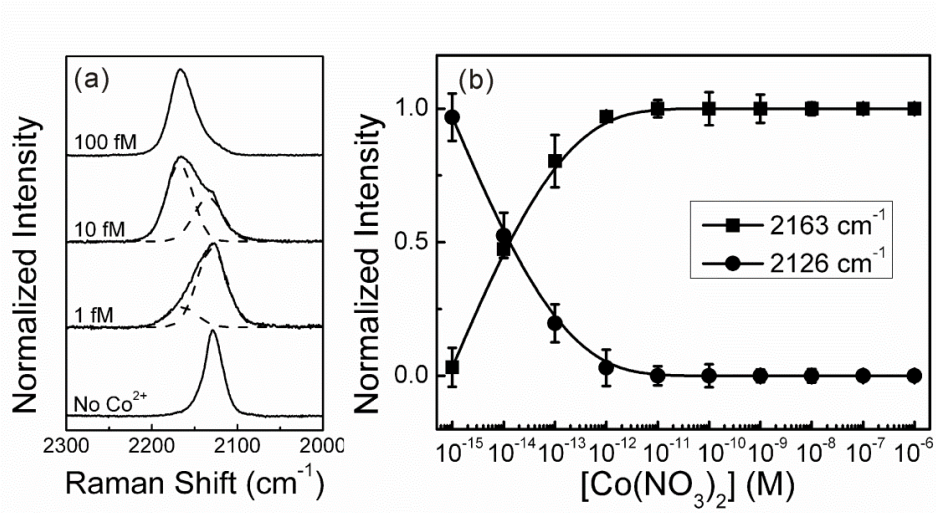

Figure 18. (a) SERS spectra of cyanide on Au measured after application of 1, 10, or 100 fM $Co(NO_3)_2$ solution. (b) Normalized intensities of Lorentzian peaks at 2126 and 2163 cm^{-1} in (a) plotted as a function of the concentration of $Co(NO_3)_2$ solution applied to cyanide on Au.

It is well known that most transition metals form cyanide complexes, having varying degrees of solubility.[99] In particular, the transition metals Cr through Ni form very stable cyanide complexes. The binding strength of metal ions to the nitrogen lone-pair electrons in CN^- is, however, comparable, or at least proportional, to binding with the carbon lone-pair electrons. In this light, the effect of Cr^{3+}, Mn^{2+}, Fe^{2+}, Fe^{3+}, Co^{2+}, and Ni^{2+} ions on the Raman spectrum of cyanide on Au was evaluated, as shown in Scheme 3. As above, a 5 μL aliquot of 1 mM aqueous solutions of nitrate salts of these ions was dropped onto cyanide on Au, and the shift of the CN stretching band was monitored. As anticipated, the peak-shift occurred immediately after application of the salt solutions. A blue-shift occurred in all cases, and the extent of the shift was highly dependent on the nature of the metal ions. Specifically, the CN stretching band was observed at 2190, 2147, 2163, 2186, 2161, and 2154 cm^{-1} for the application of Cr^{3+}, Mn^{2+}, Fe^{2+}, Fe^{3+}, Co^{2+}, and Ni^{2+} ions, respectively (See Figure 19); the corresponding magnitudes of the

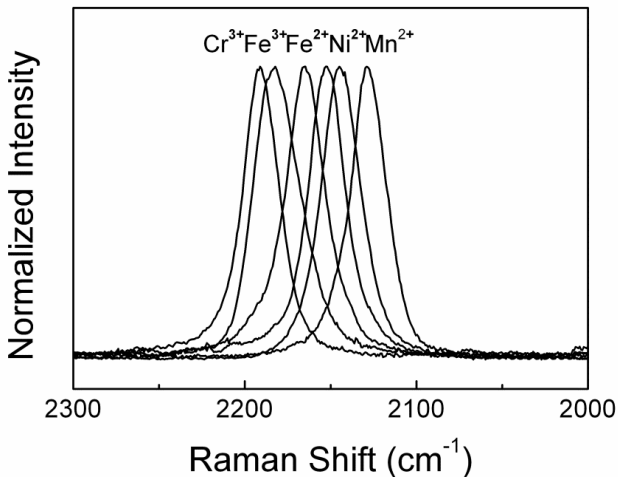

Figure 19. SERS spectra of cyanide on Au measured after application of 5 μL of 1 mM nitrate solutions of Cr^{3+}, Mn^{2+}, Fe^{2+}, Fe^{3+}, Co^{2+}, or Ni^{2+} ions.

blue-shift were thus 64 cm^{-1} for Cr^{3+}, 60 cm^{-1} for Fe^{3+}, 37 cm^{-1} for Fe^{2+}, 35 cm^{-1} for Co^{2+}, 28 cm^{-1} for Ni^{2+}, and 21 cm^{-1} for Mn^{2+}. The CN stretching peaks observed after application of the Cr^{3+} and Fe^{3+} ions were comparable to each other and more intense than those measured after the application of Mn^{2+}, Fe^{2+}, Co^{2+}, and Ni^{2+} ions. The magnitude of the blue-shift evidently increased in proportion to the ionic charge. The formation constants of the cyano complexes of transition metal ions are, in general, formidable, and in usual cases it is difficult to differentiate their values. Irrespective of this similarity, the CN stretching frequency is, nevertheless, clearly dependent on the nature of the transition metal ions. For instance, the formation constants (pK_a's) of $Fe(CN)_6^{4-}$, $Ni(CN)_4^{2-}$, and $Zn(CN)_4^{2-}$ are known to be -35.4, -30.0, and -19.6, respectively.[25] The extent of the CN peak shift measured herein was 37 cm^{-1} for Fe^{2+}, 28 cm^{-1} for Ni^{2+}, and 16 cm^{-1} for Zn^{2+}, which correlated well with the formation constants even though the latter values were very large. This is suggestive of the possibility that cyanide SERS may be applicable in the detection of hazardous transition metal ions even for concentrations as low as the femto molar level.

4. Summary and Conclusions

Cyanide adsorbed on nanostructured Au is demonstrated to be a very useful system for the detection of not only VOCs but also transition metal ions by means of SERS. This is associated with the susceptibility of the CN stretching frequency of cyanide on Au to the variation of the surface potential of the Au nanostructures that occurs in response to the adsorption of VOCs onto these surfaces. It is also associated with the susceptibility to the binding of transition metal cations onto the pendant nitrogen atom, which reduces the anti-bonding character of the nitrogen lone pair of electrons. The CN stretching band underwent a blue-shift by up to 20 cm^{-1} in response to a typical biogenic VOC farnesol, whereas the band was red-shifted by 10 cm^{-1} in response to the typical biogenic VOC (+)-α-pinene. This method must be highly sensitive (more than the system of 2,6-DMPI on Au) given that the peak shift of 2 cm^{-1} could be reproducibly measured even at a partial pressure of 1 Pa, corresponding to 76 ppm of farnesol. The CN stretching band was also demonstrated to undergo a blue-shift by up to 60 ~ 64 cm^{-1} in the presence of trivalent cations such as Fe^{3+} and Cr^{3+}, whereas the band was blue-shifted by 26 ~ 35 cm^{-1} in the presence of divalent metal ions such as Mn^{2+} and Fe^{2+}. The present SERS method is regarded as very promising because transition metal ions were detectable at concentration levels as low as 1 fM.

3.4. References

1. Andres, R. P.; Bielefeld, J. D.; Henderson, J. I.; Janes, D. B.; Kolagunta, V. R.; Kubiak, C. P.; Mahoney, W. J.; Osifchin, R. G. *Science* **1996**, *273*, 1690.
2. Schimd, G. *Chem. Rev.* **1992**, *92*, 1709.
3. McFarland, A. D.; Van Duyne, R. P. *Nano Letters* **2003**, *3*, 1057.
4. Daniel, M. –C.; Astruc, D. *Chem. Rev.* **2004**, *104*, 293.
5. Roduner, E. *Chem. Soc. Rev.* **2006**, *35*, 583.
6. Ulman, A. *Chem. Rev.* **1996**, *96*, 1533.
7. Hostetler, M. J.; Murray, R. W. *Curr. Opin. Colloid Interface Sci.* **1997**, *2*, 42.
8. Delamarche, E.; Sundarababu, G.; Biebuyck, H.; Michel, B.; Gerber, Ch.; Sigrist, H.; Wolf, H.; Ringsdorf, H.; Xanthopoulos, N.; Mathieu, H. J. *Langmuir* **1996**, *12*, 1997.
9. Culha, M.; Stokes, D.; Allain, L. R.; Vo-Dinh, T. *Anal. Chem.* **2003**, *75*, 6196.
10. Donath, E.; Sukhorukov, G. B.; Caruso, F.; Davis, S. A.; Möhwald, H. *Angew. Chem. Int. Ed.* **1998**, *37*, 2201.
11. Caruso, F.; Caruso, R. A.; Möhwald, H. *Science* **1998**, *282*, 1111.
12. Gittins, D. I.; Caruso, F. *J. Phys. Chem. B* **2001,** *105*, 6846.
13. Decher, G.; Schlenoff, J. B. *Multilayer Thin Films: Sequential Assembly of Nanocomposite Materials*; Wiley-VCH: Weinheim, 2002.
14. Decher, G.; Hong, J. D. *Makromol. Chem., Macromol. Symp.* **1991**, *46*, 321.
15. Decher, G.; Hong, J. D. *Ber. Bunsen-Ges. Phys. Chem.* **1991**, *95*, 1430.
16. Decher, G.; Hong, J. D.; Schmitt, J. *Thin Solid Films* **1992**, *210*, 831.
17. Decher, G.; Schmitt, J. *Prog. Colloid Polym. Sci.* **1992**, *89*, 160.
18. Lvov, Y.; Decher, G.; Möhwald, H. *Langmuir* **1993**, *9*, 481.
19. Decher, G.; Lvov, Y.; Schmitt, J. *Thin Solid Films* **1994**, *244*, 772.
20. Decher, G. *Science* **1997**, *277*, 1232.
21. Netz, R. R.; Joanny, J.-F. *Macromolecules* **1999**, *32*, 9026.
22. Kunze, K.-K.; Netz, R. R. *Phys. Rev. Lett.* **2000**, *85*, 4389.
23. Gole, A.; Murphy, C. J. *Chem. Mater.* **2005**, *17*, 1325.
24. Mulvaney, P. *Langmuir* **1996**, *12*, 788.

25. Alvarez, M. M.; Khoury, J. T.; Schaaf, T. G.; Shafigullin, M. N.; Vezmar, I.; Whetten, R. L. *J. Phys. Chem. B* **1997**, *101*, 3706.
26. Underwood, S.; Mulvaney, P. *Langmuir* **1994**, *10*, 3427.
27. Shin, D.; Kim, K.; Shin, K. S. *ChemPhysChem* **2010**, *11*, 83.
28. Tang, M. X.; Szoka, F. C. *Gene Ther.* **1997**, *4*, 823.
29. Remy-Kristensen, A.; Clamme, J.-P.; Vuilleumier, C.; Kuhry, J.-G.; Mely, Y. *Biochim. Biophys. Acta* **2001**, *1514*, 21.
30. Kichler, A.; Leborgne, C.; Coeytaux, E.; Danos, O. *J. Gene Med*. **2001**, *3*, 135.
31. Wang, D.-A.; Narang, A. S.; Kotb, M.; Gaber, A. O.; Miller, D. D.; Kim, S. W.; Mahato, R. I. *Biomacromolecules* **2002**, *3*, 1197.
32. Koper, G. J. M. *Macromolecules* **2003**, *36*, 2500.
33. Hall, H. K. Jr. *J. Am. Chem. Soc*. **1957**, *79*, 5441.
34. Behr, J.-P. *Chimia* **1997**, *51*, 34.
35. Klitzing, R. *Phys. Chem. Chem. Phys.* **2006**, *8*, 5012.
36. Yoo, D.; Shiratori, S. S.; Rubner, M. F. *Macromolecules* **1998**, *31*, 4309.
37. Dubas, S. T.; Schlenoff, J. B. *Macromolecules* **2001**, *34*, 3736.
38. Yan, M.; Zhan, S.; Zhou, X.; Liu, Y.; Feng, L.; Lin, Y.; Zhang, Z.; Hu, J. *Langmuir* **2008**, *24*, 8707.
39. Kim, K.; Lee, H. B.; Lee, J. W.; Shin, K. S. *Langmuir* **2008**, *24*, 7178.
40. Liu, Y. C. *Langmuir* **2002**, *18*, 174.
41. Ontko, A. C.; Angelici, R. J. *Langmuir* **1998**, *14*, 1684.
42. Kim, H. S.; Lee, S. J.; Kim, N. H.; Yoon, J. K.; Park, H. K.; Kim, K. *Langmuir* **2003**, *19*, 6701.
43. Kim, K.; Kim, K. L.; Choi, J.-Y.; Lee, H. B.; Shin, K. S. *J. Phys. Chem. C* **2010**, *114*, 3448.
44. Frisch, M. J.; Trucks, G. W.; Schlegel, H. B.; Scuseria, G. E.; Robb, M. A.; Cheeseman, J. R.; Montgomery, J. A., Jr.; Vreven, T.; Kudin, K. N.; Burant, J. C.; Millam, J. M.; Iyengar, S. S.; Tomasi, J.; Barone, V.; Mennucci, B.; Cossi, M.; Scalmani, G.; Rega, N.; Petersson, G. A.; Nakatsuji, H.; Hada, M.; Ehara, M.; Toyota, K.; Fukuda, R.; Hasegawa, J.; Ishida, M.; Nakajima, T.; Honda, Y.;

Kitao, O.; Nakai, H.; Klene, M.; Li, X.; Knox, J. E.; Hratchian, H. P.; Cross, J. B.; Bakken, V.; Adamo, C.; Jaramillo, J.; Gomperts, R.; Stratmann, R. E.; Yazyev, O.; Austin, A. J.; Cammi, R.; Pomelli, C.; Ochterski, J. W.; Ayala, P. Y.; Morokuma, K.; Voth, G. A.; Salvador, P.; Dannenberg, J. J.; Zakrzewski, V. G.; Dapprich, S.; Daniels, A. D.; Strain, M. C.; Farkas, O.; Malick, D. K.; Rabuck, A. D.; Raghavachari, K.; Foresman, J. B.; Ortiz, J. V.; Cui, Q.; Baboul, A. G.; Clifford, S.; Cioslowski, J.; Stefanov, B. B.; Liu, G.; Liashenko, A.; Piskorz, P.; Komaromi, I.; Martin, R. L.; Fox, D. J.; Keith, T.; Al-Laham, M. A.; Peng, C. Y.; Nanayakkara, A.; Challacombe, M.; Gill, P. M. W.; Johnson, B.; Chen, W.; Wong, M. W.; Gonzalez, C.; Pople, J. A. Gaussian 03W, revision C.01; Gaussian, Inc.: Wallingford CT, 2004.

45. Kim, N. H.; Kim, K. *J. Phys. Chem. B* **2006**, *110*, 1837.
46. Suh, J.; Paik, H.-J.; Hwang, B. K. *Bioorg. Chem.* **1994**, *22*, 318.
47. Smits, R. G.; Koper, G. J. M.; Mandel, M. *J. Phys. Chem.* **1993**, *97*, 5745.
48. Chatterji, P. R. *J. Appl. Polm. Sci.* **1990**, *40*, 404.
49. Liu, J.; Li, N.; Jiang, G.; Liu, J.; Jönssonc, J. Å.; Wen, M. *J. Chromatogr. A* **2005**, *1006*, 27.
50. Holcomb, L. C.; Seabrook, B. S. *Indoor Environ.* **1995**, *4*, 7.
51. Mendell, M. J. *Indoor Air* **2007**, *17*, 259.
52. D'Amato, G.; Cecchi, L. *Clin. Exp. Allergy* **2008**, *38*, 1264.
53. Phillips, M.; Gleeson, K.; Hughes, J. M. B.; Greenberg, J.; Cataneo, R. N.; Baker, L.; Mcvay, W. P. *Lancet* **1999**, *353*, 1530.
54. Isidorov, V. A.; Zenkevich, I. G.; Ioffe, B. V. *Atmos. Envion.* **1967**, *19*, 1.
55. Kesselmeier, J.; Staudt, M. *J. Atmos. Chem*. **1999**, *33*, 23.
56. Goldstein, A. H.; Galbally, I. E. *Environ. Sci. Technol.* **2007**, *41*, 1514.
57. Chameides, W. L.; Fehsenfeld, F.; Rodgers, M. O.; Cardelino, C.; Martinez, J.; Parrish, D.; Lonneman, W.; Lawson, D. R.; Rasmussen, R. A.; Zimmerman, P.; Greenberg, J.; Middleton, P.; Wang,T. *J. Geophys. Res*. **1992**, *97*, 6037.
58. Trainer, M.; Hsie, E. Y.; McKeen, S. A.; Tallamraju, R.; Parrish, D. D.; Fehsenfeld, F. C.; Liu, S. C. *J. Geophys. Res.***1987**, *92*, 11897.

59. Chameides, W. L.; Lindsay, R. W.; Richardson, J.; Kiang, C. S. *Science* **1988**, *241*, 1473.

60. Biesenthal, T.; Wu, Q.; Shepson, P. B.; Wiebe, H. A.; Anlauf, K. G.; Mackay, G. I. *Atmos. Environ.* **1997**, *31*, 2049.

61. Albert, K. J.; Lewis, N. S.; Schauer, C. L.; Sotzing, G. A.; Stitzel, T. P.; Walt, D. R. *Chem. Rev.* **2000**, *100*, 2595.

62. Dutta, R.; Hines, E. L.; Gardner, J. W.; Kashwan, K. R.; Bhuyan, M. *Sens. Actuat. B* **2003**, *94*, 228.

63. Walter, E. C.; Favier, F. R.; Penner, M. *Anal. Chem.* **2002**, *74*, 1546.

64. Qi, P.; Vermesh, O.; Grecu, M.; Javey, A.; Wang, Q.; Dai, H.; Peng, S.; Cho, K. J. *Nano Lett.* **2003**, *3*, 347.

65. Krasteva, N.; Besnard, I.; Guse, B.; Bauer, R. E.; Mullen, K.; Yasuda, A.; Vossmeyer, T. *Nano Lett*. **2002**, *2*, 551.

66. Ahn, H.; Chandekar, A.; Kang, B.; Sung, C.; Whitten, J. E. *Chem. Mater.* **2004**, *16*, 3274.

67. Zhang, H.-L.; Evans, S. D.; Henderson, J. R.; Miles, R. E.; Shen, T.-H. *Nanotechnology* **2002**, *13*, 439.

68. Chang, R. K.; Furtak, T. E. *Surface Enhanced Raman Scattering*, Plenum Press, New York, 1982.

69. Moskovits, M. *Rev. Mod. Phys*. **1985**, *57*, 783.

70. Nie, S.; Emory, S. R. *Science* **1997**, *275*, 1102.

71. Schatz, G. C.; Van Duyne, R. P. *Electromagnetic Mechanism of Surface Enhanced Spectroscopy*, Wiley, New York, 2002, Vol. 1.

72. Aroca, R. *Surface-Enhanced Vibrational Spectroscopy*, Wiley, New York, 2006.

73. Oo, M. K. K.; Chang, C.-F.; Sun, Y.; Fan, X. *Analyst* **2011**, *136*, 2811.

74. Mosier-Boss, P. A.; Lieberman, S. H. *Anal. Chim. Acta* **2003**, *488*, 15.

75. Ha, T. H.; Kim, C. H.; Park, J. S.; Kim, K. *Langmuir* **2000**, *16*, 871.

76. Sauerbrey, G. Z. *Phys.* **1959**, *155*, 206.

77. Kim, S. H.; Ahn, S. J.; Kim, K. *J. Phys. Chem.* **1996**, *100*, 7174.

78. Kim, K.; Lee, J. W.; Lee, H. B.; Shin, K. S. *Langmuir* **2009**, *25*, 9697.

79. Kim, K.; Lee, J. W.; Shin, D.; Shin, K. S. *J. Phys. Chem. C* **2010**, *114*, 9917.
80. Gridnev, I. D.; Gridneva, N. A. *Russ. Chem. Rev.* **1995**, *64*, 1021.
81. Griffith, W. P. *Q. Rev. Chem. Soc.* **1962**, *16*, 188.
82. Perumareddi, J. R.; Liehr, A. D.; Adamson, A. W. *J. Am. Chem. Soc.* **1963**, *85*, 249.
83. Nakagawa, I.; Shimanouchi, T. *Spectrochim Acta* **1962**, *18*, 101.
84. Flament, J. P.; Tadjeddine, M. *J. Mol. Struc.-Theochem* **1995**, *330*, 155.
85. Llewellyn, J. H. *Inorg. Chem.* **1963**, *2*, 777.
86. Ren, B.; Wu, D.-Y.; Mao, B.-W.; Tian, Z.-Q. *J. Phys. Chem. B* **2003**, *107*, 2752.
87. Kellogg. D. S.; Pemberton, J. E. *J. Phys. Chem.* **1987**, *91*, 1120.
88. Anderson, A. B.; Kötz, R.; Yeager, E. *Chem. Phys. Lett.* **1981**, *82*, 130.
89. Ren, B.; Li, X.-Q.; Wu, D.-Y.; Yao, J.-L.; Xie, Y.; Tian, Z.-Q. *Chem. Phys. Lett.* **2000**, *322*, 561.
90. Jacobs, B.; Jagodzinski, P. W.; Jones, T. E.; Eberhart, M. E. *J. Phys. Chem. C* **2011**, *115*, 24115.
91. Beltaramo, G. L.; Shubina, T. E.; Mitchell, S. J.; Koper, M. T. M. *J. Electroanal. Chem.* **2004**, *563*, 111.
92. Murray, C. A.; Bodoff, S. *J. Chem. Phys.* **1986**, *85*, 573.
93. Perumareddi, J. R.; Liehr, A. D.; Adamson, A. W. *J. Am. Chem. Soc.* **1963**, *85*, 249.
94. Wormer, P. E. S.; Tennyson, J. *J. Chem. Phys.* **1981**, *75*, 1245.
95. Dietz, O.; Rayón, V. M.; Frenking, G. *Inorg. Chem.* **2003**, *42*, 4977.
96. Baltruschat, H.; Heitbaum, J. *J. Electroanal. Chem.* **1983**, *157*, 319.
97. Chameides, W. L.; Fehsenfeld, F.; Rodgers, M. O.; Cardelino, C.; Martinez, J.; Parrish, D.; Lonneman, W.; Lawson, D. R.; Rasmussen, R. A.; Zimmerman, P.; Greenberg, J.; Middleton, P.; Wang, T. *J. Geophys. Res.* **1992**, *97*, 6037.
98. Trainer, M.; Hsie, E. Y.; McKeen, S. A.; Tallamraju, R.; Parrish, D. D.; Fehsenfeld, F. C.; Liu, S. C. *J. Geophys. Res.* **1987**, *92*, 11894.
99. Beck, M. T. *Pure Appl. Chem.* **1987**, *59*, 1703.

Appendix

List of Publications

List of Patent

List of Presentations

List of Publications

1. Kwan Kim*, **Ji Won Lee**, Hyang Bong Lee, and Kuan Soo Shin, "A Novel Fabrication of Au-Nanoparticle Films on Planar and Curved Surfaces of Glasses and Fiber Materials", *Langmuir*, **2009**, *25*, 9697.
2. Kwan Kim*, Hyang Bong Lee, **Ji Won Lee**, and Kuan Soo Shin, "Poly(ethylenimine)-Stabilized Silver Nanoparticles Assembled into 2-dimensional Arrays at Water-Toluene Interface", *J. Colloid Interf. Sci.*, **2010**, *345*, 103.
3. **Ji Won Lee**, Hyang Bong Lee, Kwan Kim*, and Kuan Soo Shin, "A Novel Fabrication of Silver-Coated Glass Capillaries for Ready SERS-Based Detection of Dissolved Chemical Species", *Anal. Bioanal. Chem.*, **2010**, *397*, 557.
4. **Ji Won Lee**, Kwan Kim*, and Kuan Soo Shin, "A Novel Fabrication of Au-Coated Glass Capillaries for Chemical Analysis by Surface-Enhanced Raman Scattering", *Vib. Spectrosc.*, **2010**, *53*, 121.
5. Kwan Kim*, **Ji Won Lee**, Dongha Shin, Kyung Lock Kim and Kuan Soo Shin, "Surface Potential of Au Nanoparticles Affected by Layer-by-Layer Deposition of Polyelectrolytes: A Surface-Enhanced Raman Scattering Study", *J. Phys. Chem. C*, **2010**, *114*, 9917.
6. Kwan Kim*, Kyung Lock Kim, Dongha Shin, **Ji Won Lee** and Kuan Soo Shin, "Effect of Polar Organic Vapors on Surface Potential of Au Nanoparticle Aggregates Probed By Surface-Enhanced Raman Scattering of 2,6-Dimethylphenylisocyanide", *Chem. Comm.*, **2010**, *46*, 3753.
7. Kwan Kim*, **Ji Won Lee**, Jeong-Yong Choi and Kuan Soo Shin, "The pH Effect on Surface Potential of Polyelectrolytes-Capped Gold Nanoparticles Probed by Surface-Enhanced Raman Scattering", *Langmuir*, **2010**, *26*, 19163.
8. Kwan Kim*, Hyang Bong Lee, Dongha Shin, Hyunwoo Ryoo, **Ji Won**

Lee and Kuan Soo Shin, "Surface-Enhanced Raman Scattering of 4-Aminobenzenethiol on Silver: Confirmation of The Origin of b_2-Type Bands", *J. Raman Spectrosc.*, **2011**, *42*, 2112.

9. Kwan Kim*, **Ji Won Lee**, Dongha Shin, Jeong-Yong Choi and Kuan Soo Shin "Organic Isocyanide-Adsorbed Gold Nanostructure: A SERS Sensory Device for Indirect Peak-Shift Detection of Volatile Organic Compounds ", *Analyst*, **2012**, *137*, 1930.
10. Kwan Kim*, **Ji Won Lee** and Kuan Soo Shin "Poly(ethylenimine)-Capped Ag Nanoparticle Film as A Platform for Detecting Charged Dye Molecules by Surface-Enhanced Raman Scattering and Surface-Enhanced Fluorescence", *ACS Appl. Mater. Inter.* **2012**, *4*, 5498.
11. Kwan Kim*, **Ji Won Lee** and Kuan Soo Shin "Detection of a few of Biogenic Volatile Organic Compounds by means of Raman Scattering of Isocyanide-Adsorbed Gold Nanostructures", *Spec. Chim. Acta Part A*, **2013**, *100*, 15.
12. . Kwan Kim*, **Ji Won Lee** and Kuan Soo Shin "Cyanide SERS as a Platform for Detection of Volatile Organic Compounds and Hazardous Transition Metal Ions", *Analyst*, **2013**, *138*, 2988.

List of Patent

1. Kwan Kim*, **Ji Won Lee**, Hyang Bong Lee, “Preparation method of gold or silver nanoparticle film having Surface-enhanced-Raman-Scattering activity,” Korea Patent, Seoul National University, #10-1029138, Apr. 2011.

List of Presentations

·International conferences

1. **Ji Won Lee** and Kwan Kim* "Surface Potential Variation of Gold Nanoparticles by Layer-by-Layer Deposition of Polyelectrolytes Probed by Raman Spectroscopy" *2010 International Chemical Congress of Pacific Basin Societies* Hawaii, USA, Dec. 2010.
2. **Ji Won Lee** and Kwan Kim* "Organic Isocyanide-Adsorbed Gold Nanostructure: A Sensory Device for Detection of Volatile Organic Compounds by Raman Scattering Spectroscopy" *Colloquium Spectroscopicum Internationale* XXXVII Rio de Janeiro, Brazil, Aug. 2011.
3. **Ji Won Lee** and Kwan Kim* "Organic Isocyanide-Adsorbed Gold Nanostructure: A Sensory Device for Detection of Volatile Organic Compounds by Raman Scattering Spectroscopy" *The Third Asian Spectroscopy Conference* Xiamen, China, Nov. 2011.
4. **Ji Won Lee** and Kwan Kim* "Organic Isocyanide-Adsorbed Gold Nanostructure: A Sensory Device for Detection of Volatile Organic Compounds by Raman Scattering Spectroscopy" *2nd International Advances in Applied Physics &Materials Science Congress* Antalya, Turkey, Apr. 2012.
5. **Ji Won Lee** and Kwan Kim* "Organic Isocyanide-Adsorbed Gold Nanostructure: Surface Potential Variation of Nanoparticles probed by Surface-enhanced Raman Scattering" 23rd *International Conference on Raman Spectroscopy* Bangalore, India, Aug. 2012.
6. Kwan Kim* and **Ji Won Lee** "Organic Isocyanide-Adsorbed Gold Nanostructure: A SERS Sensory Device to Detect Volatile Organics" *13th Topical Meeting of the International Society of Electrochemistry* Pretoria, South Africa, Apr. 2013.

7. **Ji Won Lee** and Kwan Kim* "Isocyanide-Adsorbed Au Nanoelectrode to Detect Biogenic Volatile Organics by Raman Scattering Spectroscopy" *13th Topical Meeting of the International Society of Electrochemistry* Pretoria, South Africa, Apr. 2013. **(Oral Presentation)**

·*Domestic conferences*

1. **Ji Won Lee**, Kuan Soo Shin, and Kwan Kim* "Surface Potential Variation of Au Nanoparticles by Layer-by-Layer Deposition of Polyelectrolytes: A Surface-Enhanced Raman Spectroscopy" *The 105th Spring Meeting of the Korean Chemical Society*, Incheon, Korea, Apr. 2010.
2. **Ji Won Lee** and Kwan Kim* "Organic Isocyanide-Adsorbed Gold Nanostructure to Detect Volatile Organic Compounds by Raman Scattering Spectroscopy" *2013 Asian Core Winter School* Busan, Korea, Jan. 2013.

Abstract (Korean)

금속 나노입자의 2 차원 배열은 나노 디바이스의 응용 가능성 때문에 많은 주목을 받아왔다. 그래서 최근 몇 년간 균일한 나노입자의 제조뿐만 아니라 2 차원 자기 조립에 관한 많은 연구가 진행되었다. 본 연구에서는 폴리에틸렌이민을 환원제와 안정제로 이용하여 금, 은 전구체를 환원시켜 나노입자를 제조한 후 이를 수용액상에 분산시킨 후 톨루엔과 벤젠치올을 가하여 물-톨루엔 계면에서 벤젠치올과 결합한 나노입자의 2 차원 구조체를 만들었다. 또한 이를 편평한 유리뿐만 아니라 유리 모세관의 내벽, 면섬유, 실리카 비드 등 기질의 종류나 형태에 특별히 제한받지 않고 마찬가지 방법으로 코팅할 수 있었다. 만들어진 금, 은 나노입자 필름은 장시간 안정적이며 균일한 표면 증강 라만 세기를 가짐을 확인하였다. 또한 흡착된 벤젠치올은 표면 증강 라만 산란 활성세기를 그대로 유지하며 흡, 탈착이 가능하기 때문에 유기분자의 흡, 탈착 동력학적 연구를 할 수 있었다. 특히 폴리에틸렌이민은 양전하를 띄는 고분자이므로 이로 만들어진 은 나노입자 필름은 전하를 띄고 있는 염료분자를 표면 증강 라만 산란과 표면 증강 형광을 통해 효과적으로 검출할 수 있음을 입증하였다.

나노 구조체에 흡착한 유기 아이소니트릴 분자의 NC 신축 진동 파동수는 나노 구조체의 표면 전하 (표면 전위)에 민감하다. 이 사실을 바탕으로 외부 환경 변화에 대한 나노 입자의 표면 전위 변화를 아이소니트릴 분자의 표면 증강 라만 산란 스펙트럼을 통해 알아 보았다. 첫번째로 폴리에틸렌이민으로 환원된 금 나노 입자에 2,6-디메틸페닐아이소시아나이드를 흡착시켜 외부의 pH 를 변화 시키면, 나노입자를 둘러싸고 있는 폴리에틸렌이민의 1 차 아민의 pK_a 값과 비슷한 pH 8.5 에서 NC 신축 진동 파동수가 급격하게 변하는 것을 확인하였다. 더 나아가 금 나노 입자의 표면 전위는 음이온/양이온

고분자 전해질의 교환적 적층에 의해서도 바뀌며 그 정도가 층이 높아질수록 점차 감소함을 확인하였다. 둘째, 아이소니트릴분자가 흡착된 나노 구조체가 휘발성 유기 기체 분자를 검출할 수 있는 센서로 사용될 수 있음을 입증하였다. 이는 나노 입자가 유기 기체 분자와 상호 작용하면서 전자를 주거나 받아 나노 입자의 표면 전하가 바뀌게 되기 때문이다. 마지막으로 나이트릴이 흡착된 나노 구조체가 아이소나이트릴이 흡착된 나노 구조체보다 더 효과적으로 휘발성 유기 기체 분자를 검출할 수 있음을 입증하였다. 또한 전이금속이 나이트릴 이온의 질소 비공유 전자쌍과 결합하여 CN 신축 진동수를 변화시켜 낮은 농도까지 효과적으로 검출 가능함을 확인하였다.

주요어: 표면 증강 라만 산란, 나노 구조, 금 나노 입자, 은 나노 입자, 금 나노 입자, 폴리에틸렌이민, 아이소나이트릴, 표면 전위, NC 신축 진동 파동수, 표면 증강 형광

학번: 2009-30851